SANDIA REPORT

SAND2003-2099
Unlimited Release
Printed July 2003

SPUF—A SIMPLE POLYURETHANE FOAM MASS LOSS AND RESPONSE MODEL

Michael L. Hobbs and Gordon H. Lemmon

Prepared by
Sandia National Laboratories
Albuquerque, New Mexico 87185 and Livermore, California 94550

Sandia is a multiprogram laboratory operated by Sandia Corporation,
a Lockheed Martin Company, for the United States Department of Energy's
National Nuclear Security Administration under Contract DE-AC04-94AL85000.

Sandia National Laboratories

Issued by Sandia National Laboratories, operated for the United States Department of Energy by Sandia Corporation.

Available to DOE and DOE contractors from
U.S. Department of Energy
Office of Scientific and Technical Information
P.O. Box 62
Oak Ridge, TN 37831

Telephone: (865)576-8401
Facsimile: (865)576-5728
E-Mail: reports@adonis.osti.gov
Online ordering: http://www.doe.gov/bridge

Available to the public from
U.S. Department of Commerce
National Technical Information Service
5285 Port Royal Rd
Springfield, VA 22161

Telephone: (800)553-6847
Facsimile: (703)605-6900
E-Mail: orders@ntis.fedworld.gov
Online order: http://www.ntis.gov/help/ordermethods.asp?loc=7-4-0#online

SAND2003-2099
Unlimited Release
Printed July 2003

SPUF – A SIMPLE POLYURETHANE FOAM MASS LOSS AND RESPONSE MODEL

Michael L. Hobbs and Gordon H. Lemmon
Engineering Sciences Center
Sandia National Laboratories
P.O. Box 5800
Albuquerque, New Mexico 87185

Abstract

A Simple PolyUrethane Foam (SPUF) mass loss and response model has been developed to predict the behavior of unconfined, rigid, closed-cell, polyurethane foam-filled systems exposed to fire-like heat fluxes. The model, developed for the B61 and W80-0/1 fireset foam, is based on a simple two-step mass loss mechanism using distributed reaction rates. The initial reaction step assumes that the foam degrades into a primary gas and a reactive solid. The reactive solid subsequently degrades into a secondary gas. The SPUF decomposition model was implemented into the finite element (FE) heat conduction codes COYOTE [1] and CALORE [2], which support chemical kinetics and dynamic enclosure radiation using "element death." A discretization bias correction model was parameterized using elements with characteristic lengths ranging from 1-mm to 1-cm. Bias corrected solutions using the SPUF response model with large elements gave essentially the same results as grid independent solutions using 100-μm elements. The SPUF discretization bias correction model can be used with 2D regular quadrilateral elements, 2D paved quadrilateral elements, 2D triangular elements, 3D regular hexahedral elements, 3D paved hexahedral elements, and 3D tetrahedron elements. Various effects to efficiently recalculate viewfactors were studied — the element aspect ratio, the element death criterion, and a "zombie" criterion. Most of the solutions using irregular, large elements were in agreement with the 100-μm grid-independent solutions. The discretization bias correction model did not perform as well when the element aspect ratio exceeded 5:1 and the heated surface was on the shorter side of the element. For validation, SPUF predictions using various sizes and types of elements were compared to component-scale experiments of foam cylinders that were heated with lamps. The SPUF predictions of the decomposition front locations were compared to the front locations determined from real-time X-rays. SPUF predictions of the 19 radiant heat experiments were also compared to a more complex chemistry model (CPUF) predictions made with 1-mm elements. The SPUF predictions of the front locations were closer to the measured front locations than the CPUF predictions, reflecting the more accurate SPUF prediction of mass loss. Furthermore, the computational time for the SPUF predictions was an order of magnitude less than for the CPUF predictions.

Acknowledgements

Robert Kerr provided considerable help in making many of the tetrahedral meshes using CUBIT. Steven W. Bova provided the program to convert HEX elements to TET elements using the same node points. The authors also gratefully acknowledge the technical assistance provided by Steven T. Sorensen and Weston Carter for help with optimization and image processing. Scot Waye helped assemble Figs. 9.1-9.19. We would also like to thank Ken Erickson, Tom Fletcher (BYU), and Dan Clayton (BYU) for providing TGA data, which we used to obtain model parameters. T.Y. Chu, K. R. Thompson, J. H. Bentz, J.G. Pantuso, W. Gill, and L.L. Humphries provided X-rays and temperature measurements for the radiant heat experiments. We are also thankful for comments from internal reviewers at Sandia National Laboratories, Dean Dobranich, Ken Erickson, Roy E. Hogan, and Michael R. Prairie.

Table of Contents

List of Figures

List of Tables

List of Tables

Preface

A PolyUrethane Foam (PUF) decomposition chemistry model was developed from December 1996 to May 1997. At that time, the PUF decomposition chemistry model did not account for the spatial distribution of temperature (e.g. temperature gradients) and was used primarily to predict the temporal behavior of a small mass of foam exposed to a prescribed temperature boundary condition, such as in a ThermoGravimetric Analysis (TGA) experiment. The mass of the foam sample divided by the initial mass of the foam sample, or solid fraction, was determined for a prescribed temperature.

From Sept 1997 to February 1999, the PUF decomposition chemistry model was implemented into the 2D and 3D finite element heat conduction code COYOTE [1] that supports conduction, chemistry, and enclosure radiation and solves the energy equation using temperature-dependent thermophysical properties (thermal conductivity and specific heat). When the solid fraction within an individual element dropped below a set criterion (referred to as the death criterion), the element was removed from the computational domain. The combined decomposition mechanism implemented into the heat conduction code is referred to as a foam response model, as opposed to the decomposition chemistry model, which only describes the chemistry and kinetics of thermal decomposition of foam. Final documentation for the PUF decomposition chemistry model and foam response model was finished in November 1999 [3] and made available in the open literature in early 2000 [4].

The original PUF model did not consider discretization bias errors, which has been shown to be significant if element dimensions are greater than 100-μm. The PUF foam response simulations were performed using a 2D axisymmetric mesh using regular quadrilateral elements that were 0.5-mm by 0.5-mm. The error introduced by using these larger elements was probably on the order of 10-20%. In other words, the predicted decomposition front velocities using the larger elements were slower than the front velocities that would have been predicted if 100-μm elements had been used. However, using 100-μm elements in large system-scale calculations is impractical, even when dynamic enclosures are considered in 2D.

From March 1999 to January 2000, a Chemical-structure-based PolyUrethane Foam (CPUF) decomposition chemistry model and foam response model (also referred to as the CPUF model) was developed with a more accurate mass loss model [5]. The predicted and measured mass loss in various TGA analyses using the older PUF decomposition chemistry model gave an average root-mean-squared (RMS) error of about 8%. The RMS error for the CPUF decomposition chemistry model for the same set of experiments was about 2%. The CPUF model was further characterized by simulating the steady-state decomposition front velocity using a single row (or column) of elements. The row of elements where assumed to have adiabatic boundary conditions on all of the edges except for one edge that was exposed to a far-field radiation boundary condition at various temperatures. The uncertainty in the steady-state front velocity, calculated as the derivative of the predicted front location vs. time, was determined using both mean-value techniques as well as Latin Hypercube Sampling (LHS) techniques [5]. Numerical derivatives were obtained using small time steps with small element dimensions to give grid and time-step independent front velocities. The grid-independent velocities required characteristic mesh dimensions that were less than 100-μm.

A discretization bias correction model was formulated for use with the CPUF model to make grid-independent predictions of large-scale experiments. This subgrid discretization bias correction model enabled predictions using regular 2D quadrilateral elements with characteristic dimensions of 1-mm. The characteristic 1-mm dimension was thought adequate for boundary temperatures ranging from mild ambient conditions to high temperatures associated with hydrocarbon fuel fires. Hobbs et al. [5] also showed that the foam response *could also be corrected for* *larger characteristic element dimensions*. However, the bias correction used in the *CPUF model was only developed for characteristic dimensions of 1-mm*.

Meshing complex geometries with uniform 1-mm hexahedral elements is difficult for complex geometries. Meshes composed of uniform hexahedral elements are extremely hard to create and are typically never used in complex geometries for thermal analysis. Tetrahedral elements are easier to use than uniform hexahedral elements for filling three-dimensional geometries. Paved hexahedral elements are also useful for creating three-dimensional meshes but result in element sizes that are not uniform. Forcing the mesh to have uniform element sizes is not practical for realistic geometries and a subgrid discretization bias correction model is needed to correct foam decomposition solutions in nonuniform finite element meshes. To this end, the SPUF foam response model described in this report was developed using a simple mass loss model and a general discretization bias correction model for meshes that are made of either uniform or nonuniform finite elements of various sizes. The SPUF model greatly reduces computation time by allowing larger elements for grid independent solutions. The SPUF model also makes it possible to complete complex uncertainty analysis by providing an efficient method of simulating response of unconfined foam-filled systems.

Executive Summary

A Simple PolyUrethane Foam (SPUF) response model has been developed to predict the fire-induced response of unconfined foam-filled systems, where encapsulated components are restrained within unsealed metal enclosures. The enclosure may have openings used for cables without sufficient sealing to retain decomposition gases. The SPUF model does not predict pressurization or liquid formation associated with confinement. Confinement refers to whether or not the decomposition gases remain in the enclosure. Unconfined decomposition occurs in systems that do not constrain the decomposition gases within the enclosure. Even systems at elevated pressure are considered unconfined if a purge gas is used to sweep decomposition gases out of the system.

The SPUF model is the third model in a series of research efforts aimed at describing foam response in unconfined systems. The previous two models were referred to as the PolyUrethane Foam (PUF) and the Chemical-structure-based PolyUrethane Foam (CPUF) response models. The two predecessor models (PUF and CPUF) where based on complex bond breaking mechanisms, lattice statistics, and vapor-liquid equilibrium with the goal of providing a framework that can eventually be used to predict the composition of the evolving decomposition gases needed to calculate the pressure increase resulting from decomposition products. However, the kinetic parameters for both the PUF and CPUF models were only determined with mass loss data since quantitative composition data for either the condensed-phase or gas-phase were not available.

The only information provided by the chemical decomposition model to the finite element foam response model is the predicted mass loss based on the solid fraction within each element. The solid fraction is defined as the condensed mass in the element divided by initial condensed mass in the element. When the solid fraction drops below a specified criterion, referred to as the death criterion, the element is removed from the computational domain; and the radiation boundary conditions are inherited by the underlying elements. The decomposition model can be significantly simplified for unconfined decomposition since the foam response model does not depend on the composition of the offgas. This simplification is the basis for the acronym, SPUF, which refers to a Simple PolyUrethane Foam response model.

The SPUF decomposition mass loss model improves upon the discretization bias correction model used in the PUF and CPUF foam response models. The discretization bias correction model used in SPUF is based on the same model used in CPUF, but is valid over a larger range of element sizes, dimensions, and shapes. The SPUF model has been parameterized using characteristic element edge sizes from 1-mm to 1-cm.

The SPUF model has been compared to grid-independent solutions of a strand of decomposing foam using 2D, 2D axisymmetric, and 3D elements. The 2D meshes were composed of regular quadrilateral elements, paved quadrilateral elements, and triangular elements. The 3D meshes were composed of regular hexahedrons, paved hexahedrons, and tetrahedron elements. Various effects including element aspect ratio and the element death criterion were studied. Most of the solutions performed with irregular, large elements were in agreement with 100-μm grid-independent solutions. The discretization bias correction model did not perform well when the element aspect ratio exceeded 5:1 and the heated surface was on the shorter side of the element. If the element with the unusually high aspect ratio was used in a paved mesh surrounded by elements of different sizes, the aspect ratio performed as well as the more uniform elements.

The SPUF model was used to simulate several large-scale radiant heat experiments. These SPUF simulations were compared to CPUF simulations performed using uniform, or perfectly square, 1-mm hexahedral elements. The location of the decomposition front compared favorably to the CPUF predictions, but the computational savings was significant for the SPUF model that used a more simple mass loss model and larger elements with a generalized bias correction model. In fact, the SPUF model gave better predictions of the radiant heat experiments than CPUF predictions when comparing the calculated front locations to the front locations determined from X-ray images. Typical computational times (referred to as CPU time) for the 2D axisymmetric radiant heat experiments were 10 hours for the CPUF model on a single processor and 1 hour for the SPUF model using 1-cm elements.

Of the three unconfined foam response models; PUF, CPUF, and SPUF; SPUF is the most accurate and most computationally efficient for describing the response of unconfined rigid polyurethane foam systems exposed to fire-like conditions, at least with respect to the reaction front. If the decomposition products are sufficiently confined (i.e., remain in sufficient contact with the degrading foam), then none of the three foam response models (PUF, CPUF, or SPUF) have the required physics necessary to simulate the response of the confined-foam. A better approach for confined systems would probably be a combination of the CPUF (chemical-structure based) and SPUF (general discretization bias correction) models with additional physics to account for off gas composition, mass transport, liquefaction, pressurization, and flow.

Nomenclature

Abbreviations

2D	Two-dimensional
3D	Three-dimensional
BYU	Brigham Young University
CDF	Cumulative distribution function
CPU	Central processing unit
CPUF	Chemical-structure-based polyurethane foam decomposition model
DAKOTA	Design analysis kit for optimization
FE	Finite element
FEM	Finite element model
HEX	3D hexahedral element
HPTGA	High-pressure thermogravimetric analysis
LPTGA	Low-pressure thermogravimetric analysis
PDF	Probability density function
PUF	Polyurethane foam decomposition model
RMS	Root mean squared
RPU	Rigid polyurethane foam
SNL	Sandia National Laboratories
SPUF	Simple polyurethane foam response model
TET	3D tetrahedral element
TGA	Thermogravimetric analysis
TRI	2D triangular element
QUAD	2D quadrilateral element

Chemistry

Foam	Progress variable representing the initial foam
G_1	Progress variable representing the primary gas
G_2	Progress variable representing the secondary gas
S	Progress variable representing the degraded solid

Miscellaneous Variables

A_j	Pre exponential factor for the j^{th} reaction
bias	Discretization bias correction factor
C_p	Specific heat of the foam
E_1	Activation energy for the first reaction
E_2	Activation energy for the second reaction
E_j	Activation energy for the j^{th} reaction
Φ	Cumulative distribution function of a standard normal random variable
Φ	Extent of reaction
γ_i	Scaled-sensitivity coefficient
γ^2_i	Importance factor for the i^{th} parameter
h_r	Reaction enthalpy of the foam
I	Total number of species
J	Total number of reactions
k	Thermal conductivity of the foam
k_1	Distributed Arrhenius rate constant for the first reaction
k_2	Distributed Arrhenius rate constant for the second reaction
k_j	Distributed Arrhenius rate constant for the j^{th} reaction
$k_{250°\mathrm{C}}$	Measured conductivity at 250 °C
$k_{3500°\mathrm{C}}^{\mathrm{bias\ corrected}}$	Bias corrected extrapolated thermal conductivity at 3500 °C
$k_{3500°\mathrm{C}}^{\mathrm{linear\ extrapolation}}$	Thermal conductivity linearly extrapolated to 3500 °C from experimental data

Nomenclature

k_j	Arrhenius reaction rate coefficient for the j^{th} reaction
K-value	Vapor liquid equilibrium ratio
L	Liquid
m	mass
m_o	Initial mass
μ	Vector representing the mean value of the SPUF model input parameter
μ_{Sf}	Mean solid fraction
μ_V	Mean decomposition front velocity
P	Thermodynamic pressure
π	Pi constant (3.14159)
q_j	Volumetric energy release for reaction j
ρ	Foam density
ρ_o	Initial foam density
R	Gas constant
r_1	Rate expression for the first reaction
r_2	Rate expression for the second reaction
r_j	Rate expression for the j^{th} reaction
S_f	Solid fraction
$s_{f,i}^{SPUF}$	Solid fraction, initial solid mass divided by solid mass calculated with the SPUF model at various temperature points *i*
$s_{f,i}^{TGA}$	Solid fraction, initial solid mass divided by solid mass measured in a TGA experiment at various temperature points *i*
σ_1	Standard deviation parameter used in the distributed activation energy model for reaction 1
σ_2	Standard deviation parameter used in the distributed activation energy model for reaction 2
σ_{Ej}	Standard deviation parameter used in the distributed activation energy model
σ_i	Standard deviation of the i^{th} SPUF model input parameter
σ_{Sf}	Standard deviation of the solid fraction
σ_V	Standard deviation of the decomposition front velocity

Nomenclature

T	Temperature
T_o	Initial foam temperature
t	Integration variable
t	Time
V	Decomposition front velocity
V	Vapor
$V_{100\mu m}$	Steady-state velocity calculated with 100-μm elements
$V_{large\ element}$	Steady-state velocity calculated with large elements
x	Spatial coordinate
y	Spatial coordinate
y	Characteristic dimension
z	Spatial coordinate
ξ	Vector representing the SPUF model input parameters
z	Number of standard deviations

SPUF – A SIMPLE POLYURETHANE FOAM MASS LOSS AND RESPONSE MODEL

1. Introduction

This report describes a model for predicting the decomposition of unconfined, rigid, closed-cell, polyurethane foam based on a simple two-step mass loss chemistry model using distributed Arrhenius activation energies. The Simple PolyUrethane Foam (SPUF) decomposition model simulates decomposition of polyurethane foam based on the assumption that the initial foam reacts to form a stable gas and a reactive solid. The reactive solid subsequently decomposes into a final stable gas. The mass loss predicted by this simple two-step model is used in a finite element code to determine when elements should be removed from the computational domain forming a dynamic radiation enclosure. The SPUF decomposition model was implemented into two different finite element frameworks, referred to as COYOTE [1] and CALORE [2]. COYOTE was used for various 2D and 3D simulations and CALORE was used for several 3D simulations.

Two foam response models have been developed previously for unconfined decomposition of polyurethane foam – PUF [3,4] and CPUF [5]. These models (PUF and CPUF) present a framework to determine gas composition necessary to predict dynamic pressurization in closed, confined systems. The PUF and CPUF models consider lattice statistics, complex-bond breaking mechanisms, and vapor-liquid equilibrium. The emphasis for developing the PUF and CPUF chemistry models was to show the necessary framework rather than to provide accurate mass loss predictions for foam response. The SPUF model was developed specifically with the goal of predicting accurate mass loss that is necessary to describe unconfined foam response. The SPUF model does not predict the evolving composition of either the condensed-phase or the gas-phase. This report also describes the methods used to determine the various SPUF model parameters, several sensitivity and uncertainty analyses of the SPUF model, and a general discretization bias correction needed for multidimensional problems. The report also includes comparisons between the SPUF model and CPUF model by comparing predictions with several experiments at different scales from different laboratories.

2. Background

The SPUF model is a simplification of two previous decomposition foam chemistry models that were based on polymer fragmentation kinetics coupled to lattice statistics and vapor-liquid equilibrium: the PUF [1] model developed in the mid 1990's and the CPUF model [2] developed in the late 1990's. Foam response was characterized by mass loss, which was predicted using detailed decomposition models. Details of the evolving condensed-phase composition and gas-phase composition were not used in the final foam response model since the foam was considered unconfined and pressurization was not predicted.

The Engineering Sciences Center's foam material response program began in 1995 with the goal to develop a high fidelity computational tool for fire-induced thermal response of systems containing rigid, closed-cell polyurethane foam encapsulants. The foam was used to encapsulate components that were retained in an external metal enclosure (skin). The combined thermal, chemical, and mechanical response of the foam, components, and the enclosure contributes to the overall system response.

Rigid polyurethane foams are used as encapsulants to isolate and support components within weapon systems. When exposed to abnormal thermal environments, such as fire, various encapsulated components are designed to fail sequentially. The failure of these components is related to exposure to high temperatures, which may be affected by the behavior of the foam. Modeling foam decomposition is a difficult problem, not only because of the numerical challenges associated with steep reaction fronts, but also because of the difficulty of describing important chemical and physical processes, such as fluid flow. In the current report, thermal transport and simple mass loss chemistry are discussed in detail. The quantitative effects of mass transport, species diffusion, bubble mechanics, fluid flow, and gravitational effects are beyond the scope of this report. However, experiments are discussed that show the importance of these various phenomena.

Prior to 1995, simplifying assumptions regarding foam decomposition were made when predicting the thermal response of encapsulated components. For example, the decomposition of foam was ignored by assuming the foam was not present and adjusting surface emissivity to match thermocouple data, or by changing physical properties of the foam at prescribed temperatures. Such simplifying approximations were necessary given the computational limitations of the day. With the advent of massively parallel computers, high-consequence predictions of foam decomposition can be made with a more fundamental foam decomposition model, founded on experimental observations, to determine accurate decomposition rates, decomposition species, and physical properties of the evolving solid residue.

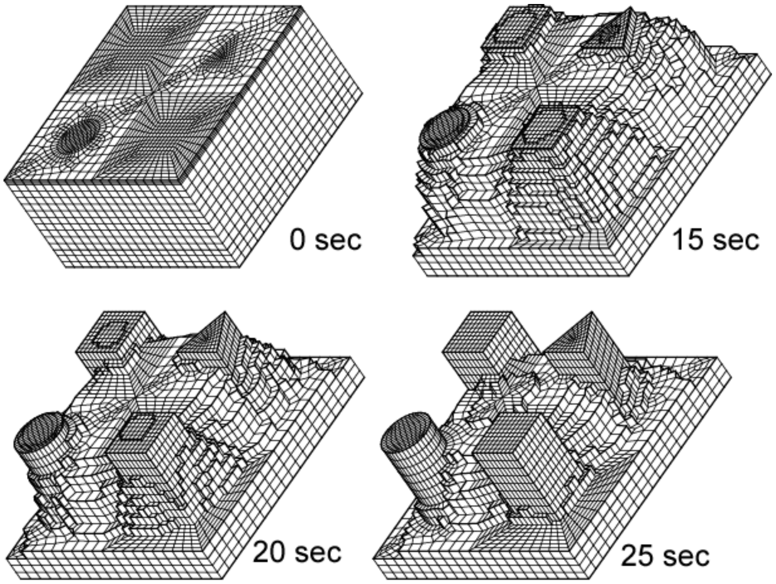

Fig. 2.1. Example calculation of inert components encapsulated in rigid polyurethane foam initially at 100°C exposed to a constant flux on the entire exposed surface. Elements were removed when element temperature exceeded 150°C. Although foam regression is shown as a function of time, a decomposition model was not used for this calculation. Figure used with permission from Gartling [6].

Computational models used in hazards analysis at SNL are designed to accommodate mass loss associated with foam decomposition. For example, Fig. 2.1 shows a COYOTE [1] finite element calculation of a block of material containing inert components of various shapes exposed to a constant energy flux. In this calculation, the encapsulating material was assumed to decompose by removing elements from the computational domain based on the element exceeding a specified temperature, without using a realistic decomposition mechanism. Actual tests of polyurethane foam exposed to abnormal thermal environments, such as fire, show the system response to be more complex.

The remainder of this report is divided into 8 additional sections. Section 3 describes the simple two-step chemical mechanism used to describe mass loss that is used by the Finite Element Models (FEM). Section 3 also describes how the chemistry parameters were obtained. Section 4 discusses comparisons between mass loss predictions and several TGA experiments. Section 5 describes the methods used to determine the remaining model parameters, which include thermophysical properties. Section 6 presents 1D strand calculations that show the dependence of the decomposition front velocity on the characteristic element dimensions. Section 6 also describes a general discretization bias correction model to allow accurate simulations using larger elements with varying aspect ratios. Section 7 presents various simulations used to verify the discretization bias correction model. Section 8 describes the component-scale radiant heat experiment where decomposition front velocities were determined using X-rays taken at regular intervals for some of the radiant heat experiments. Section 9 presents SPUF simulations of 19 radiant heat experiments to show the effects of the 1) heat flux at two different densities, 2) orientation of the heated surface with respect to the gravity vector, 3) embedded components on the decomposition front for both high- and low-density foams, 4) confinement and backpressure. The SPUF simulations were made using several different sizes and types of elements. Computational requirements (CPU times) for the SPUF predictions are compared to CPU requirements for similar CPUF predictions to illustrate significant computational savings. Some general remarks close the report in a summary and conclusions section.

3. Kinetic Mechanism and Parameters

Figure 3.1 shows the decomposition behavior of a 4-mg sample of rigid polyurethane foam (RPU) heated at 20°C/min in BYU's HPTGA at ambient pressure [9]. The initial decomposition between 250°C and 350°C was originally modeled by Hobbs et al. [1,4] as decomposition of a primary polymer forming various gases and a thermally stable secondary polymer. The secondary polymer was assumed to decompose at temperatures above 350°C at a different rate. This approach gave a percent RMS error between measured and predicted mass loss of about 8%. To get better agreement between measured and predicted mass loss for use in the foam response model, the CPUF bond breaking mechanism [5] was formulated by assuming that the polymer was initially composed of primary and secondary bridges as well as primary and secondary sites. The primary bridges were allowed to degrade into other bridge-types by evolution of CO_2. The CPUF mass loss mechanism gives a percent RMS error of about 2%.

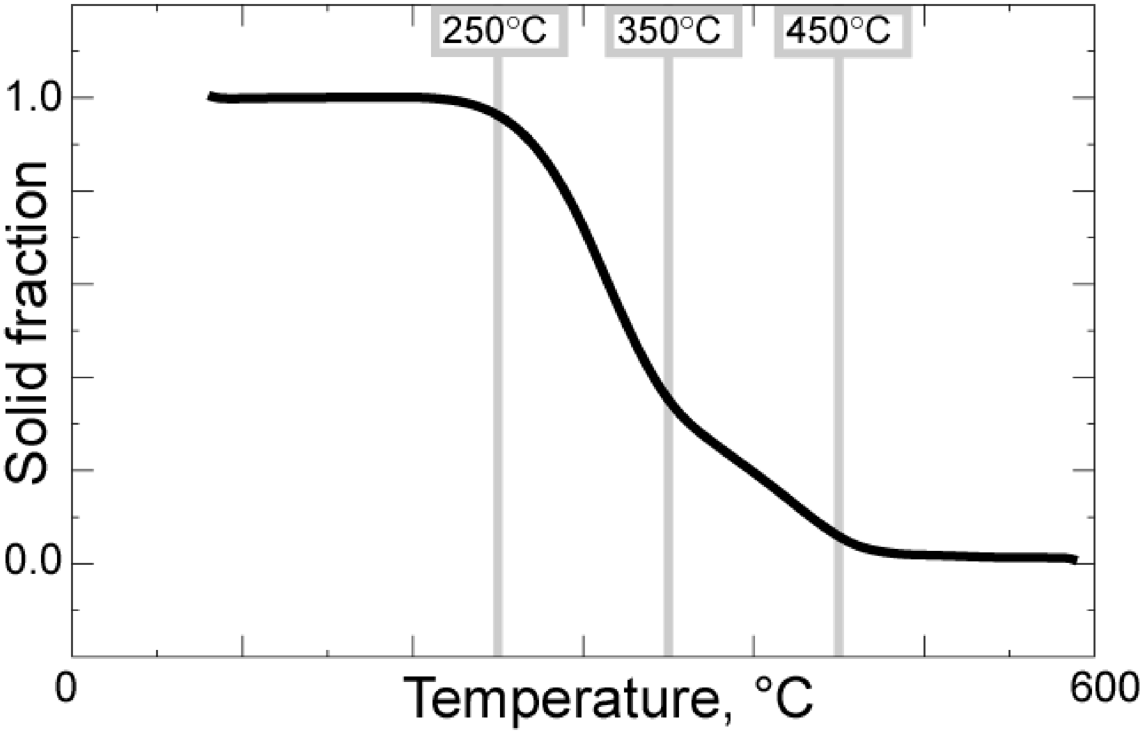

Fig. 3.1. TGA mass loss history for RPU foam at 1 bar ramped 20°C/min [9].

The % RMS error between predicted solid fraction using the PUF model with 9 reaction steps and measured mass loss for the experiment shown in Fig. 3.1 was about 8%. The same prediction using the CPUF model with 16 reaction steps gave a % RMS error of about 2%. These results suggest that better predictions can be obtained by increasing the number of reaction steps. However, the derivative of the solid fraction with respect to the temperature, as shown in Fig. 3.2, suggests that there are two primary mass loss reaction steps dominating the process. Two reaction steps should be sufficient to model mass loss accurately for the data shown in Figs. 3.1 and 3.2. The % RMS error for the two-step reaction (to be discussed later in this section) is about 1%, which is significantly better than either the PUF or CPUF predictions obtained by using a larger number of reaction steps, suggesting two rate-limiting reactions are sufficient to model mass loss for this material.

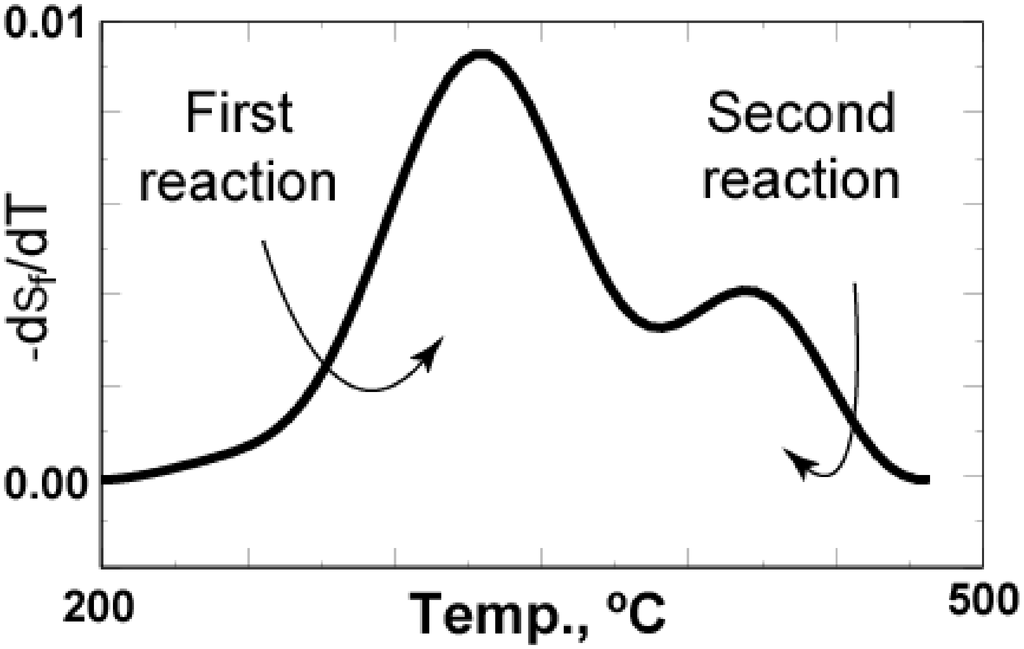

Fig. 3.2 Derivative of solid fraction with respect to temperature showing two dominating reaction pathways.

Kinetic Mechanism and Parameters

The general reaction mechanism for the SPUF decomposition model is:

$$Foam \rightarrow 0.7\, G_1 + S \qquad (1)$$

$$S \rightarrow G_2 \qquad (2)$$

where $Foam$, G_1, G_2, and S are mass based progress variables that represent foam, primary gas, secondary gas, and degraded solid, respectively. Mass based progress variables track the reaction in terms of mass fractions. For example, $Foam$ starts at unity and G_1, S, and G_2 start at zero. As $Foam$ progresses to zero, G_1 increases to 0.7. If all of S reacts to form G_2, the G_1 and G_2 gas mass fractions become 0.7 and 0.3, respectively. Details regarding the progress variables are given in the FORTRAN code in the Appendix.

The two Arrhenius reaction rates were distributed normally with respect to the extent of reaction. Distributing activation energies with respect to the extent of reaction is useful for approximating the effect of thermal damage on materials. Thermal damage may include mechanical damage such as cracks, fissures, density, and phase changes as well as chemical damage caused by thermal decomposition. The SPUF model considers distributed activation energies for each of the reactions described by Equations (1) and (2). During foam decomposition, each of the activation energies is normally distributed based on the extent of the reaction. For reaction 1, the activation energy is distributed based on the extent of reaction 1 as follows:

$$\Phi(z) = 1 - Foam = \int_{-\infty}^{z} \tfrac{1}{\sqrt{2\pi}} \exp(-\tfrac{1}{2}t^2)\,dt\,. \qquad (3)$$

For the second reaction, the activation energy is distributed based on the overall extent of the reaction set by defining the solid fraction as the sum of the foam and the reactive solid as:

$$S_f = foam + S$$

$$\Phi(z) = 1 - S_f = \int_{-\infty}^{z} \tfrac{1}{\sqrt{2\pi}} \exp(-\tfrac{1}{2}t^2)dt \,. \tag{4}$$

The cumulative distribution function (CDF), Φ, and the probability density function (PDF) of a standard normal random variable are shown in Fig. 3.3. Figure 2 also gives an example for an instance where the extent of reaction is 0.8413. In Fig. 2, the shaded area under the PDF corresponds to a Φ-value of 0.84113. Likewise a Φ-value of 0.8413 corresponds to a *z*-value of 2. Thus, when the extent of reaction is 0.8413, the activation energy is evaluated at the mean plus two standard deviations above the mean. For negative values of *z*, the relationship, Φ(-*z*) = 1 – Φ(*z*), is used. The distribution function initially starts at zero and ends at one.

For convenience, a table lookup is used for the distribution function rather than evaluation of the indefinite integral in Eqs.(3) and (4). Without any loss of accuracy, the following limits are used in the SPUF model for increased computational speed:

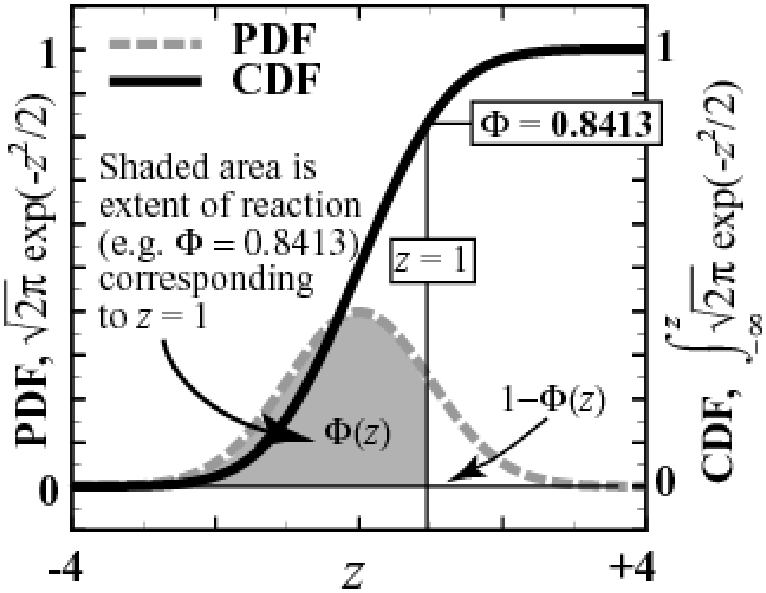

Fig. 3.3. Cumulative distribution function of a standardized normal random variable.

$$z = \begin{cases} -2 & \Phi < 0.0228 \\ +3.5 & \Phi > 0.9997. \end{cases} \tag{5}$$

For all other values of Φ, z is linearly interpolated from tables.

The reaction rates for the two-step SPUF kinetic mechanism were assumed to be first order in the initial foam and degraded solid, respectively. Reverse reactions that are significant when the foam is confined were not included in the SPUF kinetic mechanism. The two Arrhenius reaction rates are:

$$r_1 = k_1(foam) \tag{6}$$

and

$$r_2 = k_2(S). \tag{7}$$

The rate constants given in Eqs. (6) and (7) were modified to include the effect of the distributed activation energies as follows:

$$k_j(T) = A_j \exp\left[-\left(E_j + z\sigma_{E_j}\right)/RT\right]. \tag{8}$$

Distributing the activation energies tends to smooth the mass loss reaction rates and eliminates abrupt changes in calculated solid fractions, which is in agreement with experimental observations.

Eighteen TGA experiments are listed in Table 3.1. The TGA experiments in Table 3.1 were used to obtain the activation energies and standard deviations used in the distributed activation energy model. The pre-exponential factors, A_i, were assumed to be 1×10^{13} s^{-1}. The first fourteen experiments were run at Sandia National Laboratories (SNL) in Albuquerque [6-8] and the last four experiments were run at Brigham Young University (BYU) [9]. The average sample mass was 5.1-mg with a standard deviation of 0.8-mg. Activation energies and standard deviations were obtained for each of the experiments listed in Table 3.1 by minimizing the absolute error between the predicted solid fraction and the measured solid fraction in the following manner:

$$\text{Absolute RMS error} = \sqrt{\sum_{i=1}^{n}\left(S_{f,i}^{TGA} - S_{f,i}^{SPUF}\right)^2}\ . \tag{9}$$

Table 3.1 also gives the average activation energies and standard deviations for each of the chemistry parameters. The standard deviations can be used in a simple mean value analysis to propagate the uncertainty associated with the chemistry into the SPUF predictions. Table 3.1 lists the % RMS error for each of the experiments. The average % RMS error using parameters used for the individual experiments is 0.8%. The average % RMS error using the mean parameter values is 1.4%. The mean parameters are used in the remainder of this report. The standard deviations listed in Table 3.1 were used to determine 95% prediction intervals.

Table 3.1. Arrhenius parameters for SPUF model

Run*	Sample	m_o, mg	E_1	E_2	σ_1	σ_2	†Error	‡Error
1	F_062199	4.498	41500	44600	1180	3110	0.0089	0.0134
2	Fm061499	5.135	41200	45700	1090	3140	0.0050	0.0121
3	Foam1112	6.162	41700	45500	1180	2800	0.0091	0.0170
4	Foam1114	6.079	41600	45500	1130	2810	0.0112	0.0201
5	Foam1117	4.477	41400	45100	1080	3140	0.0103	0.0103
6	Foam1118	4.51	41400	45100	1080	3140	0.0098	0.0098
7	Foam1119	4.469	41600	45400	1260	2770	0.0076	0.0130
8	Foam1202	5.236	41500	45200	1090	3130	0.0098	0.0134
9	Foam1204	4.687	41500	45200	1090	3130	0.0078	0.0094
10	Foam1205	4.561	41500	45400	1150	3030	0.0076	0.0129
11	fm102999	5.976	41500	45200	1090	3130	0.0109	0.0129
12	fm103099	6.136	41800	45700	1160	2990	0.0190	0.0264
13	fm110199	4.062	41500	45200	1090	3130	0.0071	0.0096
14	fm11019a	4.008	41500	45200	1090	3130	0.0063	0.0086
15	BYUA051000	6.327	41200	44700	881	3510	0.0051	0.0115
16	BYUB051000	5.176	41000	44400	887	3550	0.0051	0.0207
17	BYUA051100	5.169	41300	44700	1070	3450	0.0061	0.0084
18	BYUB051100	5.496	40900	44500	855	3390	0.0050	0.0212
	Mean =	**5.12**	**41400**	**45100**	**1080**	**3140**	**0.0084**	**0.0139**
	St. Dev. =	**0.76**	**229**	**397**	**107**	**225**	**0.0034**	**0.0051**

*1-14 run at SNL; 15-18 run at BYU

†Error calculated with individually optimized E_i and σ_i

‡Error calculated with mean E_i and σ_i

4. TGA Experiments and Predictions

The TGA apparatus is composed of 1) a microbalance used to measure mass loss associated with thermal decomposition, 2) a thermocouple in close proximity to the sample to determine sample temperature, and 3) purge gas to sweep away decomposition gases from the surface of the sample. Sample sizes were chosen to minimize size effects and to maximize the signal-to-noise ratio. A high thermal conductivity purge gas was needed in the high-pressure thermogravimetric analysis (HPTGA) experiment to insure that the thermocouple temperature was sufficiently close to the sample temperature. Erickson et al. [6-8] and Clayton [9] give more information regarding the low-pressure thermogravimetric analysis (LPTGA) and HPTGA experiments, respectively.

The TGA records the sample mass (m) versus temperature or time. Typically, the normalized sample mass or solid fraction ($S_f = m/m_o$) is plotted as a function of temperature if the sample is ramped at a constant heating rate. If the sample is held at a constant temperature, the normalized sample mass is plotted as a function of time. The TGA experiments discussed in the current report were performed using a variety of heating conditions that included nonisothermal "ramped" experiments as well as "isothermal" experiments. The temperatures of the samples in the ramped experiments were increased at constant heating rates (5ºC/min, 20ºC/min, and 50ºC/min) from ambient temperature to about 575ºC.

Two types of isothermal experiments were considered – "one-step isothermal" and "two-step isothermal" experiments. The "one-step isothermal" experiments addressed samples heated from ambient temperature at a constant rate of 20ºC/min to a temperature of 300ºC; the sample temperature was then held at 300ºC for one hour or longer. The "two-step isothermal" experiments addressed samples heated from ambient temperature at a constant heating rate of 40ºC/min to a temperature of 300ºC; the samples were then held at 300ºC for one hour or longer. Following this first constant temperature period, the "two-step isothermal" samples were then heated from 300ºC to 400ºC at a rate of 40ºC/min, the samples were then held at a second constant temperature period of one hour or more at 400ºC. The three nonisothermal ramped experiments in this report are referred to as 5, 20, and 50 representing temperature ramp rates of 5ºC/min, 20ºC/min, or 50ºC/min. The isothermal experiments are referred to as 250, 270, 300, and 300/400 representing a 250ºC one-step isothermal experiment, a 270ºC one-step isothermal experiment, 300ºC one-step isothermal experiment, and a 300ºC/400ºC dual isothermal experiment, respectively.

The mean value method [10,11] was used to calculate the mean and standard deviation of the solid fraction as a function of the heating conditions by assuming that the input parameters are independent random variables and that the response is linear. The mean solid fraction, μ_{Sf}, and the standard deviation of the solid fraction, σ_{Sf}, was determined using a simple Taylor series expansion of solid fraction, $S_f(\xi_i)$, about the mean of the individual random variables or input parameters, μ_i, by neglecting higher order terms as follows:

$$\mu_{S_f} = S_f(\xi)\big|_{\xi=\mu} \tag{10}$$

$$\sigma_{S_f}^2 = \sum_{i=1}^{n}\left[\sigma_i \frac{\partial S_f(\xi)}{\partial \xi_i}\Big|_{\xi=\mu}\right]^2 . \tag{11}$$

Equation (10) is a single-sample approximation of the mean solid fraction calculated as a function of temperature with the finite element model with all input parameters, ξ, equal to the mean values, μ. In Eq.(11), σ_{Sf} is the standard deviation of the solid fraction; σ_i is the standard deviation of the i^{th}-input parameter (random variable); and μ is a vector representing the mean input parameters.

The relative importance of each input variable to the uncertainty in the calculated solid fraction can be determined from the scaled sensitivity coefficients, γ_i, defined as:

$$\gamma_i = \frac{\sigma_i}{\sigma_{s_f}} \times \frac{\partial S_f(\xi)}{\partial \xi_i}\,, \tag{12}$$

where

$$-1 \le \gamma_i \le 1 \tag{13}$$

and

$$\sum_{i=1}^{n} \gamma_i^2 = 1\,. \tag{14}$$

The input variables that contribute the most to the uncertainty in the calculated solid fraction also have the largest absolute sensitivity values. The sign of the scaled sensitivity coefficients indicate that an increase in the input parameter value causes an increase in the value of the response function or solid fraction. Likewise, a negative sensitivity coefficient indicates that an increase in the input parameter value causes a decrease in the response function value. The square of the sensitivity coefficient is referred to as the importance factor, γ_i^2, which can be used to easily identify important input variables that contribute to the calculated uncertainty. The term “importance factor” is a misnomer. The importance factor only shows the relative importance of a parameter with respect to the uncertainty calculation. All model parameters are important and necessary to determine the foam response. The importance factors merely indicate which parameters contribute most to the response uncertainty. The importance factors are highly dependent on the estimates of the individual parameter uncertainty expressed in this report as a standard deviation.

Thermophysical properties are not needed to calculate the solid fraction when the temperature history of the sample is known. The primary variables that contribute to the standard deviation of the solid fraction for the ambient pressure TGA simulations are the activation energies (E_i) and the distributed activation energy parameter (σ_E). The derivatives in Eq. (11) were obtained using a central differencing technique with a finite difference step size of 0.01 times the mean input parameter. Nine function evaluations were required to obtain the derivatives for the ambient pressure experiments: two for each of the 2 activation energies, two for each of the distributed activation energy parameters, and one evaluation using the mean input values.

Figure 4.1 shows the predicted and measured mass loss for samples heated at various heating rates (5, 20, and 50ºC/min). All of the experiments were run with “low-density” samples

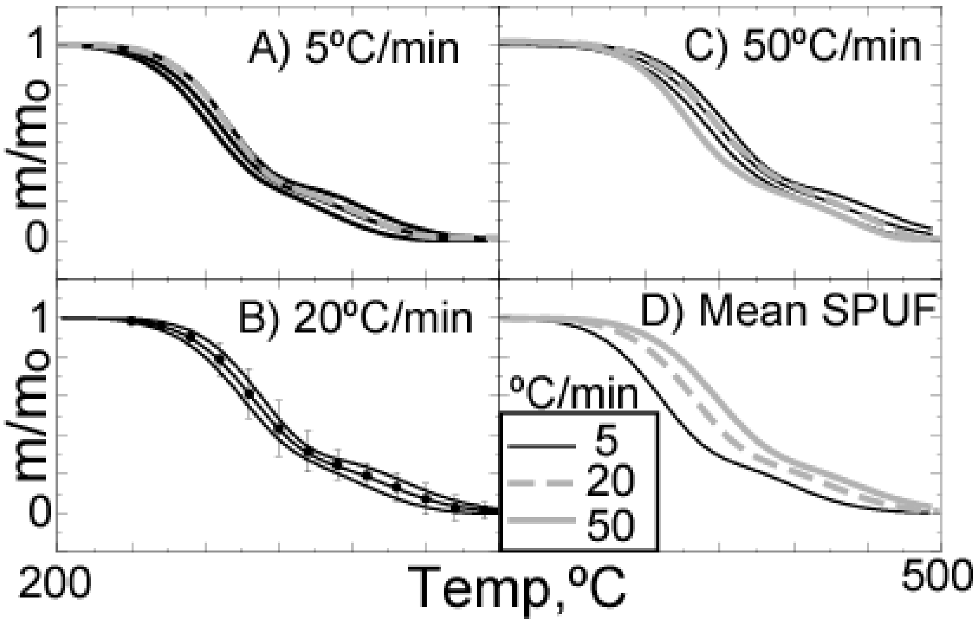

Fig. 4.1. Comparison between SPUF predicted and measured solid mass fraction for various heating rates. The black lines in A-D and the gray lines in D are SPUF predictions. In A-C, the middle black lines represent the mean and the outer black lines represent the 95% prediction interval. The gray lines in A and C and the symbols in B represent experimental data.

that were nominally 0.19 g/cm^3 (12 lb/ft^3), except for sample Foam0410 (Fig 4.1.C, dashed gray line), which had a nominal density of 0.4 g/cm^3 (25 lb/ft^3). The middle black line is the mean prediction and the outer two black lines represent the 95% prediction interval. The symbols in Fig 4.1.B represent the mean measured solid fraction and the error bars represent the 95% confidence interval. The 95% prediction interval (based on the SPUF model) is similar to a 95% confidence interval (based on data). The response is assumed to be normally distributed with the 95% prediction interval based on adding and subtracting $2\times\sigma_{sf}$ from the mean response, μ_{sf}. In this report, the term *prediction interval* will be used when the uncertainty is based on a *model prediction*. The term, *confidence interval* will be used when the response is based on *data*. The model response uncertainty is based on the uncertainty (standard deviations) of the 2 activation energies and the distributed activation energy model parameters given in Table 3.1.

Some of the unconfined TGA samples (nominally 5-mg) were heated isothermally in open platinum pans. Figure 4.2 shows a comparison between predicted and measured solid fractions for various isothermal TGA experiments. The 250°C samples were ramped from room temperature (27°C) to 250°C in about 14 minutes; the 270°C samples were ramped from room temperature to 270°C in about 14 minutes; the 300°C samples were ramped from room temperature to 300°C in about 16 minutes; and the dual isothermal samples were ramped from room temperature to 300°C in 8 minutes, held for 2 hours, ramped to 400°C in about 4 minutes and held at 400°C temperature for 4 hours. The measured mass loss from each of the isothermal experiments is within the 95% prediction interval.

Figure 4.3 shows the TGA mass loss profile and importance factors for a sample temperature ramped at 20ºC/min. The 95% prediction limit for the SPUF model and the 95% confidence limit for the data are also shown in Fig. 4.3.A. The importance of the chemistry parameters for the SPUF model are shown in Fig. 4.3.B. The importance factors shown in Fig 4.3.B provide

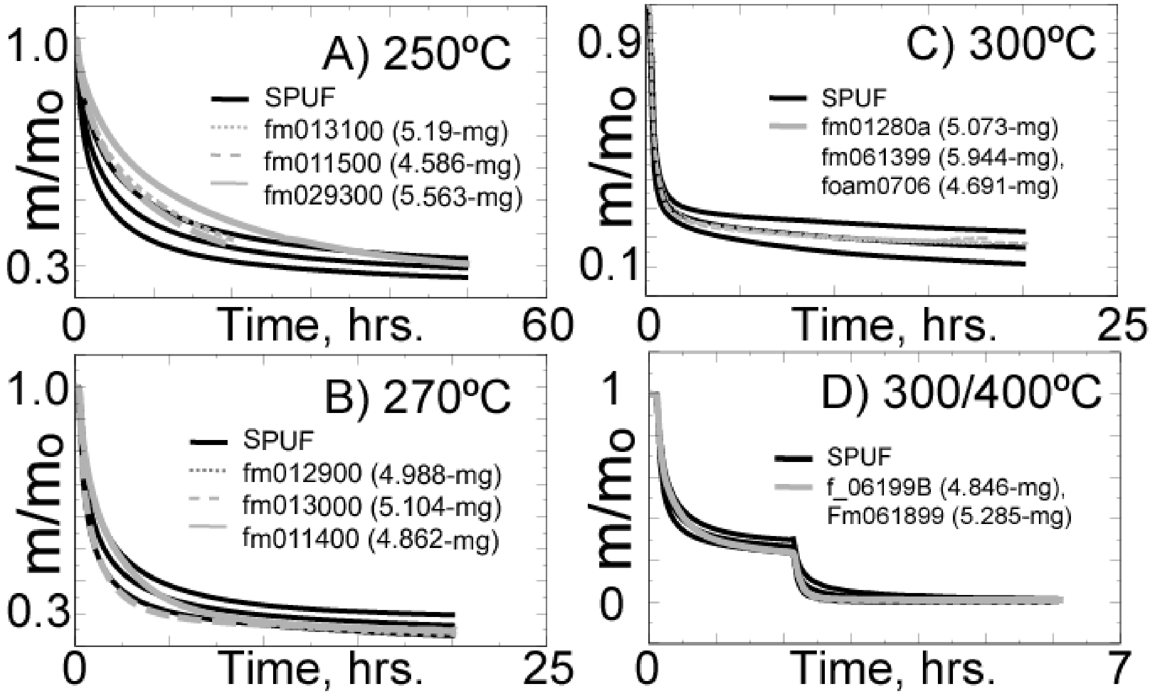

Fig 4.2. Comparison between SPUF predicted (3 black lines) and measured (gray lines) solid mass fraction for various temperature histories at ambient pressure. The middle black lines represent the mean and the outer two black lines represent the 95% prediction interval. The legend gives the name of the experimental run as well as the initial mass of the sample (m_o). The sample temperatures were ramped at 20°C/min and held at A) 250°C for 50 hours, B) 270°C for 20 hours, and C) 300°C for 18-20 hours. In D, the sample temperatures were ramped at 40°C/min to 300°C and held for 2 hours, and then the temperatures were ramped at 40°C/min to 400°C and held for 4 hours.

a measure of which input parameters contribute the most to the total uncertainty in the calculated solid fractions. The importance of a variable does not indicate whether the variable is significant or insignificant in the model. Instead, importance refers to the relative contribution each input parameter makes to the uncertainty of the calculated solid fraction or response, which is shown as the 95% prediction interval in Fig. 4.3.A. The chemistry parameters for reaction 1 dominate the uncertainty until the sample reaches about 350ºC; after which, the uncertainty is dominated by the second reaction. Progress variables are shown in Fig. 4.3.C.

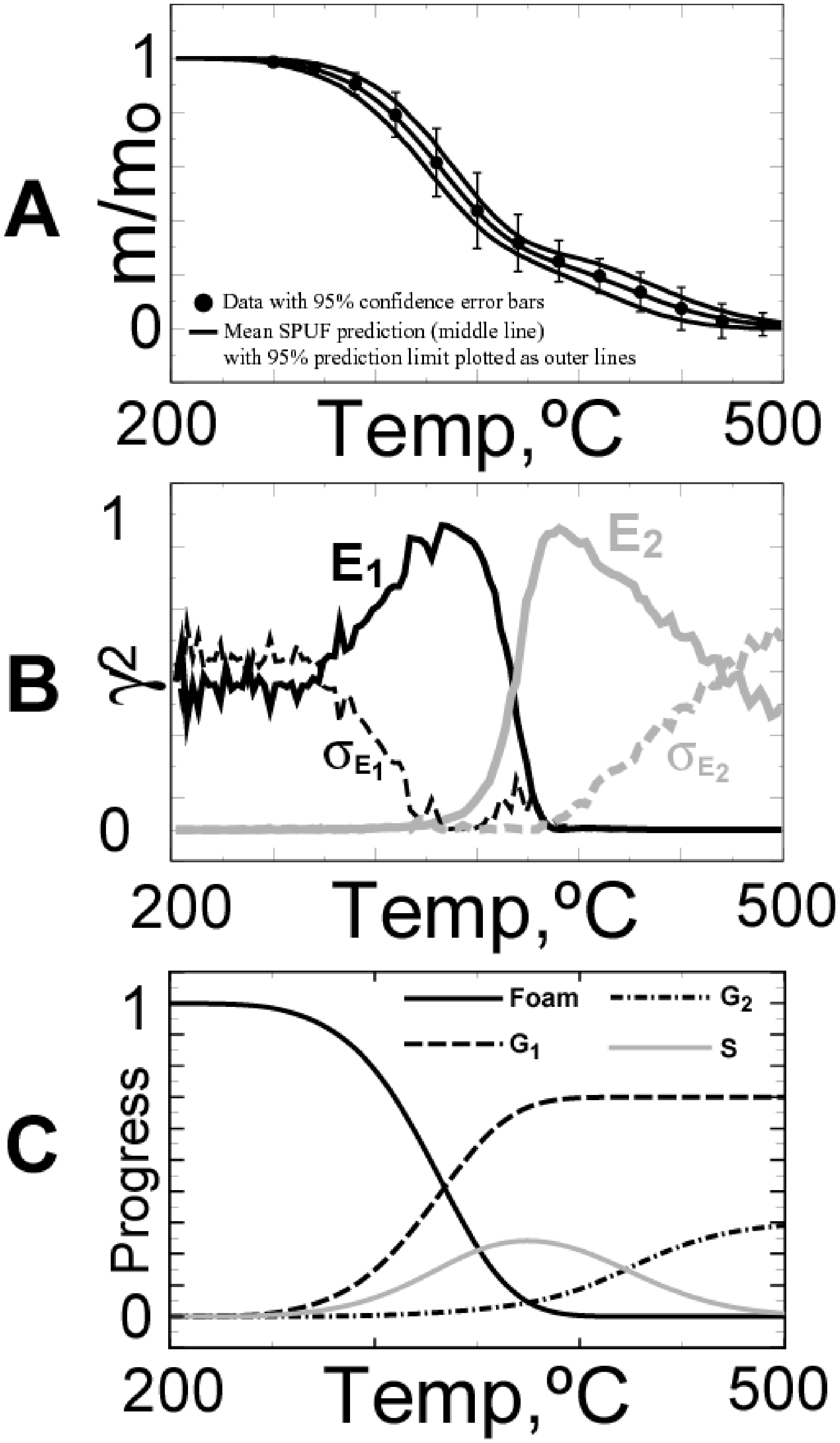

Fig. 4.3 A) predicted (lines, middle is mean and outer two represent the 95% prediction interval) and measured (symbols with 95% confidence intervals as error bars) solid fraction for sample ramped at 20ºC/min. B) Importance factors (see Eq. 14), γ_ι^2, for SPUF prediction interval in A. C) Progress variable for the mean prediction in A.

5. SPUF Model Parameters

Thermophysical properties are needed to model multidimensional foam response. Table 5.1 gives the means (μ_i) and standard deviations (σ_i) of the SPUF input parameters, which include the initial density and temperature of the foam (ρ_o and T_o), the multiplying factors for temperature-dependent thermal conductivity and specific heat of the foam (k and C_p), the reaction enthalpy of the foam (h_r), the emissivity of the foam (ε), the element death criterion (S_f^{death}), the 2 frequency factors (A_i), 2 activation energies (E_i), and the 2 standard deviation of the distributed activation energy model (σ_{Ei}). The chemistry parameters where discussed previously in Section 4. The input parameters are assumed to be normally distributed independent random variables.

All of the mean *thermophysical properties* in Table 5.1 are *based on measurements*. Densities were determined from the sample volume and mass. Initial temperatures were measured using embedded thermocouples. The thermal conductivity and specific heats were measured at Purdue's Thermophysical Properties Laboratory [12, 13] between 23ºC and 250ºC using 1.3-cm wide by 0.3-cm thick samples. The thermal conductivity and specific heat for samples with densities of 0.078-g/cm^3, 0.150-g/cm^3, and 0.352-g/cm^3 are given in Table 5.2. The reaction enthalpy was measured with a differential scanning calorimeter using a nominally 5-mg sample ramped at 20ºC/min. The foam emissivity was *estimated* from measurements at Purdue.

Table 5.1. Moments of various SPUF model parameters[†]

	Thermophysical						***Death***	***Chemistry***				
ξ_i	ρ_o	T_o	f_k[‡]	f_{cp}[‡]	h_r	ε	S_f^{death}	A_i	E_1	E_2	σ_{E1}	σ_{E2}
μ_i	0.364	300	1	1	-29.2	0.8	0.038	1×10^{13}	41.4	45.1	1.08	3.14
σ_i	0.02	3	0.09	0.04	1.0	0.04	0.01	0	0.229	0.397	0.107	0.225

[†] Density (ρ_o) in g/cm^3, initial temperature (T_o) in K, reaction enthalpy (h_r) in cal/cm^3, frequency factors (A_j) in 1/s, activation energies (E_i) in Kcal/mol, and standard deviation of the activation energies (σ_{Ei}) in Kcal/mol.
[‡] k and C_p are given in Table 5.2. f_k and f_{cp} are scaling parameters which can be used for uncertainty analysis.

Table 5.2. Thermal conductivity and specific heat for RPU foam at three densities [12-13]

	k, cal/s-cm-K			**C_p, cal/g-K**		
T, °C	**0.078 g/cm^3**	**0.150 g/cm^3**	**0.352 g/cm^3**	**0.078 g/cm^3**	**0.15 g/cm^3**	**0.352 g/cm^3**
23	5.7×10^{-5}	6.9×10^{-5}	1.4×10^{-4}	0.303	0.303	0.303
50	6.4×10^{-5}	7.6×10^{-5}	1.5×10^{-4}	0.324	0.324	0.324
100	7.4×10^{-5}	8.4×10^{-5}	1.6×10^{-4}	0.358	0.358	0.358
150	9.1×10^{-5}	9.8×10^{-5}	1.8×10^{-4}	0.440	0.440	0.440
200	9.8×10^{-5}	1.0×10^{-4}	2.0×10^{-4}	0.475	0.475	0.475
250	1.2×10^{-4}	1.2×10^{-4}	2.2×10^{-4}	0.526	0.526	0.526
3500*	9.1×10^{-4}	9.1×10^{-4}	1.3×10^{-3}	0.526	0.526	0.526

*Extrapolated thermal conductivity used in bias correction in Eq. (16) given as $k_{3500^\circ\mathrm{C}}^{\text{linear extrapolation}}$

Density. The variability in the initial foam density may be caused by a skin effect. For example, the density of cast blocks of polyurethane foam varies considerably from near the surface to the interior of the foam. The skin effect is greatest when the average density of the foam is high. Purdue measured from 1.4% to 23% difference in density between the machined samples used for the thermal conductivity measurements and the large blocks from which the samples were taken. The 1.4% difference was for the 0.078-g/cm^3 foam and the 23% difference was for the 0.150-g/cm^3 foam. Of course, these differences are based on significant skin effects that depend on the size of the bulk sample. The samples used in both the large and small-scale experiments were taken near the center of the foam block to avoid large edge effects. The density measured for the large-scale experiments was given in Table 5.1 (0.364 g/cc). The density used to determine the thermal conductivity was given in Table 5.2 (0.352 g/cc). These two different values were used to determine the standard deviation of the foam density [3.3% of the mean value = (0.364-0.352)/0.364]. The standard deviation of density in the current report was taken to be twice this value or 6.6% of the mean density. A larger uncertainty is used in the current report because the foam used in the application will be cast in place and may have a significant skin effect.

Initial temperature. The standard deviation of the initial foam temperature was based on the measured initial sample temperatures for both the small and large-scale experiments. For example, the mean initial temperature of the TGA experiments was 26ºC (299 K) with a standard deviation of 2.3ºC. The mean initial temperature of the large-scale experiments was 21ºC (294 K) with a standard deviation of 4.0ºC. For convenience, the nominal mean and standard deviation of the initial temperature was taken to be 27ºC (300 K) and 3ºC, respectively.

Thermal conductivity. The uncertainty in the thermal conductivity is based on multiple room temperature measurements using two different techniques – a laser flash diffusivity method and a heated probe method [12, 13]. The laser flash diffusivity method measures bulk conductivity and the heated probe method measures the conductivity parallel to the rise direction of the foam as well as orthogonal directions perpendicular to the rise direction of the foam. Three measurements were made at 23˚C for both the 0.078-g/cc samples and the 0.150-g/cc samples; and nine measurements were made at 23˚C for the 0.352-g/cc samples. The standard deviations for the 0.078-g/cc, 0.150-g/cc, and 0.352-g/cc samples were 9%, 4%, and 5% of the mean thermal conductivity value at 23˚C, respectively. The standard deviation was determined as a percent of the mean thermal conductivity to facilitate uncertainty analysis. The highest standard deviation (9% of the mean) was chosen to reflect the unknown variability at higher temperatures. Condensed-phase reactions and liquefaction are expected to cause the uncertainty in thermal conductivity to increase.

Specific heat. The specific heats of RPU samples preheated to 150 and 250˚ were measured with a differential scanning calorimeter with sapphire as the reference material. The samples were preheated to prevent contamination of the test cell with decomposition products. Variability in the specific heat is related to uncertainty caused by mass loss associated with decomposition. Polyurethane specific heat data were not available to estimate uncertainty. However, specific heat data for a different type of foam was taken multiple times by repeating the measurement on the same sample four times. The average and standard deviation of the specific heat at each temperature were determined using the four runs. The average standard deviation between ambient temperature and 200˚C was 3.7% of the mean specific heat value. The variability in the polyurethane specific heat (~4%) was assumed similar to the variability over the same temperature range.

Reaction enthalpy. Data from a differential scanning calorimeter (DSC) was used to determine the energy changes for conditions similar to the TGA experiments run at 20ºC/min. The overall endothermic heat of reaction at these conditions was about 100 cal/g [14] or 36.4 cal/cc for foam with a density of 0.364. The heat of reaction shown in Table 7.1, -29.2 cal/cc, is the reaction enthalpy used for both reactions. The sign is negative because the reaction is endothermic. The individual reaction enthalpies are probably not the same, but since only a single overall reaction enthalpy value was reported rather than time and temperature resolved energy changes, the reaction enthalpy for both reactions were assumed to be the same for simplicity.

The overall endothermic heat of reaction was used with the finite element code [1] to obtain the energy release for each reaction step j. The source term in the heat diffusion equation is used to account for the overall endothermic reaction enthalpy. The heat diffusion equation is

$$\rho C_p \frac{\partial T}{\partial t} = \frac{\partial}{\partial x}\left(k \frac{\partial T}{\partial x}\right) + \sum_{j=1}^{J} q_j r_j \ . \tag{15}$$

In Eq. (15), ρ, C_p, T, t, x, k, q, and r; represent material density, specific heat, temperature, time, spatial coordinate, thermal conductivity, endothermic or exothermic energy release for reaction step *j*, and the reaction rates given previously in Eqs. (6) and (7), respectively. Equation (15) was used iteratively with a 20ºC/min ramp to determine the individual heat of reaction values of -29.2

cal/cc that gives an overall reaction enthalpy of –100 cal/g or –36.4 cal/cc. Figure 5.1.A shows the volumetric heat release, $\sum q_j r_j$, plotted as a function of time for the 20ºC/min TGA run. Figure 5.1.B shows the integrated volumetric heat release, which converges to a value of –36.5 cal/cc or –100 cal/g. Different values of the energy release are expected at different heating rates to reflect the effect of the reaction mechanism on the overall energy release [5].

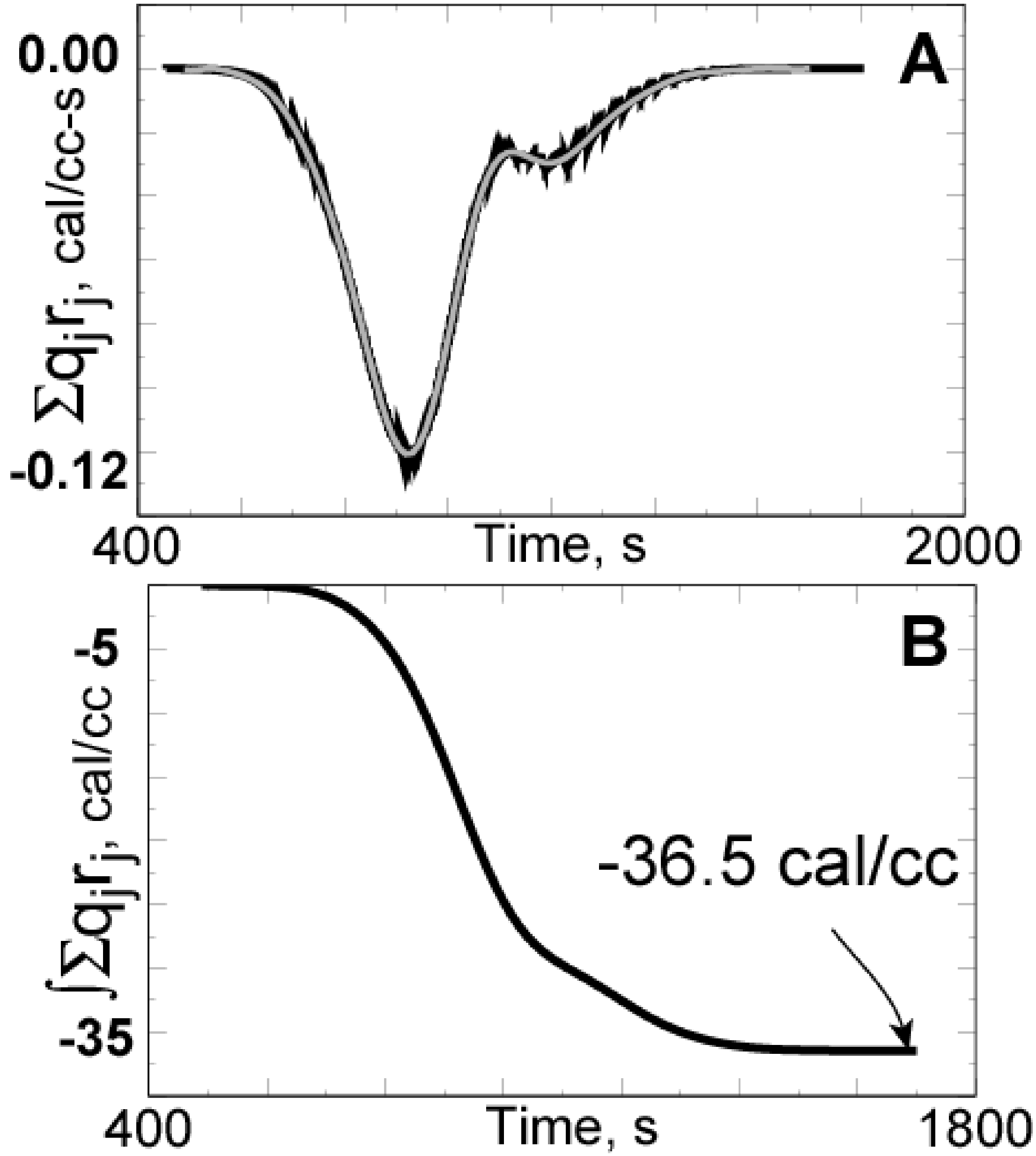

Fig. 5.1. A) SPUF predicted heat release for 0.364 g/cc sample heated at 20ºC/min, B) integrated volumetric heat release for 0.364 g/cc sample heated at 20ºC/min.

The uncertainty in the volumetric heat release is difficult to estimate because only one DSC experiment was performed at a heating rate of 20ºC/min. The density of the DSC sample was reported to be the same as the samples used in the TGA analysis [14]. The density of the DTA sample was assumed equal to 0.364 g/cc. However, the sample may have had a density of 0.352 g/cc, which is the density measured for the samples used to determine the thermal conductivity. The error associated with the assumed density is about 3.3% of the mean value. Thus, the standard deviation of the reaction enthalpy was taken to be 3.3% of the mean value, or 1.0 cal/cc (0.033×29.2 cal/cc).

Emissivity. The emissivity of the degraded foam surface was estimated because *no measurements were performed*. The rough surface of the foam was used to base the estimate of emissivity—rough surfaces, independent of color, typically have emissivities approaching unity. The postmortem color of the decomposed foam may also give an indication of the emissivity of the foam. The postmortem color of the decomposed foam was similar to the color of the interior surface of the confining skin, which was painted black with Pyromark Paint 2500. The hemispherical emissivity of this paint was between 0.768 and 0.811 at temperatures between 460ºC and 1,014ºC [12]. The emissivity of the foam was assumed to rapidly approach 0.8 with an estimated standard deviation of 0.04. The standard deviation of the foam emissivity was based on the range of the measured emissivity for the Pyromark Paint (0.04 = 0.81-0.77).

Element death criterion. Later in the report, element death will be used to model the decomposition of a strand of foam as well as several component-scale radiant heat experiments. In the FEM codes, COYOTE and CALORE, the solid fraction, m/m_o, is determined at each Gauss point and the average solid fraction is determined for each element. When the solid fraction within an element drops below a specified element death criterion, the element is removed from the computational domain and the surface boundary condition is applied to the newly exposed elements, which exchange energy via radiative heat transport.

In the FEM codes, elements were removed from the computational domain when a specified criterion was reached. Removal of an element from the computational domain is referred to as "element death". In this report, a solid fraction death criterion, S_f^{death}, was used to control the elimination of elements during the computation. The solid fraction calculated within each element is checked every iteration to determine if the element should be removed from the computational domain. If the calculated solid fraction within an element falls below the "death criterion", S_f^{death}, the element is removed from the computational domain. The death criterion is based on experimental observations.

The 20°C/min ramped TGA experiments were used to determine the appropriate value to use for the death criterion. Figure 5.2 shows how the death criterion was selected based on experiment Foam1114 and the SPUF predictions. Figure 5.2 shows the predicted and calculated

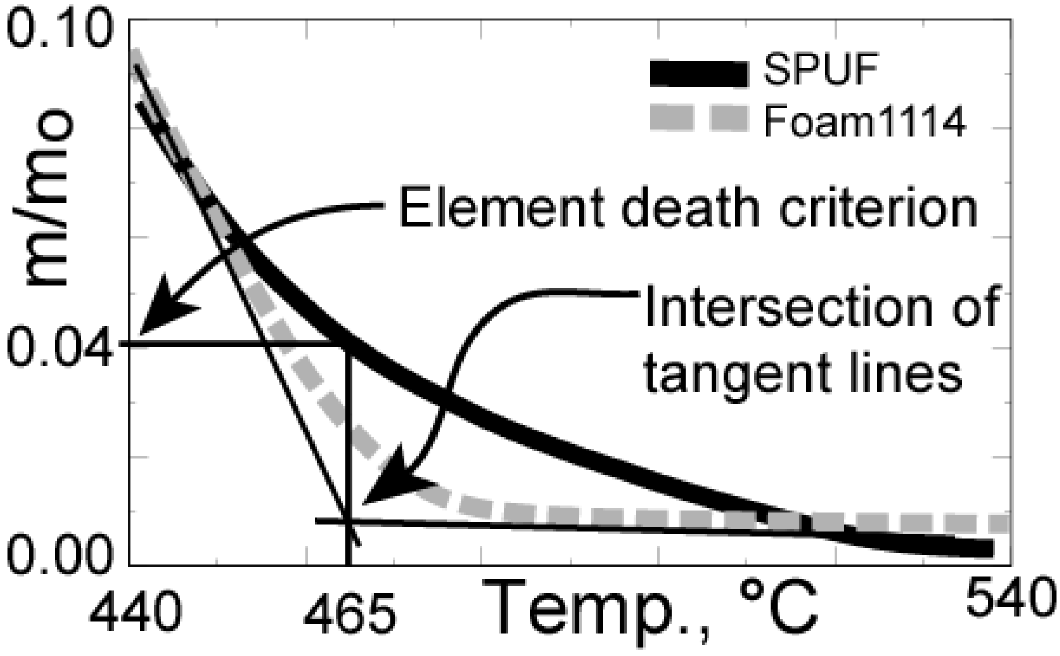

Fig. 5.2. TGA solid fraction contours near the end of decomposition. Tangent lines to the data intersect at 465ºC corresponding to the SPUF solid fraction (0.04) used as the element death criterion.

solid fraction when the sample is near the end of decomposition. At this point, a small amount of residue is left in the TGA pan, which does not decompose at high temperatures. For experiment Foam1114, the residual solid fraction was about 0.01. The intersection of the two tangent lines to the measured solid fraction for Foam1114 determines the temperature corresponding to a SPUF solid fraction (0.04) that is used as the element death criterion. Using the onset of complete decomposition gives a consistent method to determine the element death criterion using the TGA data. Other methods for determining the death criterion can be used when significant liquefaction occurs. For example, the effective viscosity of the degrading foam may also be used as an element death criterion when liquid formation is significant.

The mean element death criterion and associated uncertainty was determined with the 20°C/min TGA experiments listed in Table 5.3. The intersection of the tangent lines near complete decomposition was obtained with TA Instrument's Universal Analysis 2000 software using the onset point analysis capability. Only the data taken at Sandia National Laboratories were used to determine the death criterion since the BYU data was not in a form compatible with the TA analysis software. The mean and standard deviation of the death criterion are 0.038 and 0.01, respectively.

Table 5.3. SPUF burnout based on TGA data*

Run	Sample	Burnout Onset point, C	CPUF burnout
1	F_062199	464.67	0.0442
2	Fm061499	480.86	0.0234
3	Foam1112	464.97	0.0438
4	Foam1114	465.18	0.0435
5	Foam1117	475.90	0.0285
6	Foam1118	472.26	0.0331
7	Foam1119	455.28	0.0619
9	Foam1204	466.07	0.0421
10	Foam1205	469.41	0.0372
11	fm102999	476.34	0.0280
12	fm103099	473.54	0.0314
13	fm110199	468.46	0.0386
14	fm11019a	469.70	0.0368
	Mean	469.43	0.0379
	Median	469.41	0.0372
	St. Dev	6.57	0.0098

*Run 8 (outlier), 15-18 (not in TA Analyzer format) not used

6. Discretization Bias Correction using Front Velocities

This section describes the steady-state decomposition front velocity in a 1D strand of foam using element death. A discretization bias correction model is used to correct the solution for discretization errors. The decomposition of a strand of foam is modeled as a column of elements with a radiation boundary condition at one end of the foam strand and an insulation (adiabatic) boundary condition on the remaining sides of the strand. The SPUF model was implemented into COYOTE and CALORE as an auxiliary-variable user subroutine. The thermophysical properties listed in Table 5.1 are implemented as material properties. In the FEM codes, the solid fraction, m/m_o, is determined at each Gauss point and the average solid fraction can be determined for each element. When the solid fraction within an element drops below a specified element death criterion, the element is removed from the computational domain and the surface boundary condition is applied to the newly exposed element — the exposed face of the foam strand exchanges energy via radiative heat transport to a far-field reference radiation temperature.

The steady-state decomposition front velocity is calculated as the derivative of the decomposition front location versus the elapsed time for element death. Figure 6.1 shows the calculated front location using various element sizes ranging from 1-mm elements to 50-μm elements. The foam strands used for the calculations in Figure 6.1 were exposed to a 1,000°C radiative temperature. The decomposition front location is taken as the centroid of the element associated with the radiation boundary. Elements are removed from the computational domain when the calculated solid fraction (m/m_o) drops below the mean element death criterion of 0.038.

The front velocities shown in Fig. 6.1 start at zero and then increase rapidly to a steady-state value. The velocity increases near the end of the strand of foam due to the adiabatic boundary condition enforced at the end of the strand of foam. The steady-state front velocities

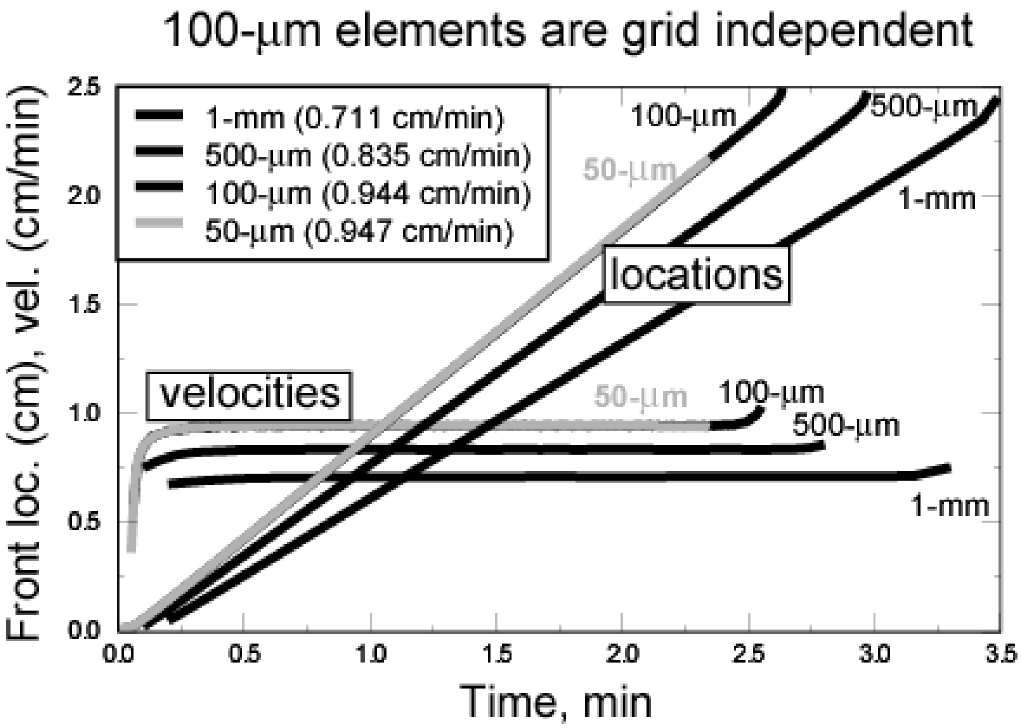

Fig. 6.1 Front location and velocity calculated using various element sizes ranging from 1-mm elements to 50-µm elements. The element size is indicated on the various curves.

plotted in Fig. 6.1 are also given in legend. As the size of the element decreases, a grid independent velocity was achieved. The velocity of the front became independent of the size of the element, or grid independent, when the size of the element was about 100-µm.

The steady-state decomposition front velocity is strongly dependent on the size of the element, especially if elements are larger than 100-µm. For elements that are 100-µm or less, the decomposition velocity is independent of the element size. Grid dependency is related to the discrete removal of elements and the inheritance of the radiation boundary condition on the newly exposed element. The application of the radiation boundary condition to newly exposed surfaces is a discrete rather than a continuous process. As the elements become smaller, the propagation of the front becomes more continuous.

Large elements contain more mass than small elements of the same density. Consequently, the lifetimes of larger elements are longer than the lifetimes of smaller elements with the same radiation boundary condition. Since element death is delayed when larger elements are used, the reapplication of the radiation boundary condition to the next element is also delayed, making the decomposition front move more slowly, since radiation to a surface is a more efficient means of heat transfer than conduction through an element. The size of the element has no effect on the front velocity when the element dimensions are 100-μm or less. Since 100-μm elements are impractical for realistic system-level calculations, a correction is needed to account for the bias associated with discretization.

In the CPUF model [5], the discretization bias correction was achieved by increasing the extrapolated thermal conductivity near the decomposition front depending on the element size and heat flux driving the reaction front. Measured thermal conductivities are not changed. However, the extrapolated thermal conductivity is used to obtain grid size independent decomposition front velocities. For example, Table 5.2 showed measured thermal conductivities up to 250°C. For the grid independent solutions with element sizes less than or equal to 100-μm, measured thermal conductivities are used when the temperature is 250°C or less. When temperature exceeds 250°C, thermal conductivities were linearly extrapolated between the measured conductivity at 250°C, $k_{250^\circ C}$, and the extrapolated conductivity at 3500°C, $k_{3500^\circ C}^{\text{linear extrapolation}}$, given previously in Table 5.2.

In practice, thermal conductivity is never extrapolated to 3500ºC. The maximum foam temperatures in the current report never exceed 1000ºC. With the exception of liquids such as water, liquid conductivities decrease with increasing temperature. However, at elevated temperatures expected in fire-like environments, effective conductivities may increase due to convective transport caused by bubble motion. Rather than speculate on mechanisms for extrapolating conductivity, a simple linear extrapolation was assumed herein.

For larger element dimensions (>100-μm), the extrapolated conductivity at 3500° C can be multiplied by a bias correction to match the decomposition front velocities calculated using 100-μm elements with the following equation:

$$k_{3500°\text{C}}^{\text{bias corrected}} = bias \times k_{3500°\text{C}}^{\text{linear extrapolation}} . \tag{16}$$

The bias correction factor, *bias*, in Eq. (16) was determined using the DAKOTA optimization toolkit [15] by minimizing the absolute RMS error associated with the difference between predicted front velocities using 100-μm elements and various larger element sizes over a wide range of far-field radiation boundary conditions:

$$\text{Absolute RMS error} = \sqrt{\left(V_{100\,\mu m} - V_{\text{Large Element}}\right)^2} . \tag{17}$$

The results of the bias optimization used for the CPUF model are given in Fig. 6.2.

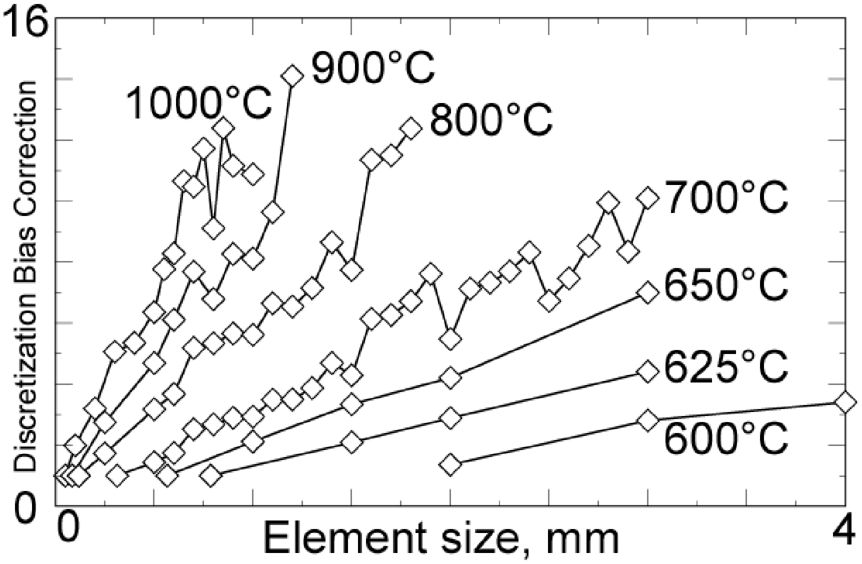

Fig. 6.2. CPUF [5] bias correction factors for various radiation boundary temperatures.

Figure 6.2 shows bias corrections for the CPUF model for element sizes up to 4-mm. Discretization bias corrections were only obtained for elements sizes up to 1-mm when the radiation boundary temperature was set to 1,000°C. If the applied heat flux is less than the heat flux produced by a 1000°C far-field radiation boundary condition, a *larger* bias-corrected element dimension can be used

Figure 6.3.A shows that the CPUF bias correction factor for 1-mm elements varies linearly with the radiation boundary condition. To apply the bias correction in Fig. 6.3.A to general boundary conditions, the temperature gradient within the individual elements was utilized. As

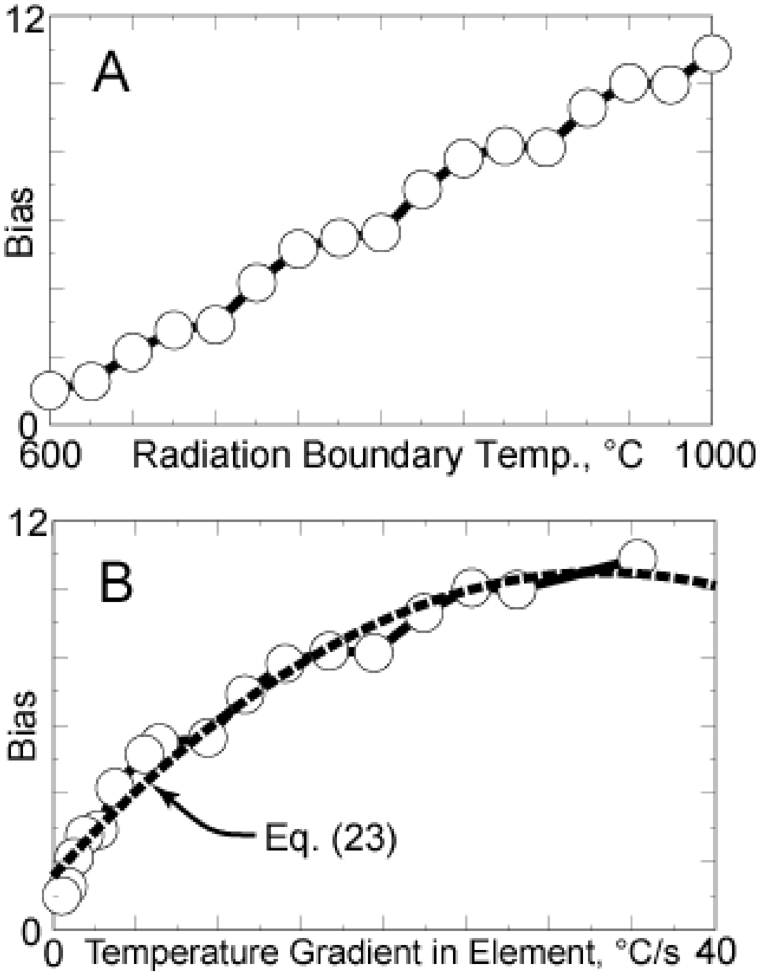

Fig. 6.3 CPUF discretization bias correction for 1-mm elements. Bias correction plotted as a function of A) radiation boundary temperature and B) temperature gradient in element when temperature exceeds 250ºC.

long as the temperature within individual elements is less than or equal to 250°C, then the measured thermal conductivity values were used. If the element exceeds 250°C, the temperature gradient within the elements was used to determine the bias correction. Figure 6.2.B shows that the bias correction factor for 1-mm elements varies quadratically with the temperature gradient determined once the element reaches a temperature of 250°C as follows:

$$bias = 1.57 + 0.538\left(\tfrac{dT}{dt}\right) - 0.00812\left(\tfrac{dT}{dt}\right)^2 \tag{18}$$

For extreme conditions, the bias correction factor is determined from the following equation:

$$bias = \begin{cases} 10.48 & \tfrac{dT}{dt} \geq 33.1 \\ 1 & \tfrac{dT}{dt} \leq 1.55 \end{cases} \tag{19}$$

where 10.48 is the maximum bias correction and 1 signifies no bias correction.

Figure 6.4 shows a test problem run with CPUF using both 50-μm elements and 1-mm elements showing the validity of the bias correction model. Hobbs et al. [5] give more detail regarding Fig. 6.4. The bias correction for the CPUF model given in Eq. (18) was developed for exclusive use with elements having characteristic dimensions of 0.1-mm. However, Fig. 6.2 clearly shows that a similar discretization model may be possible for various element dimensions. Thus, a generalized discretization bias correction model was sought for the SPUF model for use with element sizes ranging from 1-mm to 1-cm.

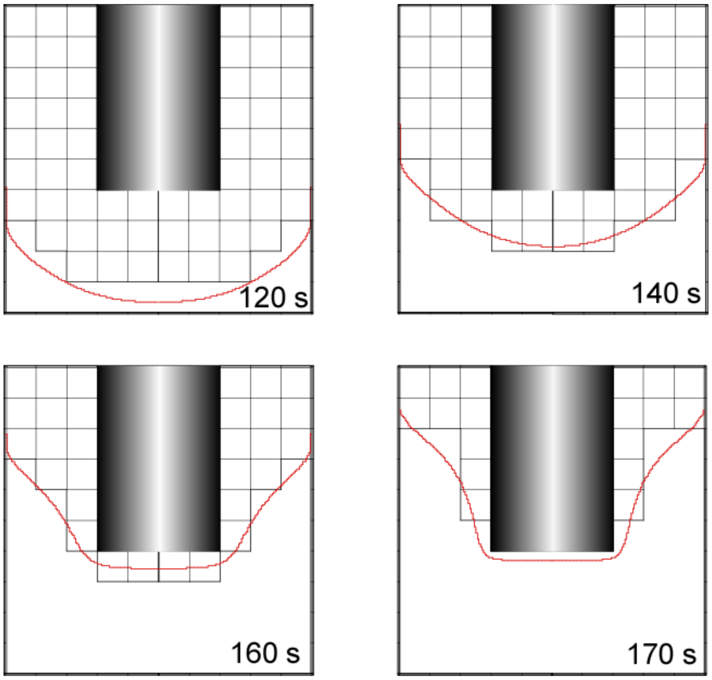

Fig. 6.4. Decomposition around an encapsulated component at various times using 1-mm elements and 50-μm elements. The 1-mm elements are shown as small squares. For the 50-μm element solution, the decomposition front is shown as a solid line.

The general form of the discretization model for the SREF model is the same as the discretization model for the CPUF model given in Eq. (16). However, the empirical model for the bias factor is different. The bias factor used for the CPUF model was given in Eq. (18) as a function of only the heating rate. Equation (18) contains the implicit requirement that the characteristic element dimension be 1-mm. Rather than limit the SPUF model to 1-mm element sizes, a more general empirical bias factor was determined using mesh independent velocities calculated with strands of 100-μm elements exposed to far-field boundary conditions with radiation temperatures ranging from 600ºC to 1000ºC.

A discretization bias correction surface (plotted in Fig. 6.5) was generated using the SPUF model by obtaining the bias factor for various steady-state decomposition front velocities calculated with 17 radiation temperatures ranging from 600ºC to 1000ºC at 19 grid sizes ranging

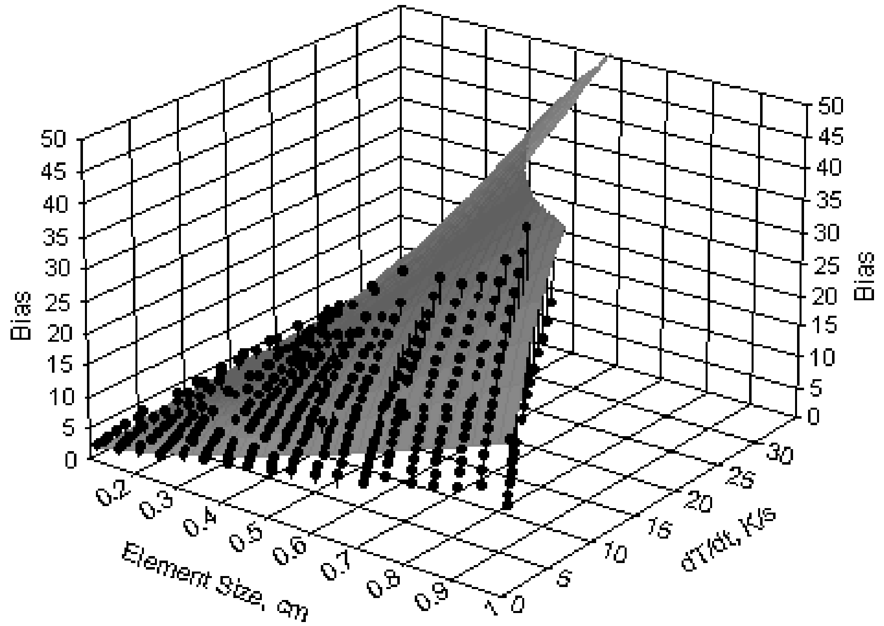

Fig. 6.5. SPUF bias factor for 1-mm to 1-cm elements. Bias factors are plotted as a function of temperature gradient in element when temperature exceeds 250ºC and element size.

from 1-mm to 1-cm. The bias factor was determined by minimizing the absolute RMS error associated with the difference between predicted front velocities using 100-μm elements and larger element. A total of 323 minimizations (17 temperatures × 19 grid sizes) were performed using the DAKOTA toolkit [15]. Figure 6.5 shows the 323 bias values plotted as spheres and the best-fit surface.

The equation for the surface shown in Fig. 6.5 is

$$\ln\left(bias_{SPUF}\right) = 3.09 + 0.441\ln\left(\frac{dT}{dt}\right) + 1.35\ln\left(y\right), \tag{20}$$

where *dT/dt* (K/s) is the temperature gradient and y (cm) is the characteristic dimension based on the node coordinates. A similar equation was found when the characteristic dimension is based on the Gauss point coordinates:

$$\ln\left(bias_{SPUF}\right) = 3.59 + 0.437\ln\left(\frac{dT}{dt}\right) + 1.20\ln\left(y\right). \tag{21}$$

The characteristic dimension, *y*, in Eqs. (20) and (21) can be calculated several ways. The most computationally expensive method of calculating the characteristic dimension is to take the cubed root of the volume of the three dimensional elements and taking the square root of the area for two-dimensional elements. A more efficient method of calculating the characteristic dimension is to take the average length of the sides of a parallel-piped that encompasses the element. The next section discusses each of these options.

The bias corrections in Eq. (20) and (21) were obtained using characteristic dimensions based on either the coordinates of the element nodes or the coordinates of the Gauss points within the elements. Either equation gives essentially the same correction. The correction should only be applied when the surface temperatures are between 600 and 1000ºC, which is the range of temperatures used to obtain the correlation. This range is sufficient for abnormal thermal environments where a system may be exposed to fire-like heat fluxes. As the flux approaches zero, no correction is needed since the foam will not propagate a decomposition front. As the characteristic element dimension approaches zero, the bias correction should approach unity. Extrapolation of the bias correction to values less than 1-mm is not recommended since the surface was determined with elements ranging in size from 1-mm to 1-cm.

7 Verification of the SPUF Discretization Bias Correction Model

The bias correction surface shown in Fig. 6.4 was tested with a variety of meshes, shown in Table 7.1, using element dimensions ranging from 0.1-cm to 10-cm. Bias corrected velocities were compared to the grid independent steady-state velocities. One end of the one-dimensional foam strand was exposed to a far field radiation boundary condition with the radiation tempera-

Table 7.1 Various mesh types used to verify the discretization bias correction model

Mesh	Lateral View	End
A **2D Axisymmetric QUAD**	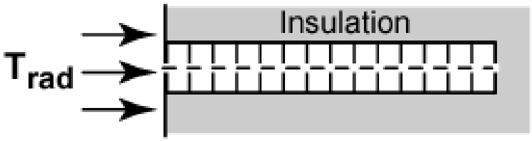	
B **2D square QUAD**	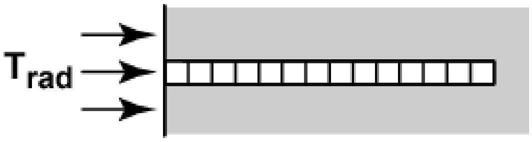	
C **3D cube HEX**	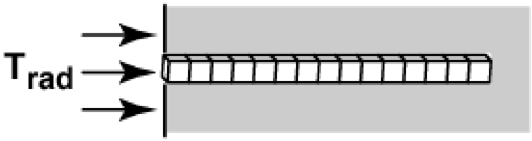	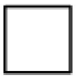
D **3D regular TET** **(nodes from type C mesh)**	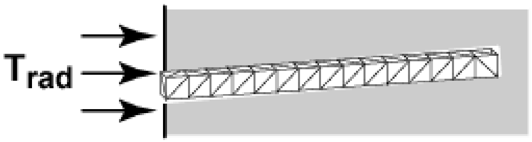	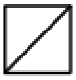
E **3D paved HEX**	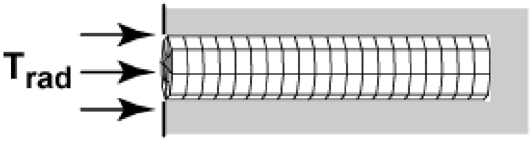	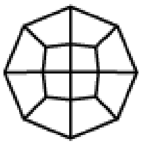
F **3D irregular TET**	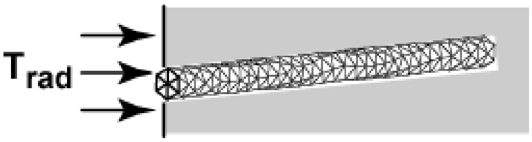	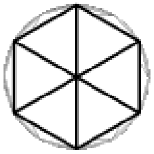

ture ranging from 600°C to 1000°C. The other sides were insulated. The decomposition of a strand could be performed with a one-dimensional model; however, for the simulations in this report, two and three-dimensional meshes were used to determine the steady-state velocity using either COYOTE or CALORE since the end use of the foam decomposition model is inherently multi-dimensional.

Twelve different types of runs listed in Table 7.2 were used to evaluate the discretization bias correction model using different types and sizes of elements. The twelve plots referenced A-L in Table 7.2 are shown in Fig. 7.1. The bias surface was first evaluated by determining the effect of the characteristic element dimension calculated by either using the Gauss points [Fig. 7.1.A with bias surface evaluated with Eq. (21)] or the Node points [Fig. 7.1.B with bias surface evaluated with Eq. (20)]. Results using either Eq. (21) or (20) are within 1% or better when compared to the grid-independent velocities over the entire range of temperature boundary conditions leading to the conclusion that the bias correction can be performed with either the Gauss coordinates or the node coordinates.

The effect of element size is also shown in Fig. 7.1.A and 7.1.B. Fig. 7.1.C and 7.1.D also show the effect of various element sizes for meshes constructed from 2D square quadrilateral (QUAD) and 3D regular hexahedral (HEX) elements. Although dimensions were investigated

Table 7.2 One dimensional SPUF runs used to verify discretization bias correction model

Plot	Mesh Type	Effect	Approximate dimensions
A	A: 2Daxi QUAD	Dimension from Node Points	0.1 to 1-cm
B	A: 2Daxi QUAD	Dimension from Gauss Points	0.1 to 1-cm
C	B: 2D QUAD	2D Element Size	0.1 to 1-cm
D	C: 3D reg HEX	3D Element Size	0.1 to 1-cm
E	D: 3D reg TET	Element Type/45° orientations	1-cm
F	E: 3D paved HEX	Paving	0.5-cm
G	F: 3D twisted TET	Element Type/Random Orientations	1-cm
H	B: 2D QUAD	Aspect Ratio (1:1 to 10:1)	0.1 to 1-cm
I	B: 2D QUAD	Aspect Ratio (1:1 to 1:10)	0.1 to 1-cm
J	A: 2Daxi QUAD	Extrapolated Size	1 to 10-cm
K	C: 3D reg HEX	Characteristic Dimension Calculation	1-cm
L	B: 2D QUAD	Element Death Criterion	1-cm

from 0.1-cm to 1-cm, only select dimensions were used for the plots in Fig. 7.1 for clarification. All of the simulations in this section with various sizes and types of elements give essentially the same velocity as the grid-independent velocity calculated using 100-μm elements and shown as symbols in Fig. 8.1.

The bias surface was next evaluated with various types and element orientations. For instance, the 3-D row of 1-cm^3 HEX elements was sliced to create a row of TET elements (see mesh type C and D in Table 8.1). The 15 elements in mesh type C were split into 90 tetrahedral elements by using the same node locations as the 15 stacked bricks. In other words, the HEX mesh was used to construct the TET mesh by slicing each of the 1-cm by 1-cm by 1-cm elements into 6 TET elements. Figure 7.1.E shows a comparison between the regular HEX mesh and the diced TET mesh. Both of the 3D mesh types give the same mesh independent velocities as solutions using 100-μm elements.

Next, the effect of the bias surface was evaluated for 3-dimensional paved meshes (see mesh type E in Fig. 7.1). The cross-sectional view of this mesh in labeled “End” in Fig. 7.1. The diameter of the strand was 2-cm and the length of the strand was 10-cm, making the approximate dimension of the irregular hexahedral elements 0.5-cm by 0.5-cm by 0.5-cm. Figure 7.1.F shows a comparison between the regular HEX mesh and the diced TET mesh. The solution using the 3D paved mesh gives the same velocities as solutions using 100-μm elements.

The most demanding test of the bias surface was performed using an extremely irregular, twisted TET mesh (see mesh type F in Fig. 7.1). One of the problems encountered with using the irregular TET mesh was evaluating the front velocity with seemingly random element edges and node locations. At best, the front locations were probably good to about 1-cm and the velocity calculations are somewhat suspect. Nevertheless, the calculated velocities with the irregular TET mesh are within 15% or better when compared to the grid independent solutions. A better evaluation of irregular TET elements is discussed towards the end of the report, where both random, 2D-axisymetric triangular (TRI) elements and 3D TET elements are used to simulate the radiant heat experiments. For these simulations, the randomly place TRI and TET elements can be used to adequately capture the grid independent velocities.

The effect of aspect ratio was also investigated. In Fig. 7.1.H, the dimension of the heated edge is 1-cm and the edge parallel to the heat flux is changed from 1-cm to 0.1-cm causing the aspect ratio to vary from 1 to 10. In essence, the 2D QUAD element is changed from a square element to a short squatty element. The effect of aspect ratio is minor even for aspect ratios as high as 10 provided the heat flux is applied perpendicular to the larger element face. The results are not as good if the heat flux is applied to the smaller element face as shown in Fig. 7.1.I. In Fig. 7.1.I, the dimension of the heated edge parallel to the heat flux is kept at 1-cm and the heated edge is changed from 1-cm to 0.1-cm causing the aspect ratio to also vary from 1 to 10. The difference between Fig. 7.1.H and Fig. 7.1.I is in the direction of the applied heat flux. If the flux is applied to the smaller face, the agreement is acceptable up to an aspect ratio of 5.

The final three plots in Fig. 7.1 show the effect of extrapolated element size, the element death criterion, and simplification of the characteristic dimension calculation. Figure 7.1.J shows that the extrapolated bias surface for element sizes ranging from 1-cm to 10-cm is surprisingly good. Large elements may be important for certain simulations where the foam fills large systems.

Figure 7.1.K shows the effect of simplification of the characteristic dimension calculation. The characteristic dimension of an element [*y*-value in Eq.(20) and (21)] can be calculated several ways. All of the examples thus far used the method of taking the square root of 2-D element areas, and the cubed root of 3-D element volumes to calculate this value. Another method takes the average length of the sides of a parallel-piped that encompasses the element. This is equiva-

lent to averaging the maximum ∆x, ∆y, and ∆z values for the element. This method was evaluated (see Fig. 7.1.K) and found to be more computationally efficient, yet equally accurate.

Figure 7.1.L shows the effect of the element death criterion. Figure 7.1.L shows that the same discretization bias correction surface plotted in Fig. 6.4 can be used if the death criterion is changed from 0.038 to 0. 4. Notice that a new grid-independent velocity was determined for the plot in Fig. 7.1.L. With a 1000°C free-field radiation boundary temperature, the steady-state front velocity increased form 0.94-cm/min to 1.45-cm/min by changing the death criterion from 0.038 to 0.40. The element death criterion is a sensitive model parameter that may be used to prevent liquid build-up at the decomposition front to approximate liquefaction and flow effects that cannot be accommodated in a simple heat flow model.

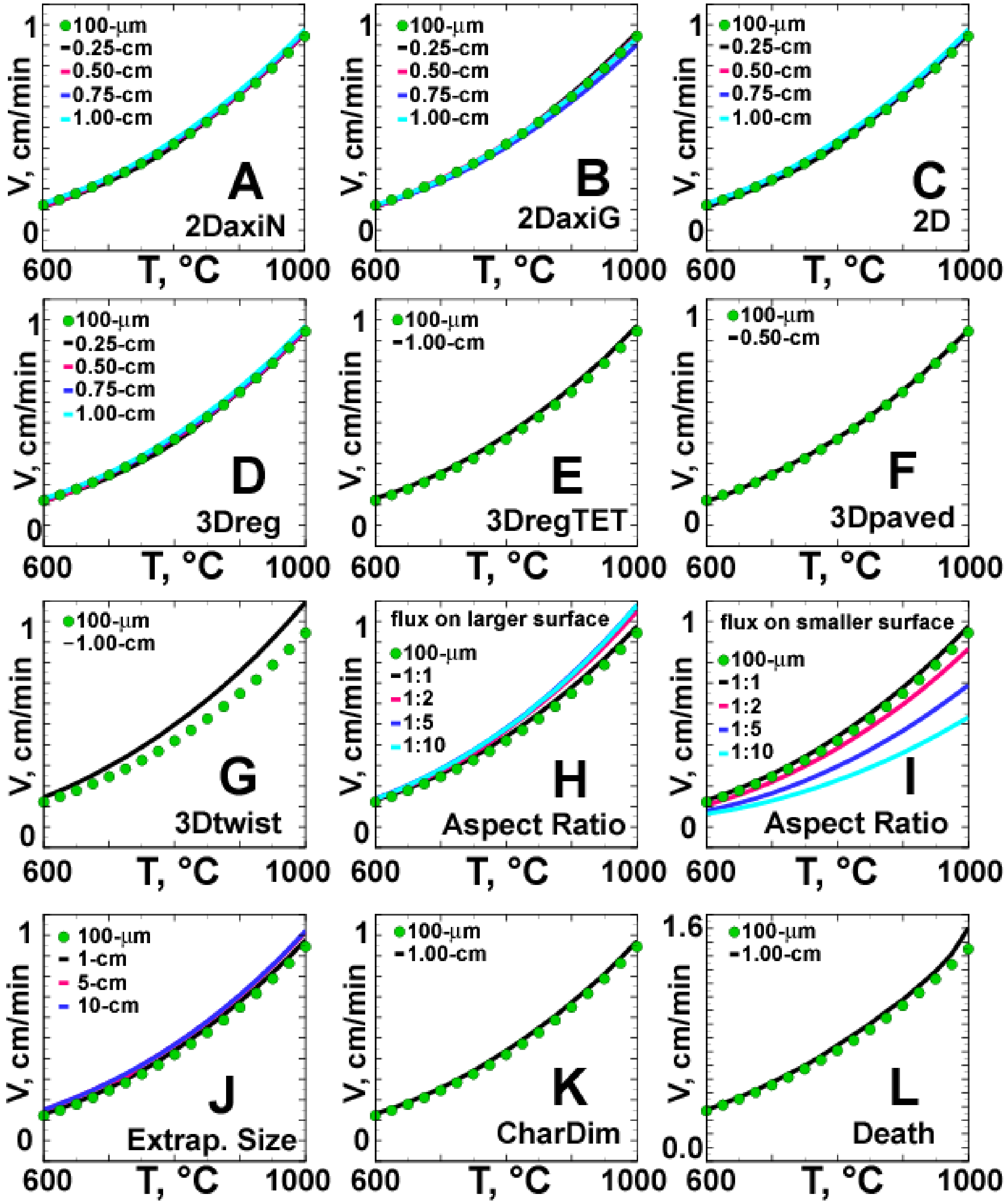

Fig. 7.1. Grid independent velocities (symbols) compared to various bias corrected velocities. Descriptions of the different plots in A through L are found in Table 7.1 and 7.2.

8 Radiant Heat Experiments

The radiant heat experiments provide a method to test the SPUF model for larger-scale systems of interest, where spatially resolved temperatures are important. The radiant heat experiment; including geometry, test matrix, thermal and pressure boundary conditions; are presented in this section. Specific data on the thermal boundary conditions for each of the radiant heat experiments are included in the CPUF documentation [5]. Section 9 compares the seven different SPUF simulations for each of the radiant heat experiments using a variety of element types – nominally 1) 0.25-cm regular quadrilateral (QUAD) elements, 2) 0.50-cm regular QUAD elements, 3) 1.00-cm regular QUAD elements, 4) paved QUAD elements, 5) 0.50-cm triangular (TRI) elements, 6) 1.00-cm triangular (TRI) elements, and 7) 1.00-cm tetrahedral (TET) elements.

8.1 Configuration

Pictures and schematics of the component-scale radiant heat experiments are shown in Figure 8.1, where the foam is shown as an 8.8-cm diameter, 14.6-cm high right circular cylinder. The foam was contained in a sample cup with a 6-mm stainless steel plate that was force-fit into a 7.3 to 16.4-cm long, thin wall (0.5-mm) stainless steel tube. Various orientations of the experiment are shown in Fig. 8.2. The 6-mm stainless steel plate was welded to the thin walled stainless steel tube. Both sides of the stainless steel plate and the inside of the stainless steel tube were painted with flat black Pyromark® 2500. Up to six 6-mm holes were drilled through the side of the stainless steel tube, near the cup plate, to vent decomposition gases into a flame guard. A flame guard was used to prevent fuel rich gases from oxidizing near the cup walls.

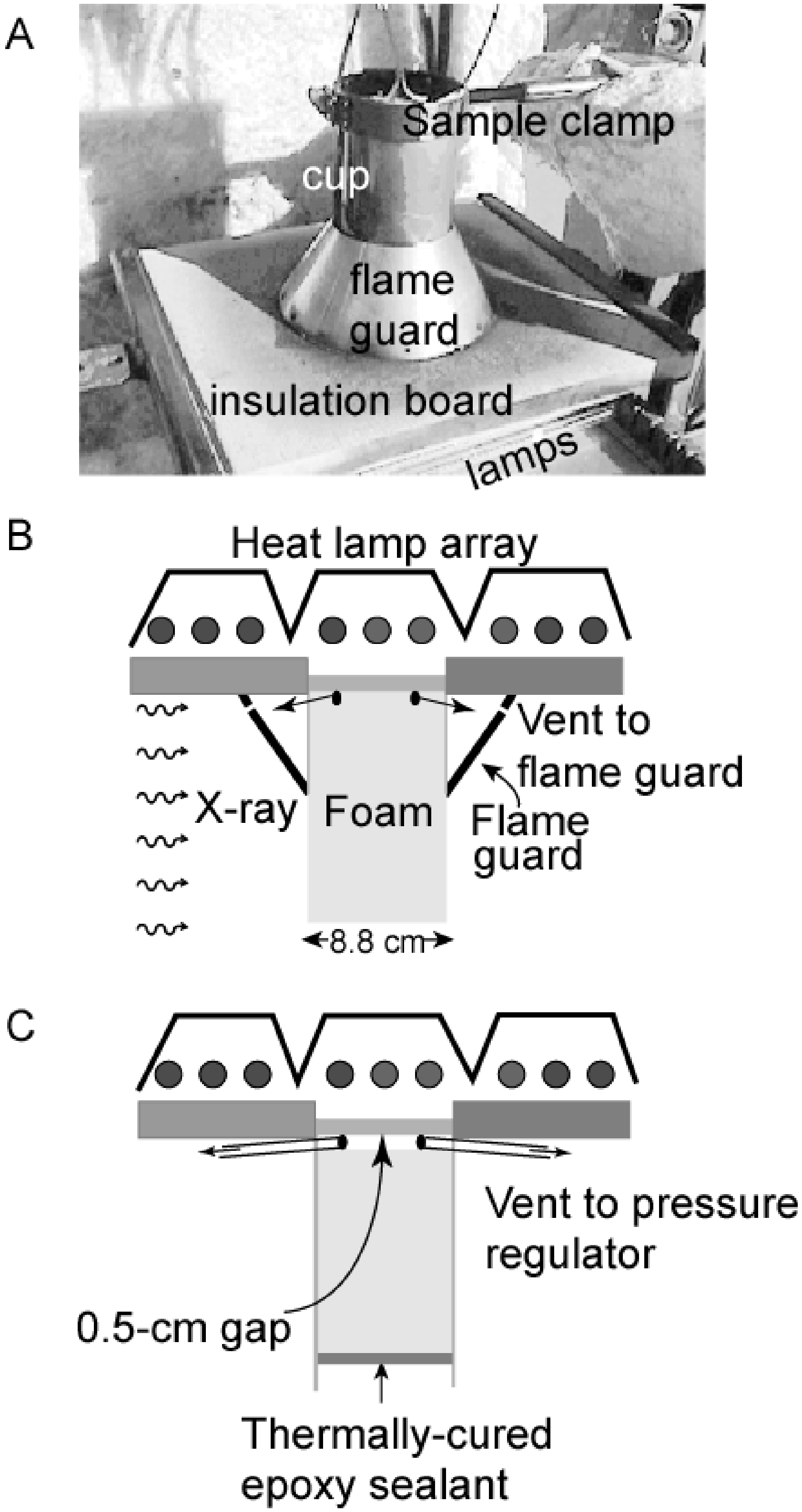

Fig. 8.1 A) Photograph of bottom heated radiant heat experiment, B) schematic of top heated unconfined radiant heat experiment, and C) schematic of partially confined top heated radiant heat experiment.

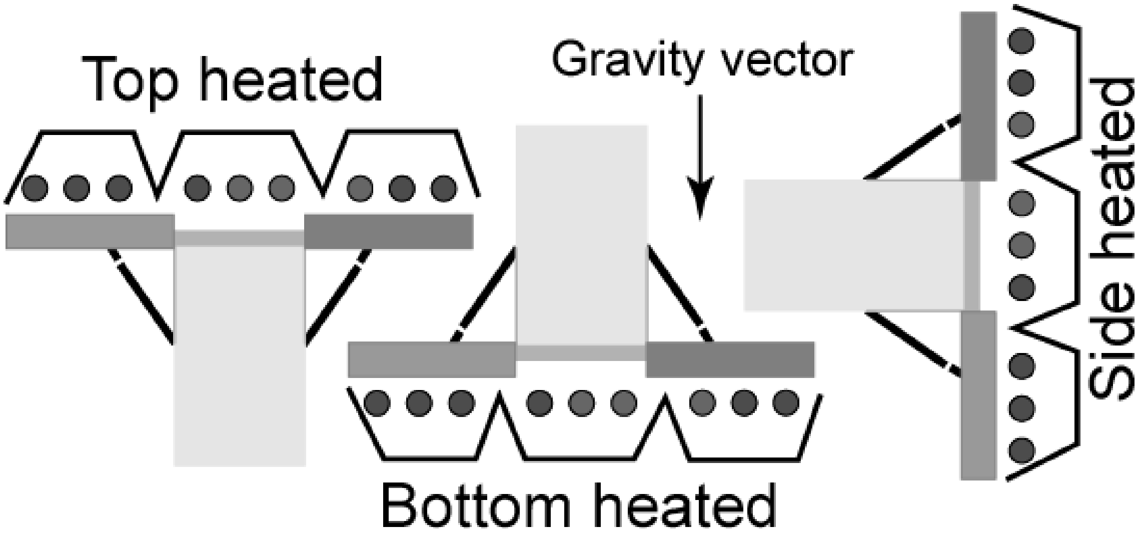

Figure 8.2 Three orientations for the radiant heat experiments.

Figure 8.1.C shows the partially confined component-scale radiant heat apparatus without the flame guard. The configuration for the partial confined radiant heat experiments are similar to the unconfined radiant heat experiments except that the outer cup was sealed at the top using a thermally cured epoxy sealant and the gases were vented to a pressure regulator. Four 5-mm ID stainless steel vent tubes (smaller vent area than the unconfined tests) were used for the partially confined experiments. The tubes were connected to a water-cooled (~5°C) condenser initially charged with nitrogen and regulated with a pressure control valve to the desired test pressures of 0.0, 0.1, and 0.3-MPa (0, 15, and 40-psig). In the partially confined experiments, the face of the foam cylinder was not flush with the heated plate. Rather, a 0.5-cm gap was left between the initial surface of the foam and the heated plate to prevent decomposition gases from clogging the vent holes. The gap was modeled as a radiation enclosure with the finite element model.

The cup was heated by an array of high intensity infrared radiant heat lamps as shown in Fig. 8.1. The relatively thick plate promotes uniform heating of the foam samples. The uninsulated thin stainless steel sidewall limits lateral conduction. As shown in Fig. 8.2, the experiments were performed with the heated surface facing upward (top heated), downward (bottom heated), or sideward (perpendicular to the gravity vector). The experiments were fully instrumented with thermocouples, heat flux gauges, and an X-ray camera described previously [14].

Some of the experiments contained a simulated internal component that was positioned 2.1-cm from the heated foam surface. The internal component was 3.81-cm in diameter and 6.35-cm long. All surfaces were plated with black copper. Simulated embedded components were manufactured from 304 stainless steel or 6061-T6 aluminum. The stainless steel component was a solid cylinder, but the aluminum component was machined in the shape of a cup. The aluminum component was positioned within the foam cylinder so the solid end of the aluminum cup was close to the heated end of the foam. A 0.315-cm diameter stainless steel threaded rod prevented the component from shifting after the foam became soft due to thermal degradation. A foam plug was placed in the cavity after the component was in position.

A description of 19 large-scale experiments organized to emphasize various effects is given in Table 8.1. The quasi-steady incident heat flux, required to maintain the cup plate at various temperatures, is also given in Table 8.1 along with various notes regarding some of the experiments. The heat fluxes given in Table 8.1 are only approximate with more detail given in the next section. The temperature boundary conditions for each of the experiments are also given in the next section. The effects studied include the quasi-steady bottom plate temperature for both low-density and high-density foams, the orientation of the experiment with respect to the gravity vector, the presence of either a hollow aluminum component or a solid stainless steel component for both high- and low-density foam, and confinement with backpressures ranging from ambient conditions to 3.58-atm.

Table 8.1 Component-scale radiant heat experiments

Effect	Identifier[a]	*Description*[b]	Flux[c]	T_{plate}[d]	Notes
Bottom plate temperature (high-density)	600-1	600-H.bot.no.u.0	6	h	
	750-2[e]	750.H.bot.no.u.0	11	h	Sampling (3.5 and 28-min)
	900-3	900.H.bot.no.u.0	19	c	Control oscillations
	900-14	900.H.bot.no.u.0	21	h	Test 900-3 repeat
Bottom plate temperature (low-density)	ld600-6	600.L.bot.no.u.0	6	c	
	ld750-12	750.L.side.no.u.0	12	h	
	ld900-7	900.L.bot.no.u.0	22	c	Flame around base
Orientation	side-11	750.H.side.no.u.0	9	h	Shield obscured sample
	side-13	750.H.side.no.u.0	9	c	Test side-11 repeat
	top-10	750.H.top.no.u.0	12	h	
Component (high-density)	al-4	750.H.bot.al.u.0	12	c	Late vent, al movement
	al-15	750.H.bot.al.u.0	14	h	Test ss-15 repeat
	ss-1000-19	1000.H.side.ss.u.0	31	c	
	ss-5	750.H.bot.ss.u.0	12	h	
Component (low-density)	ldal-8	750.L.bot.al.u.0	11	h	
	ldss-9	750.L.bot.al.u.0	12	h	
Confinement	600-amb-p4	600.H.top.no.p.0	6	c	Cup thermocouple failed
	600-1.54-p2	600.H.top.no.p.1.	4	c	
	600-3.58-p3	600.H.top.no.p.3.	7	h	

[a] Identifiers give a brief description of the experiment followed by the run identification number. A more detailed explanation of the run is given in the description.

[b] Experiments described by six effects separated by periods. Effects refer to flux (cup plate temperatures of 600, 750, 900, or 1000°C), density (high, H, 0.364 g/cc; or low, L, 0.091 g/cc), orientation of heated surface (bot, top, side), embedded component (none, no; solid stainless steel, ss; or hollow aluminum, al), confinement (unconfined, u, partially confined, p), and gauge pressure (0: 0.0-MPa, 1: 0.07-MPa, 3: 0.28-MPa).

[c] Quasi-steady incident flux (W/cm^2) measured after the plate reached a steady temperature.

[d] The heated plate had two thermocouples designated as either the “h” or “c” thermocouple. The “h” thermocouple read a slightly higher temperature than the “c” thermocouple. The “h” or “c” in this table refers to the thermocouple used as the plate boundary condition in the CPUF simulation.

[e] Experiment 750-2 is the base case.

8.2 Thermal Boundary Conditions

A heat flux gauge was mounted 6.35-cm from the centerline of the heated plate to the centerline of the gauge. The heat flux gauge was 2.22-cm closer to the lamps than the heated plate and is not an exact measurement of the incident heat flux on the heated plate. The heat flux measured for the 19 experiments listed in Table 8.1 are plotted in Fig. 8.3. The flux levels required to maintain the heated plate for the high-density experiments were similar to the flux

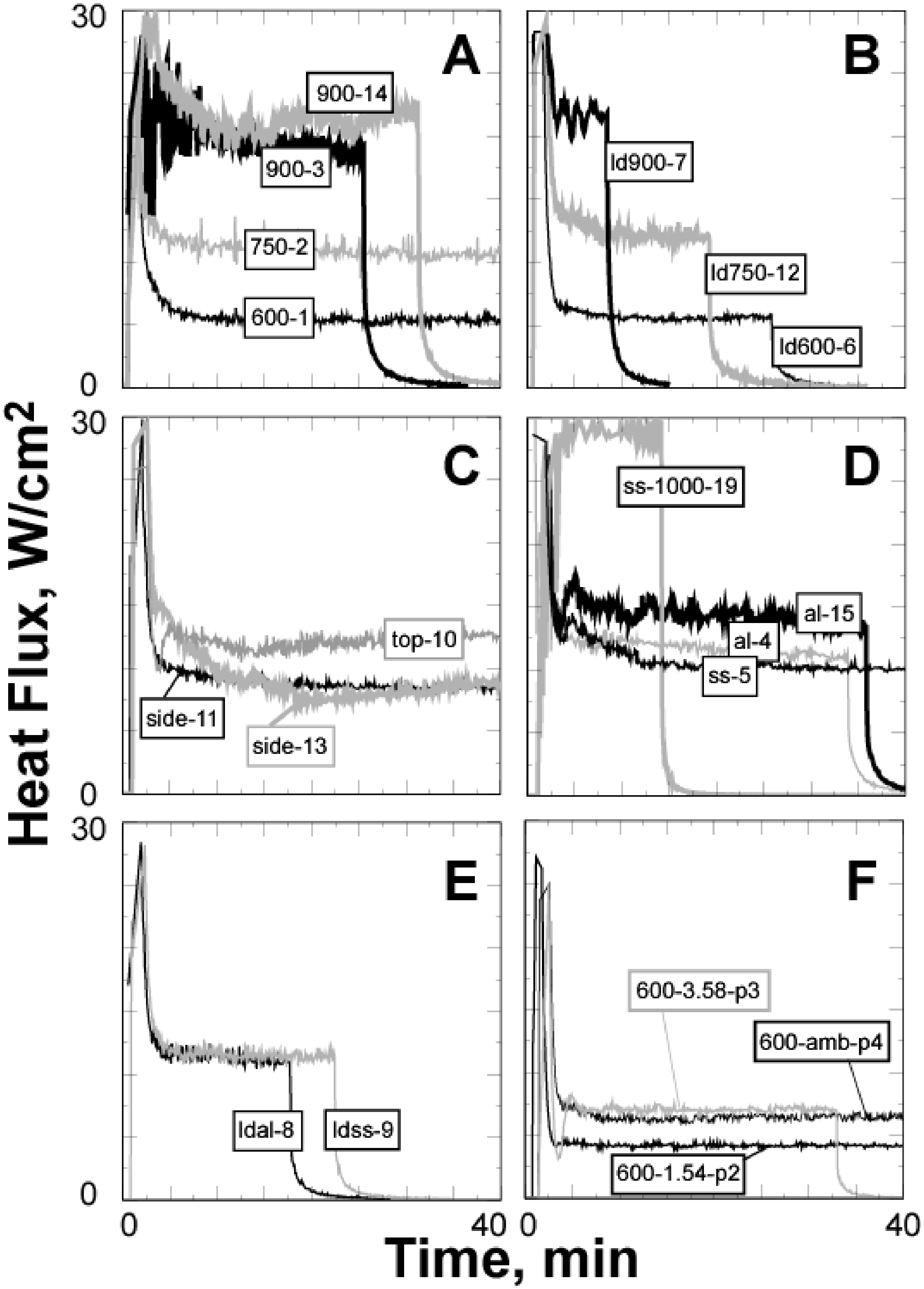

Fig. 8.3. Measured heat flux for the radiant heat experiments grouped by A) bottom plate temperature for high-density foam, B) bottom plate temperature for low-density foam, C) orientation, D) component embedded in high-density foam, E) component embedded in low-density foam, and F) confinement.

levels required to maintain the heated plate of the low-density experiments at the same temperature. Some erratic behavior is apparent in the recorded heat fluxes shown in Fig. 8.3. For example, side-11 reached a steady heat flux level whereas the flux recorded for the duplicate experiment side-13 was noisier.

The heat flux required to maintain the bottom plate temperatures at 750°C was also dependent of the orientation of the experiment as shown in Fig. 8.3.C. For example, the top heated experiment required a larger heat flux than the side heated experiments to maintain the heated plate temperature at 750°C. X-rays of the partially confined foam experiments in Fig. 8.3.F revealed liquid formation. For these experiments, the heat flux required to maintain the heated plate at 600°C was significantly different for these experiments exhibiting liquefaction effects.

A schematic of the confinement can for the radiant heat experiment is shown in Fig. 8.4. Thermocouples located within the heated plate are labeled “c” and “h” in Fig. 8.4. The “c” represents the cooler thermocouple because the “c” thermocouple is slightly farther away from the radiant heat source than the hotter thermocouple marked with an “h” in Fig. 8.4. The temperature of the bottom plate should be nearly uniform after the initial transient heating of the plate. The thermocouples labeled 1 through 5 on the outside of the confining can were also used as temperature boundary conditions for the SPUF simulations. Thermocouples were used for the boundary conditions since the radiation and convective coefficients on the side of the can were not measured.

Figure 8.5 shows more detail of the bottom plate. Because of the close proximity of the “c” and “h” thermocouples, the temperature for these two thermocouples should be close. The bottom plate temperature was controlled in the SPUF model by either the “c” thermocouple or the “h” thermocouple. Table 8.1 indicates which thermocouple the SPUF model used for the bottom

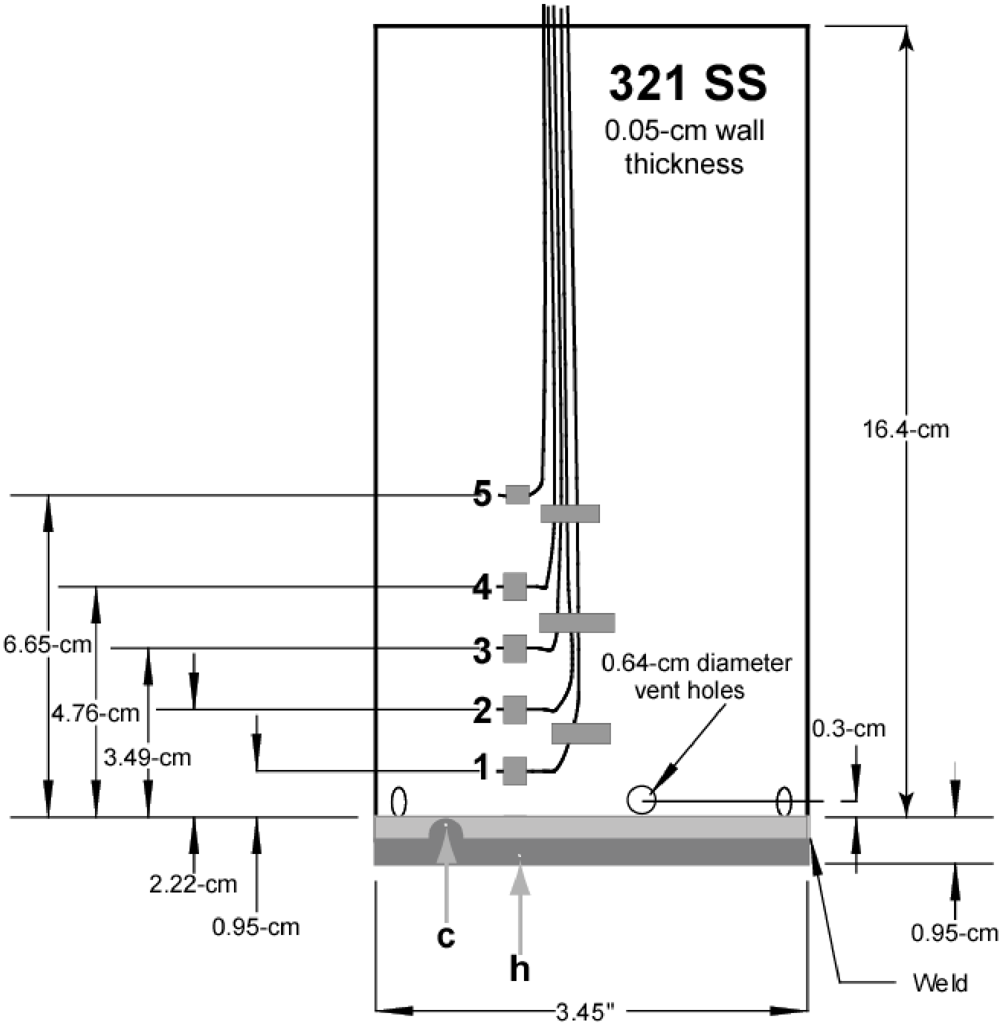

Fig. 8.4 Schematic of the confinement can for the radiant heat experiments.

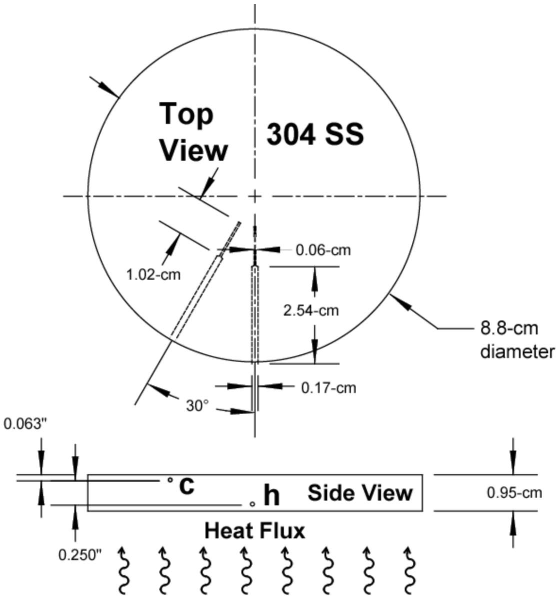

Fig. 8.5 Schematic of the heated plate.

plate temperature. The “c” thermocouple would have given the best estimate of the plate temperature since the “c” thermocouple is located closer to the foam surface. The location of the applied temperature boundary condition was always specified in the SPUF model at the location of the “c” thermocouple shown in Fig. 8.5. However, the original data set had the “c” and “h” thermocouple data mislabeled in some of the data files. Thus, 11 of the 19 SPUF simulations were run with the “c” thermocouple data for the bottom plate temperature and 8 of the 19 simulations were run with the “h” thermocouple data for the bottom plate temperature. This error in the bottom plate thermocouple resulted in temperature differences ranging from 2 to 18 degrees. The uncertainty in the boundary condition is greater for the higher temperature boundary conditions due to higher temperature gradients within the heated plate.

Figure 8.6 through 8.9 show plots of the temperatures recorded for each of the 19 experiments listed in Table 8.1. The numbers and letters on the temperature profiles correspond to the thermocouples shown in Fig. 8.4 and 8.5, respectively. Temperatures used for boundary conditions in the radiant heat experiments are given the CPUF reference [5]. Figure 9.6, 9.7, 9.8, and 9.9 give the temperature boundary conditions for the experiments with the control thermocouple set to 600°C for the high/low-density foam, 600°C for the partially confined experiments, 750°C for the high/low-density foams with/without embedded components, and 900°C for the high- and low-density foams, respectively. The experiment with the stainless steel component and a bottom plate set temperature of 1,000°C is also shown in Fig. 8.9.

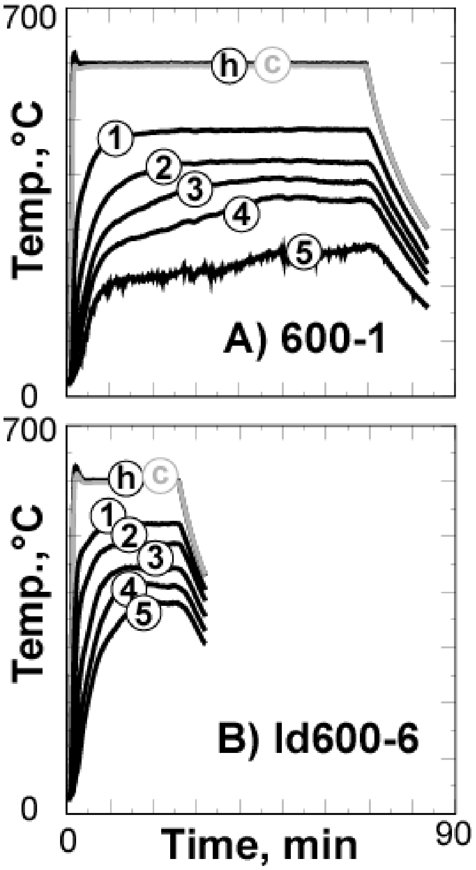

Fig. 8.6 Temperature boundary conditions for experiments A) 600-1 and B) ld600-6.

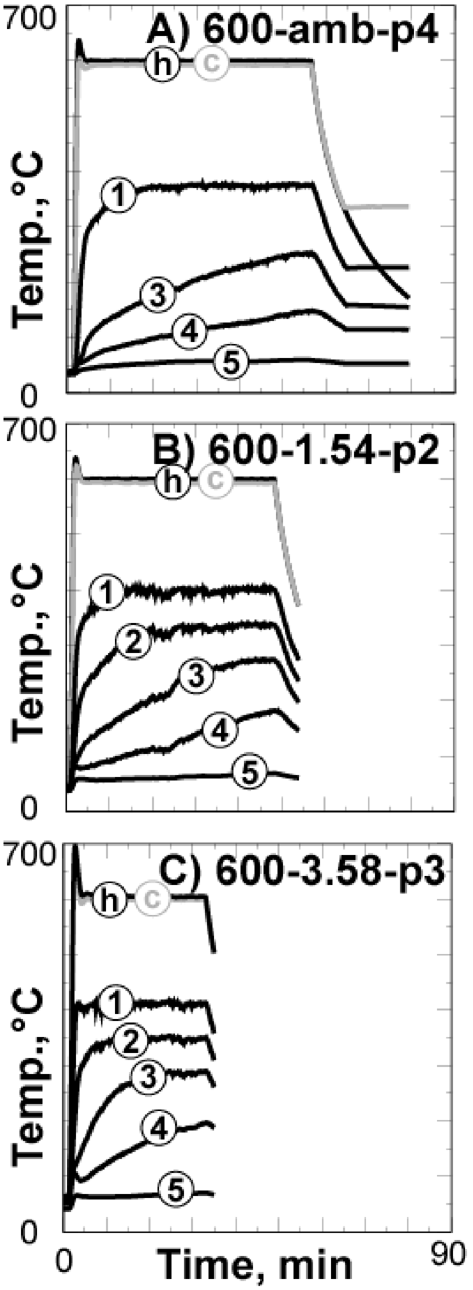

Fig. 8.7 Temperature boundary conditions for partially confined RPU experiments A) 600-amb-p4, B) 600-1.54-p2, and C) 600-3.58-p3.

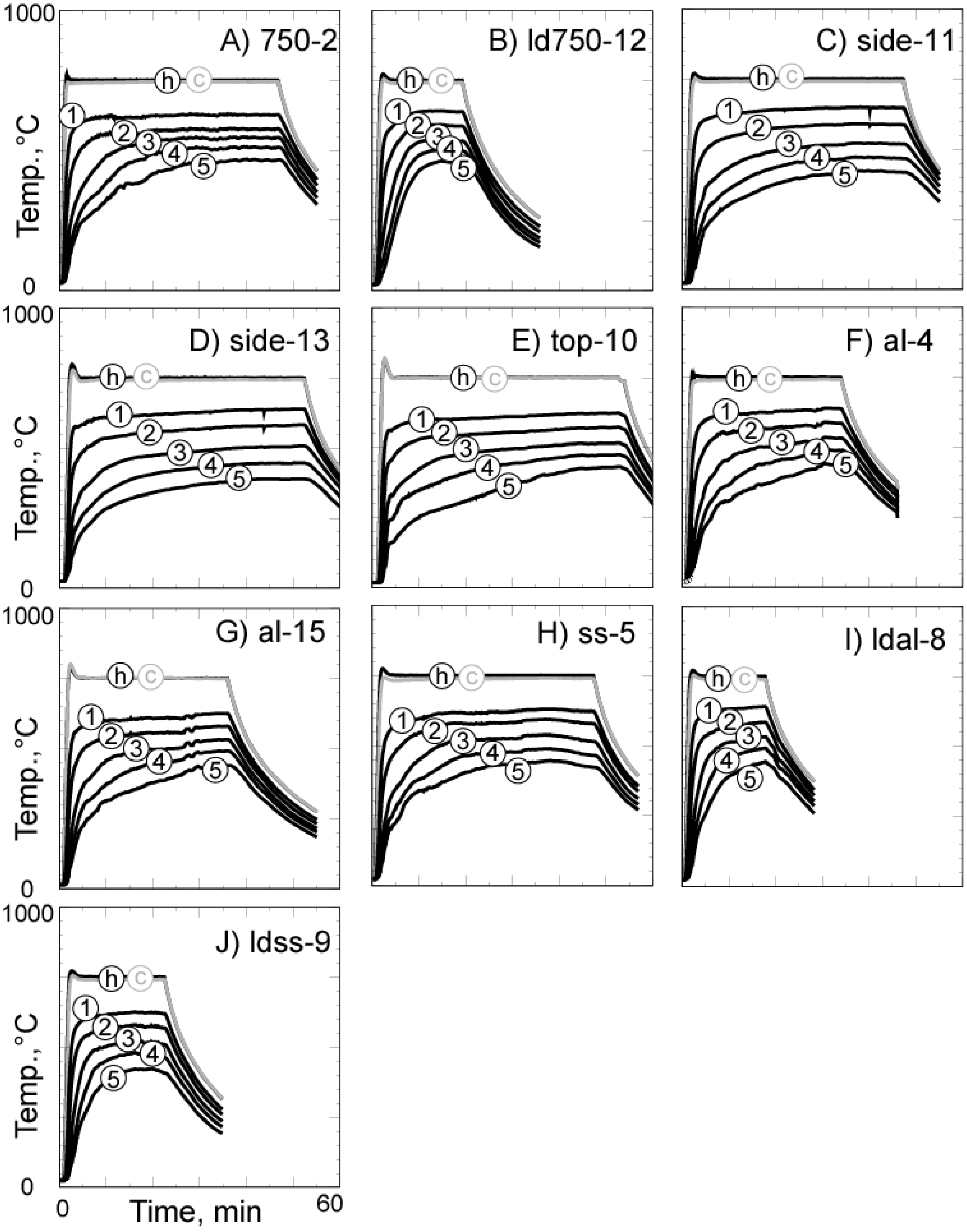

Fig. 8.8. Temperature boundary conditions for the 750°C radiant heat experiments.

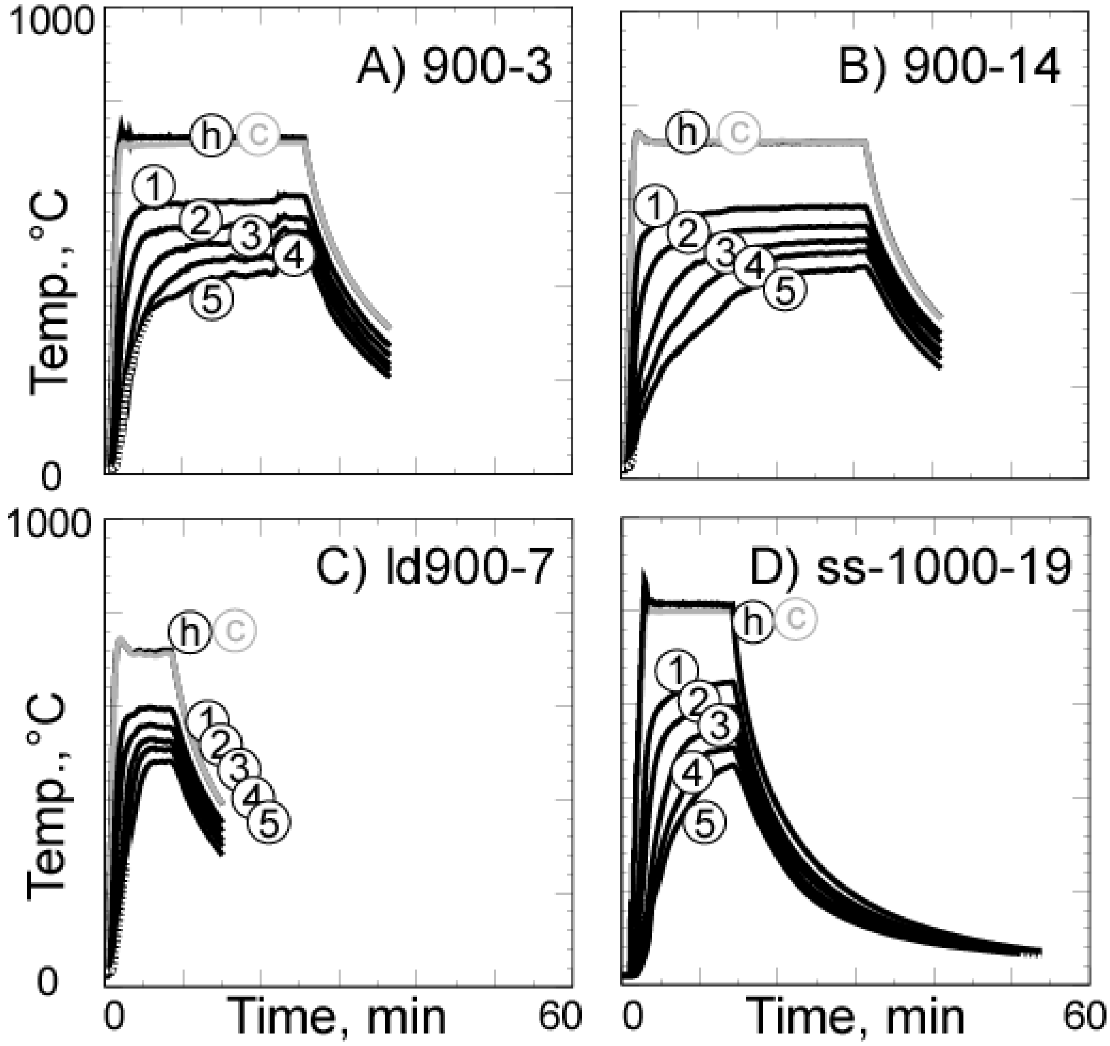

Fig. 8.9 Temperature boundary conditions for the 900ºC and 1000ºC radiant heat experiments.

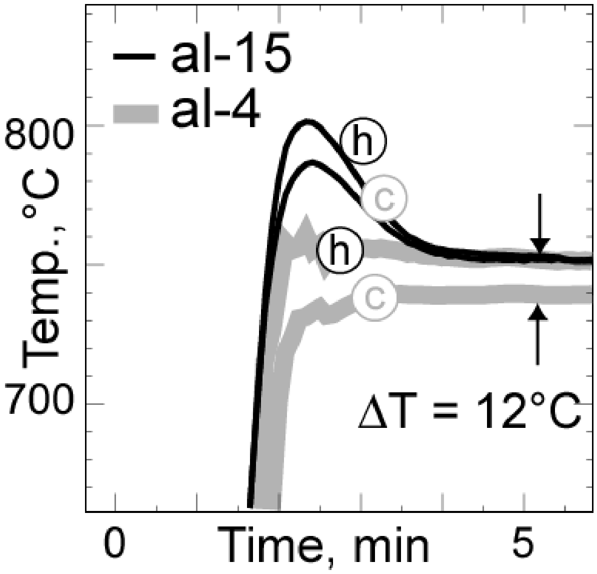

Fig. 8.10 Heated plate thermocouple readings for experiments al-15 and al-4.

The difference between the “h” and “c” bottom plate thermocouple reading is not obvious when the temperatures are plotted on the scales shown in Figs. 9.6 through 9.9. However, some differences are apparent. For example, Fig. 8.10 shows a zoomed-in view of the “h” and “c” thermocouple temperature for experiments al-4 and al-15. The difference in the “h” and “c” temperature for experiments al-4 and al-15 at 5 minutes is 2°C and 12°C, respectively. It is difficult to know why the temperatures are so different for these replicate experiments. Contact resistance and thermocouple error are two possible explanations. Rather than speculate further, the SPUF boundary conditions are considered only as an *estimate* of the actual boundary condition.

The pressure for the SPUF simulations was assumed constant with most of the experiments set to 1-atm. For the partially confined experiments; 600-amb-p4, 600-1.54-p2, and 600-3.58-p3; the pressure was set to 1-atm, 1.54-atm, and 3.58-atm, respectively. Figure 8.11 shows the measured pressure for these experiments. The errors associated with using a constant pressure are negligible since the mass loss shifts calculated with the SPUF model are negligible at these conditions. Future foam response models should calculate the dynamic pressurization using the predicted molecular weights of the decomposition gases taking into account gases that may enter or leave the enclosure due to confinement conditions.

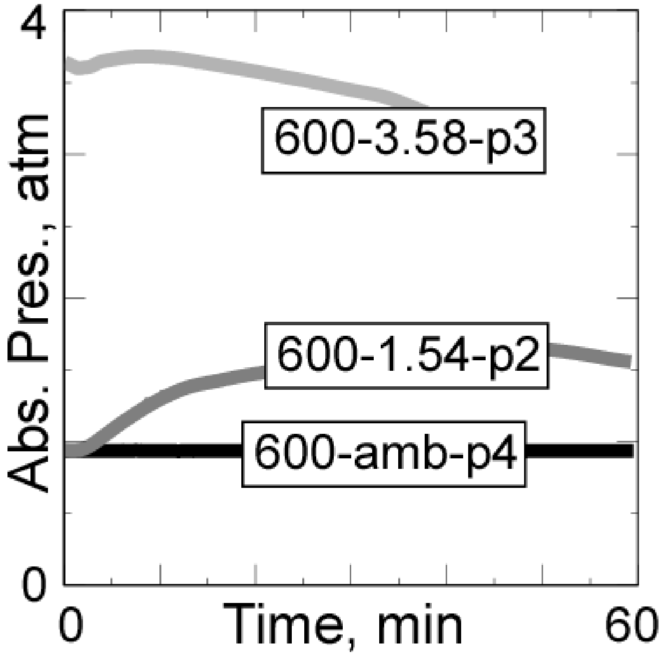

Fig. 8.11 Measured pressures for the partially-confined radiant heat experiments.

8.3 Experimental Observations

Figure 8.12 shows the effect of the boundary temperature and foam density on the centerline front locations as measured from the heated cup plate and velocities for experiments 600-1, 750-2, 900-14, ss-1000-19, ld750-12; Figure 8.13 shows the effect of pressurization and confinement on the centerline front locations for experiments 600-1, 600-amb-p4, 600-1.54-p2, 600-3.58-p3. Centerline front locations for the remaining experiments were not plotted since they are essentially the same as the representative experiments shown in Fig. 8.12 and Fig. 8.13. In these figures, the lines represent the *measured* front locations and velocities determined from a

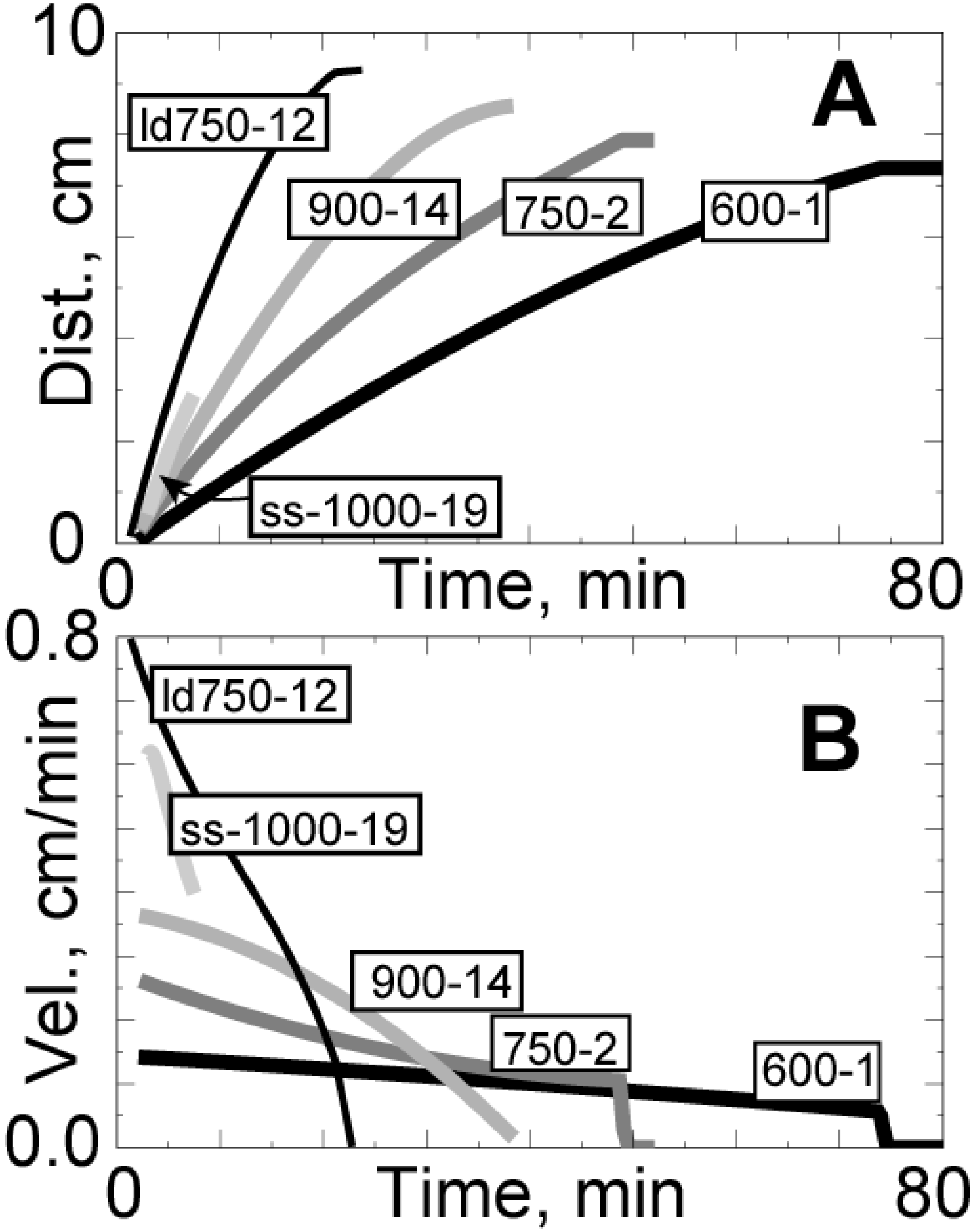

Fig. 8.12 A) Decomposition front locations measured from the heated plate and B) measured front velocities showing the effect of heated plate temperature (experiments 600-1, 750-2, 900-14, and ss-1000-19 and density (ld750-12).

series of X-ray images taken at various time intervals ranging from 5-60 seconds. The location of the decomposition front was determined using various image-processing software.

In Fig. 8.12, the front velocity is shown to increase with increasing plate temperatures for the high-density foam. The velocity of the low-density experiment ld750-12 was about 3 times faster than the velocity of the high-density experiment 750-2, even though the thermal conductivity for the higher density foam was greater than the thermal conductivity of the lower density foam. The primary reason for the faster decomposition velocity for the lower density foam was a lower volumetric energy sink for the low-density foam. In other words, fewer bonds needed to be

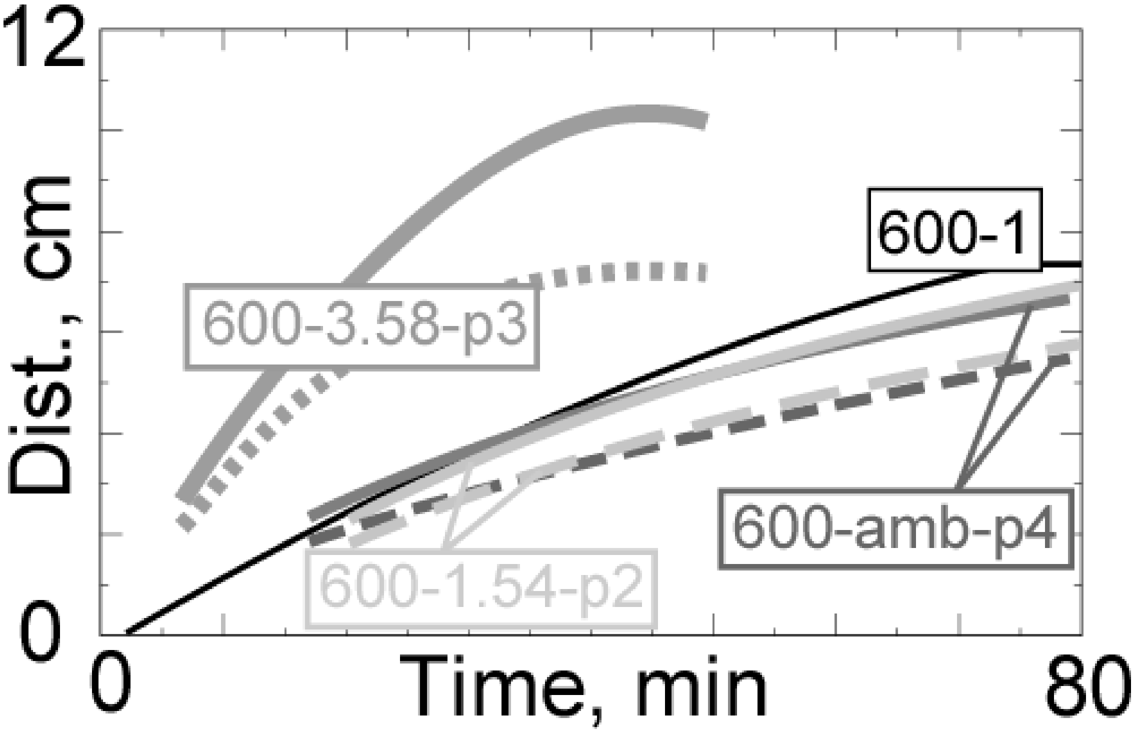

Fig. 8.13 Measured decomposition front locations showing the effect of confinement and pressure (600-1 is unconfined at ambient pressure, 600-amb-p4 is partially confined at ambient pressure, 600-1.54-p2 is partially confined at 0.16-MPa, and 600-3.58-p3 is partially confined at 0.36-MPa.

broken to decompose the same volume of material. Determination of the front velocities for the remaining lower density foam X-rays was not attempted due to difficulty in analyzing the low contrast X-ray film.

Figure 8.13 shows the centerline front locations for experiments 600-1 and 600-amb-p4, 600-1.54-p2, 600-3.58-p3 to illustrate the effect of confinement and pressure during decomposition of the RPU encapsulant in large-scale experiments. The front locations for the partially confined experiments 600-amb-p4, 600-1.54-p2, 600-3.58-p3 are shown with two lines – a solid line and a broken line – representing the interface between the *foam and bubbly liquid* and *bubbly liquid and gas*. The SPUF model does not include the effects of confinement or pressurization. Thus the SPUF simulations give confinement-independent and pressure-independent results.

The increased decomposition velocity at 0.36-MPa may be related to substantial liquid formation caused by partial confinement of the decomposition gases and increased pressure. The cellular structure, composed of struts and windows separating gas-filled bubbles, disappears when the polymer liquefies. The loss of the cellular structure causes the local density to increase as observed in the X-ray images. The disappearance of the cellular structure at the heated surface is partially responsible for the observed increase in the decomposition front velocity. The decomposition front is also accelerated as the heat transfer rate is increased due to the higher thermal conductivity of the liquid front and convective heat transfer within the bubbly liquid.

Figure 8.14 gives an overlay of the X-ray images for the partially confined RPU experiments after 30 minutes to show the nonlinearity of the decomposition fronts with pressure. The X-ray movies of the 0.3-MPa experiment showed damage occurring within the closed-cell foam as cell windows opened (ruptured) and a liquid plume penetrated into the previously closed-cell foam. Predicting damage caused by decomposition chemistry and pressure loading is beyond the current capability of the FEM code.

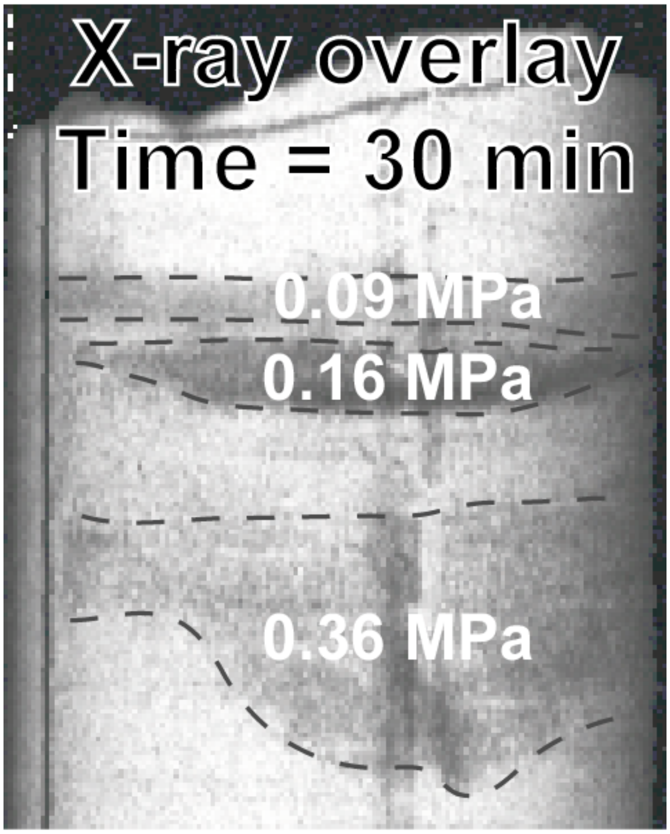

Experiments:
600-amb, 600-1.54, 600-3.58

Fig 8.14 Overlay of three X-ray images taken at 30 minutes for experiments 600-amb-p4, 600-1.54-p2, and 600-3.58-p3.

9 SPUF Simulations of the Radiant Heat Experiments

Table 9.1 lists 19 different experiments that were simulated using both the CPUF and SPUF foam response models. Table 9.1 is an index of the simulations of the 19 radiant heat experiments, which are given in Figures 9.1 through 9.19. All of the 2D-axisymetric simulations were performed using COYOTE and the 3D-simulations were run with CALORE, which currently lacks 2D capability. The SPUF simulations were performed using seven different element types,

Table 9.1 SPUF and CPUF simulations

Effect	Identifier*	Figure[†,‡]
Plate temperature (high density)	600-1	9.1
	750-2	9.2
	900-3	9.3
	900-14	9.4
Plate temperature (low density)	ld600-6	9.5
	ld750-12	9.6
	ld900-7	9.7
Orientation	side-11	9.8
	side-13	9.9
	top-10	9.10
Component (high density)	al-4	9.11
	al-15	9.12
	ss-1000-19	9.13
	ss-5	9.14
Component (low density)	ldal-8	9.15
	ldss-9	9.16
Confinement	600-amb-p4	9.17
	600-1.54-p2	9.18
	600-3.58-p3	9.19

*See Table 8.1 for a more detail description

[†] The left-hand-side of A, B, C, E, and F show CPUF results calculated with a 0.10-cm regular quadrilateral mesh (0.10regQUAD). The right-hand-side of A, B, C, E, and F show SPUF results with the following mesh types:

A: 0.25-cm regular 2D quadrilateral elements (0.25regQUAD)
B: 0.50-cm regular 2D quadrilateral elements (0.50regQUAD)
C: 1.00-cm regular 2D quadrilateral elements (1.00regQUAD)
E: 2D paved quadrilateral elements (PavedQUAD)
F: 0.5-cm 2D triangular elements (0.5TRI)

[‡] G shows SPUF results on the left-hand-side using 1.00-cm 2D triangular elements (1.00TRI). The right-hand-side in G shows a slice plane through a 3D SPUF simulation using 3-D tetrahedral elements (1.00TET). D and H show X-ray images of the radiant heat experiments.

which are described in the footnote of Table 9.1. All of the CPUF simulations were performed using 0.1-cm regular (square) quadrilateral elements. The parameters for the SPUF model were discussed previously in Section 3-7. The primary objective of the simulations presented in this section is to show that the SPUF discretization bias corrected solutions give similar results for a wide variety of mesh types, the SPUF foam response model gives similar results to the CPU-intensive CPUF model, and the SPUF results are compared to various X-rays at selected time intervals. The SPUF model predictions are in better agreement with the X-ray data for unconfined foam response. No adjustable parameters are used in the simulations described in this section.

Figures 9.1-9.19 show a comparison between X-rays and the solid fraction contours calculated with both the CPUF and SPUF foam response models for the 19 experiments listed in Table 9.1. The two-dimensional axisymmetric calculations (Figures A-C and E-G in Figs. 9.1-9.7 and Figs 9.10-9.19) are plotted to the left of each of the X-ray images in these figures. For the side-heated experiments in Figs. 9.8-9.9, the X-rays are plotted on the bottom to compare the front locations. The CPUF calculations used a mesh composed of 0.1-cm regular quadrilateral elements. The right-hand-side of the image was calculated using the SPUF foam response model using various element types. Plot G shows two SPUF calculations with the left-hand-side of the image calculated using 2D triangular elements and the right-hand-side of the image calculated using 3D tetrahedral elements. The images show three black solid fraction contour lines calculated with both the CPUF and SPUF model representing the values 0.2, 0.5, and 0.8. The 0.2 contour lines are closest to the heated surface, the 0.5 contour lines are the middle lines, and the 0.8 contour lines are farthest from the heated surface. The solid fraction is the mass of the foam in the element divided by the initial foam mass in the element at time zero. The low thermal conductivity of the foam encapsulant causes the decomposition front to be narrow when exposed to high temperatures. Three X-ray images at various times for each experiment are shown with arrows to show the approximate location of the decomposition front.

The effect of the heated plate temperature for the experiments with the higher density foam is shown in Figs. 9.1-9.4. Increasing temperatures causes the bond breaking rates to increase in an Arrhenius fashion. Consequently, the velocity of the decomposition front also increases with temperature resulting in the position of the front being located farther from the heated surface at equivalent times. A similar effect is shown in Figs. 9.5-9.7, which depicts the temperature effect for the low-density foam. However, the decomposition rate is significantly greater for the lower density foam, than for the higher density foam. For the lower density foam, the volumetric endothermic energy change is not as profound as for the higher density foam. The result is an increase in the decomposition front velocity for the lower density foam. Thermophysical properties of the foam also affect the velocity of the decomposition front.

Replicate experiments are shown in Fig. 9.3 and 9.4 for the high-density experiments with the plate temperature set to 900ºC. Experiment 900-3 was repeated due to an oscillation in the control thermocouple. The X-ray images show that the decomposition front for experiment 900-3 and 900-14 are at nearly the same location; however, the predicted front location for experiment 900-3 is in better agreement than the predicted front location for experiment 900-14. The bottom plate temperature measured with thermocouple “c” was used for the 900-3 boundary condition; and bottom plate temperature measured with thermocouple ‘h’ was used for the 900-14 boundary condition. The location of the applied temperature boundary condition was always at the location of the “c” thermocouple shown in Fig. 8.5. Thus, the “c” thermocouple temperature is thought to be more representative of the actual boundary condition. The better agreement between the predicted and measured decomposition front locations for experiment 900-3 are likely due to a better representation of the thermal boundary condition.

An anomaly is shown in Fig. 9.7 near the centerline of the CPUF predictions of the effect of a 900ºC boundary temperature on the response of low-density foam. The shape of the predicted solid fraction contour for the CPUF model has unnatural curvature near the centerline. This behavior is not observed for the SPUF predictions. In fact, a stray element is seen in the CPUF predictions at 5 minutes. This “zombie element” was not removed from the computational domain due to a numerical oscillation that caused local nodes within this element to have disparate temperatures. Some of the node temperatures were hot and some of the node temperatures were cold, which prevented the average solid fraction with the “zombie element” to drop below the specified “death criterion”. In the current context, a “zombie element” is referred to an element that should be dead (removed from the computational domain) but is not. This numerical instability did not occur in any of the other simulations. The combination of low-density and high thermal boundary temperature produced the highest front velocities in agreement with the experimental data. A similar calculation using CALORE for experiment LD900-7 did not have any numerical instability.

Figures 9.8-9.10 show the effect of the heating orientation on the shape of the decomposition front. The foam studied in this report does not exhibit strong liquefaction behavior when the foam is decomposed under ambient pressure with sufficient venting of the decomposition gases. Thus, orientation effects are shown to be negligible, although slight variations are shown in the X-rays of the two side-heated experiments. Side-13 is a replicate of experiment Side-11. In experiment Side-11, the X-ray shield started to slowly creep into the line of site of the X-ray camera. Another difference between experiment Side-11 and Side-13 was the steady-state temperature of the “c” thermocouple. The steady-state temperature of the “c” thermocouple for experiment Side-11 was about 4ºC colder than the steady-state temperature of the “c” thermocouple for experiment Side-13. The temperature differential of 4ºC caused the centerline front locations to differ by about 1-cm by the end of the experiment, giving an indication of the sensitivity of the radiant heat experiments to the boundary temperature. Since the radiant heat experiments were done some time ago, other uncertainties such as density may have contributed to differences between Side-13 and Side-11.

Figures 9.11 to 9.16 show the effect of components on the decomposition front for both the higher density foam and the lower density foam, respectively. The effect of two types of components were studied – 1) a hollow aluminum component and 2) a solid stainless-steel component. The hollow aluminum component has a lower thermal capacitance than the solid stainless-steel components. The components do not significantly influence the decomposition of the encapsulant until the component is exposed to the heated plate. The lower capacitance, hollow aluminum component heats more rapidly than the higher capacitance solid stainless steel component. The temperature of the hollow aluminum component rapidly reaches decomposition temperatures and decomposition of the encapsulant is accelerated near the surface of the component. Conversely, the temperature of the solid stainless steel component heats slowly. Calculated fronts locations match the front locations shown in the X-ray images as density variations.

Figures 9.17-9.19 show the effect of partial confinement at various levels of backpressure for a steady-state plate temperature of 600ºC. As shown previously in Fig. 9.1.C, the decomposition gases were vented to a backpressure regulator. The backpressure (shown in Fig. 9.11) was regulated to be nominally 0.9-atm, 1.54-atm, and 3.58-atm for Figures 9.17, 9.18, and 9.19, respectively. The higher backpressures cause the CPUF predicted decomposition front velocities to slow. The delay in the predicted front velocity is a result of the pressure-dependent vapor-liquid equilibrium model. As the backpressure is increased, the predicted V/L ratio decreases since the vapor-liquid equilibrium ratio or *K-value* is lowered with higher hydrodynamic pressure ($K_i \propto 1/P$). The SPUF foam response model does not depend on pressure and the SPUF predictions in Figs. 9.17-9.19 are essentially the same. The only differences in the SPUF predictions in Figs. 9-17-9.19 are related to the thermal boundary conditions.

The width of the reaction zone (decomposition front) for the *unconfined* samples in Figs. 9.1 to 9.16 appeared in the X-ray images to be narrow with little or no liquid accumulation. In contrast, the reaction zones in the *partially confined* samples shown in Fig 11.6 were broad with significant liquid accumulation even at ambient pressures. The front velocities decreased with moderate increases in absolute pressures from ambient (600-amb) to 0.16-Mpa (600-1.54), which was consistent with high-pressure TGA experiments. However, as the pressure was increased further in 600-3.58 (to 0.36-Mpa), the front velocity increased dramatically. The increased velocity of the *partially confined RPU at high- pressure* was associated with liquefaction and enhanced heat transfer in the reaction zone. A subgrid model may be able to account for enhanced thermophysical property enhancement associated with liquid formation and flow. Such a subgrid model is beyond the scope of the current CPUF and SPUF foam response model.

The validation of SPUF's discretization bias correction model of using various mesh sizes goes beyond merely capturing the location or boundary of the dynamically developing enclosure. Characterization of energy transport to embedded components also depends on the physical state of the degrading foam. The cellular structure, composed of struts and windows separating gas-filled bubbles, disappears when the polymer liquefies. The loss of the cellular structure causes the local density to increase as observed in the X-ray images (Figs 9.17-9.19). The disappearance of the cellular structure at the heated surface is partially responsible for the observed increase in the decomposition front velocity. The decomposition front is also accelerated as the heat transfer rate is increased due to the higher thermal conductivity of the liquid front and convective heat transfer within the bubbly liquid. An X-ray movie of the 0.3-MPa experiment 600-3.58 showed damage occurring within the closed-cell foam as cell windows opened (ruptured) and a liquid plume penetrated into the previously closed-cell foam. Predicting damage caused by decomposition chemistry and pressure loading is beyond the current capability of the FEM code and is left as an unsolved research topic.

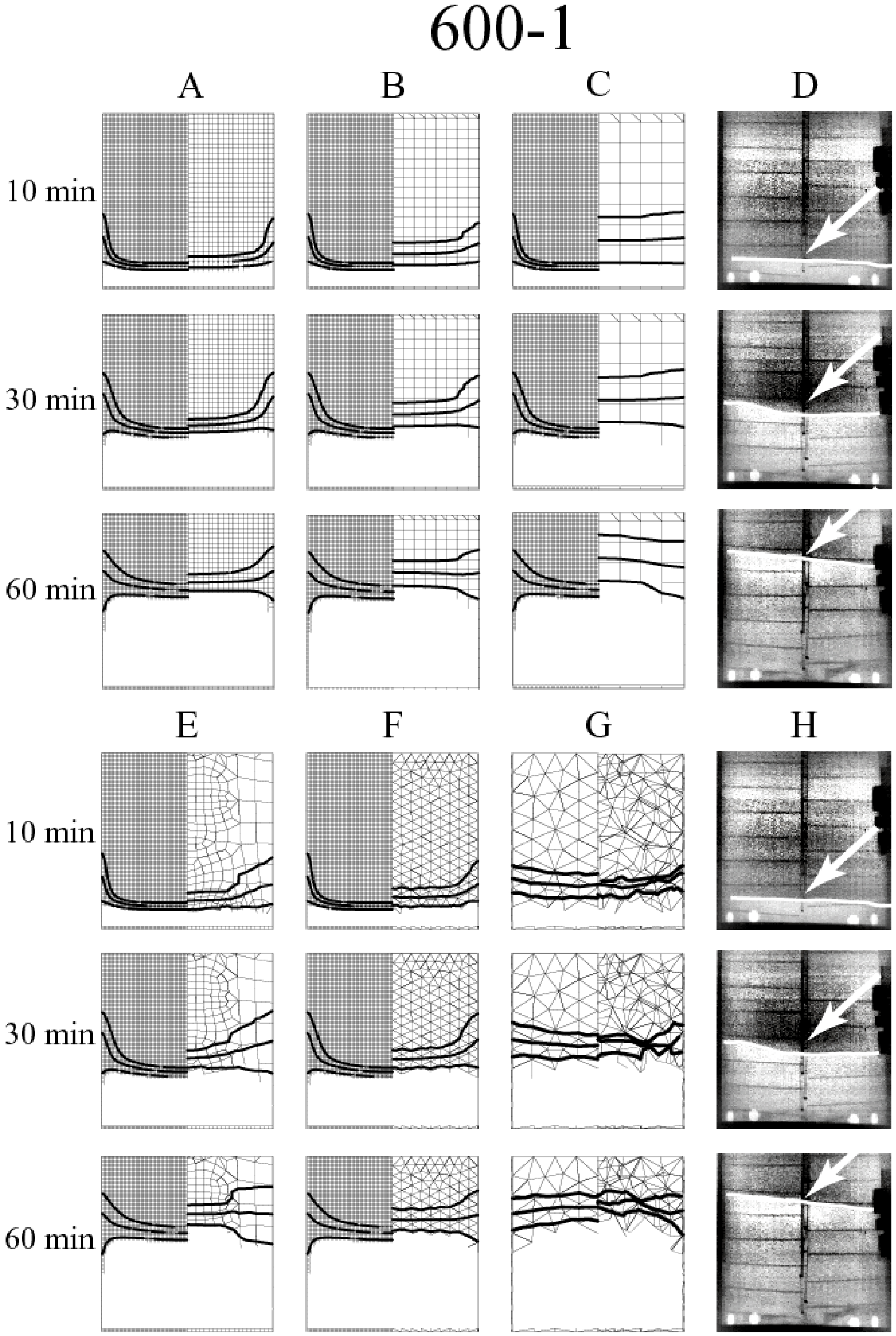

Fig. 9.1. Comparison between SPUF predictions using various mesh types and sizes as described in the footnote of Table 9.1and X-ray images for experiment 600-1

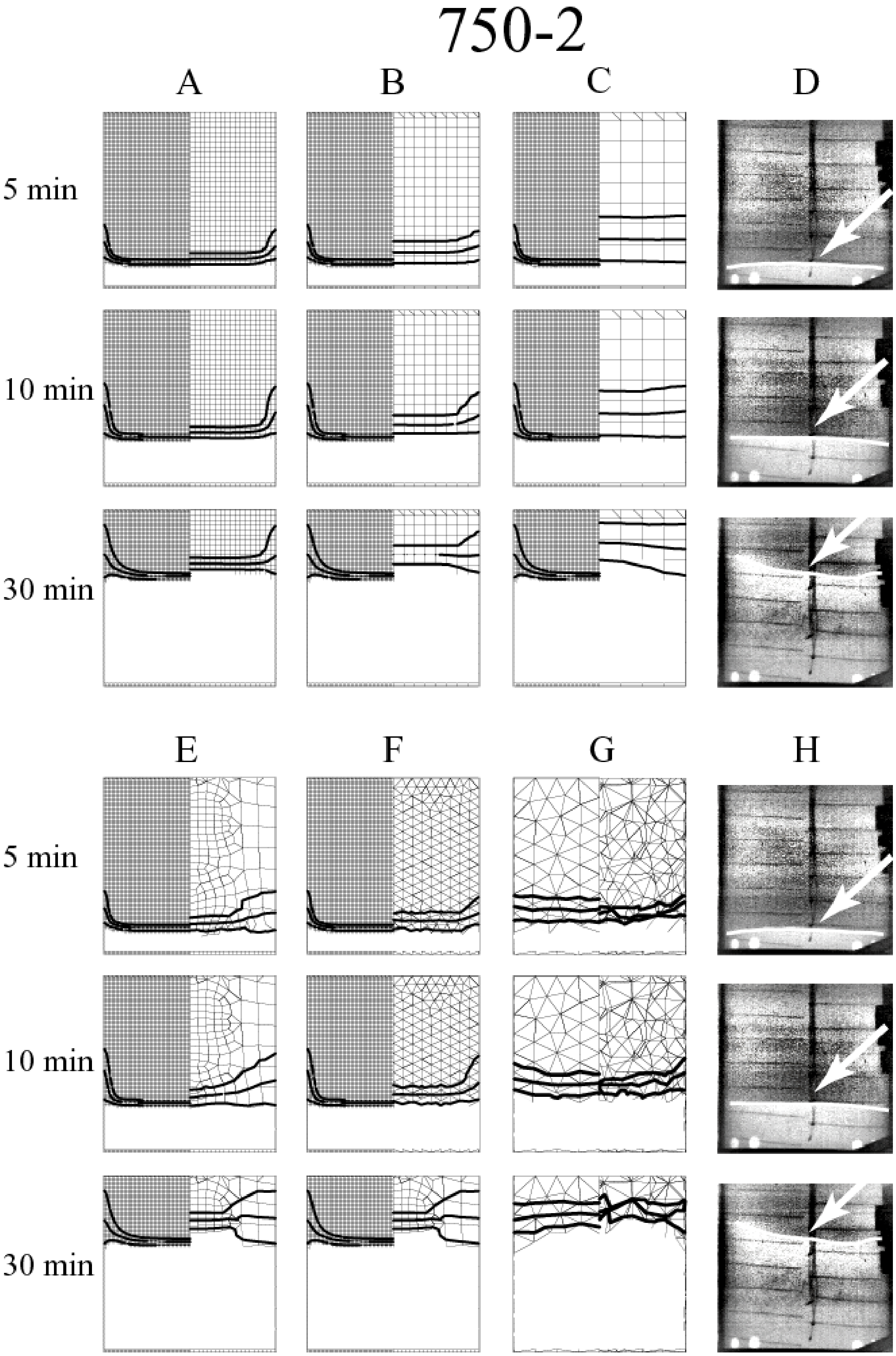

Fig. 9.2. Comparison between SPUF predictions using various mesh types and sizes as described in the footnote of Table 9.1and X-ray images for experiment 750-2.

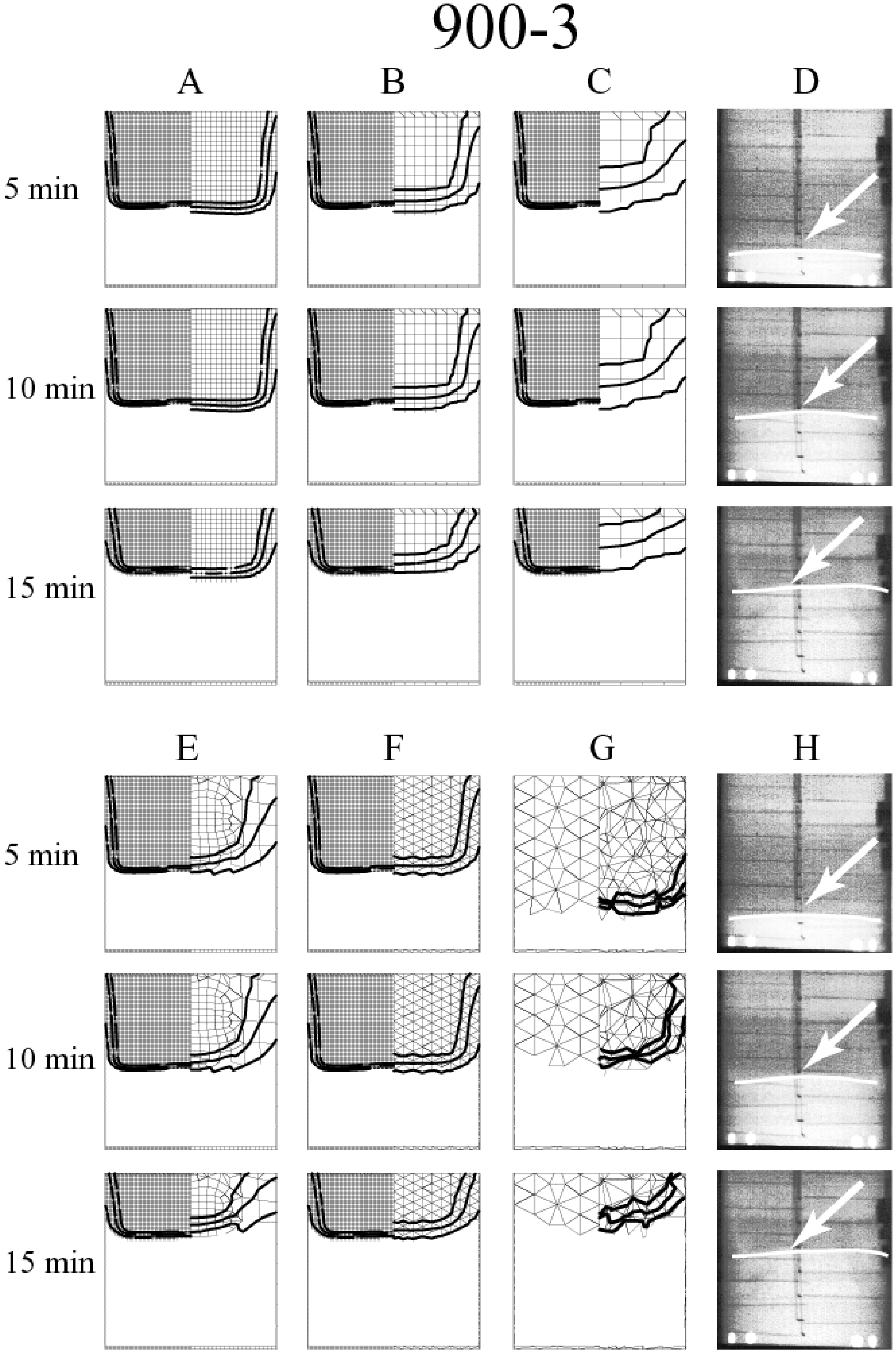

Fig. 9.3. Comparison between SPUF predictions using various mesh types and sizes as described in the footnote of Table 9.1and X-ray images for experiment 900-3.

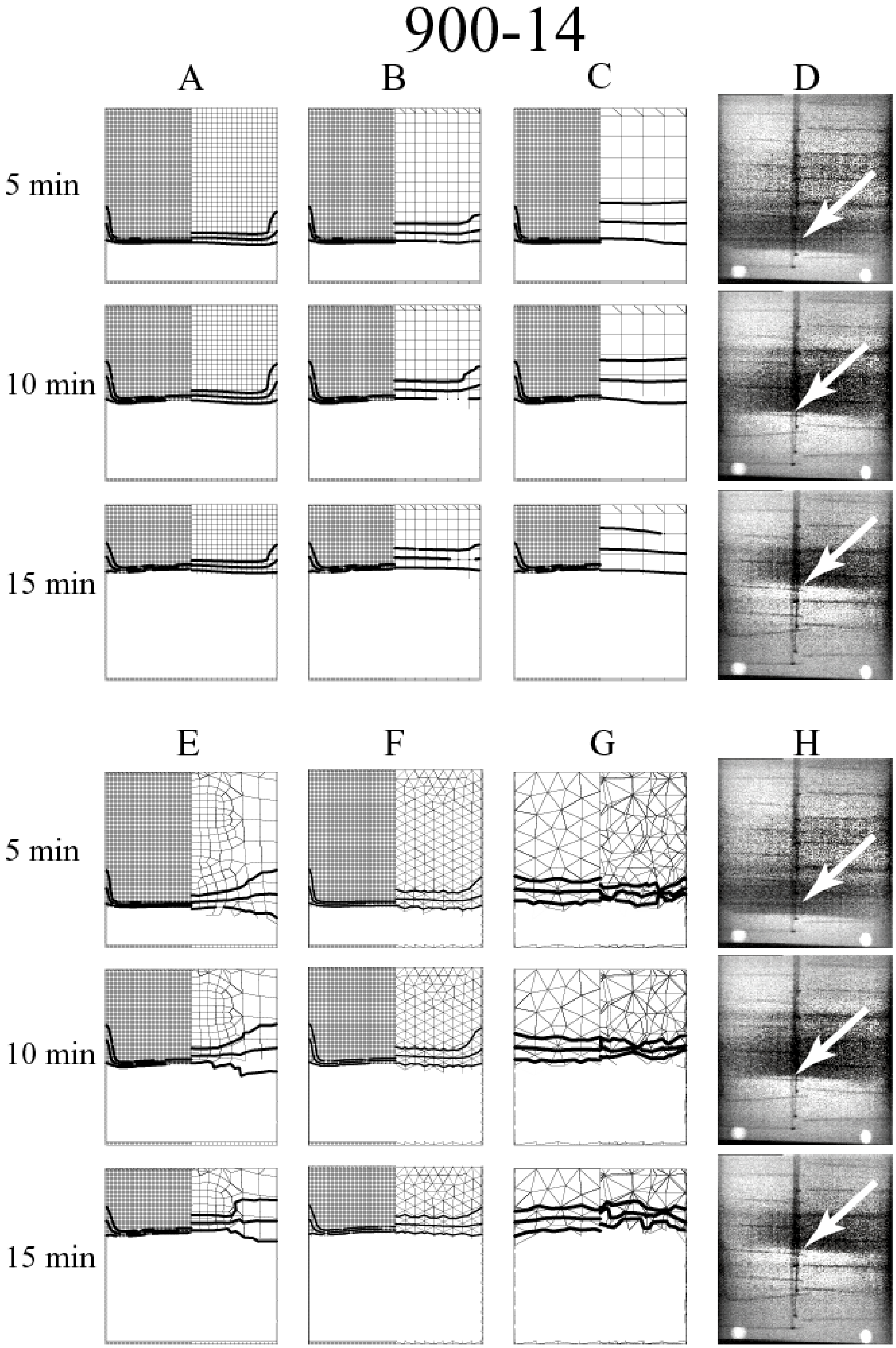

Fig. 9.4. Comparison between SPUF predictions using various mesh types and sizes as described in the footnote of Table 9.1and X-ray images for experiment 900-14.

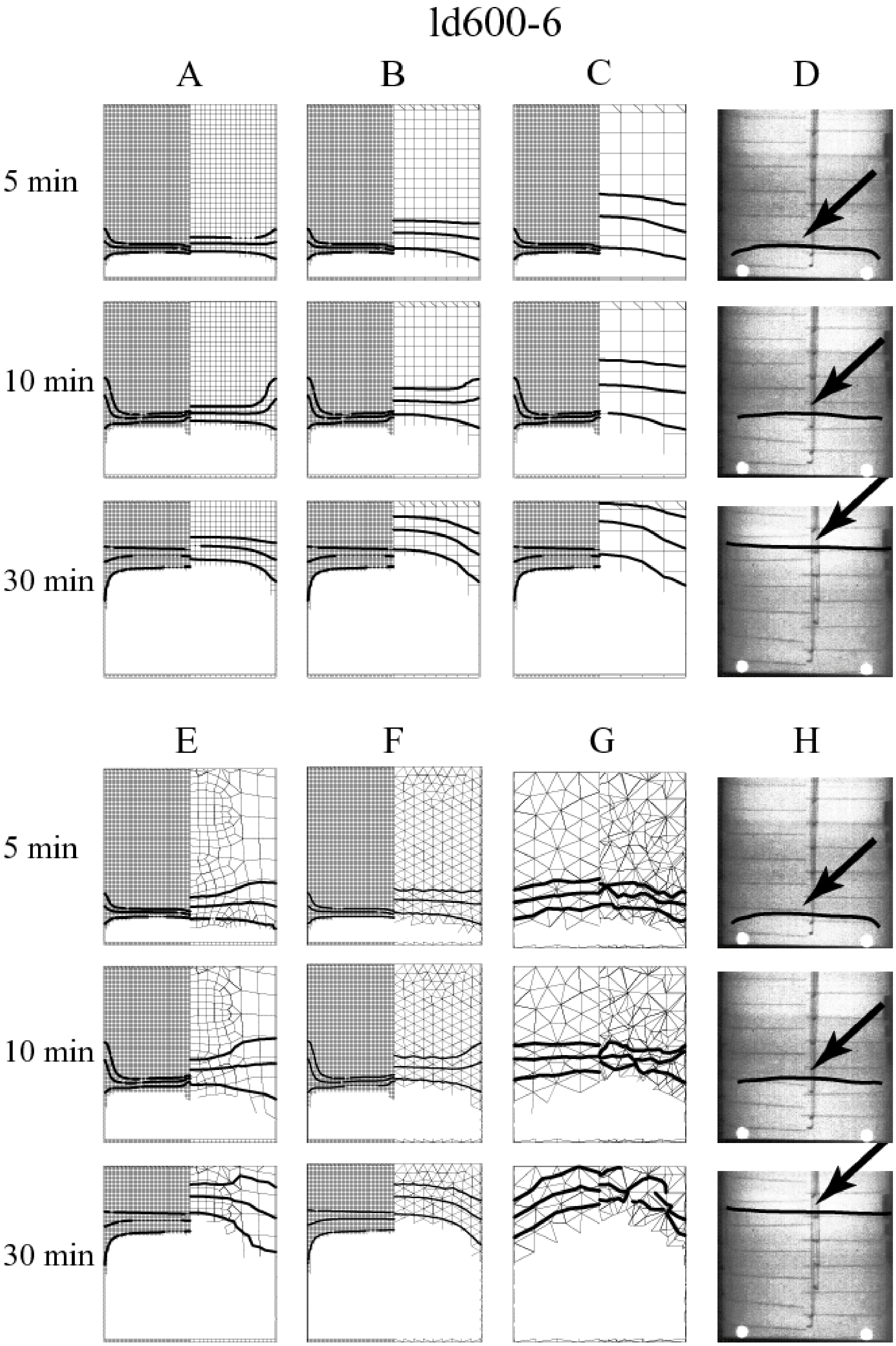

Fig. 9.5. Comparison between SPUF predictions using various mesh types and sizes as described in the footnote of Table 9.1and X-ray images for experiment ld600-6.

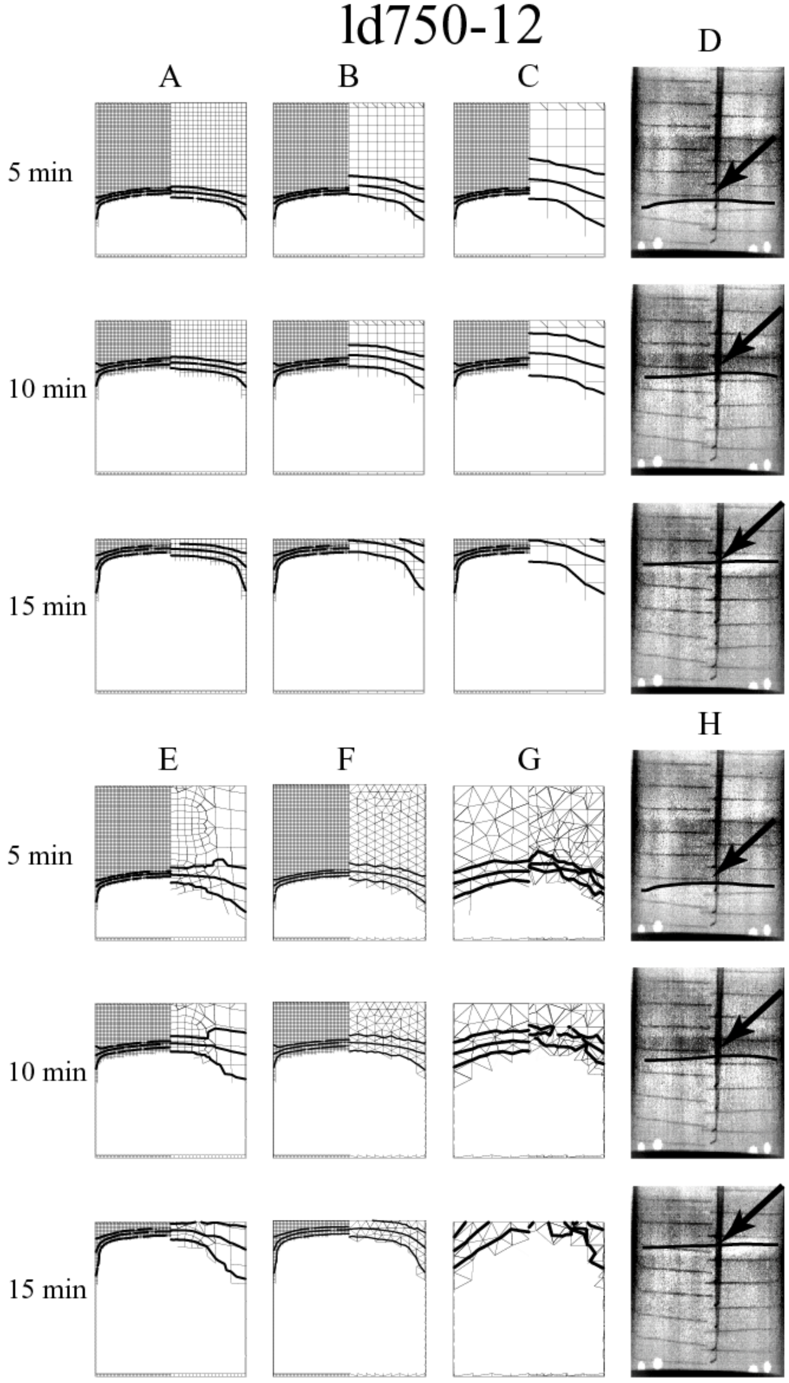

Fig. 9.6. Comparison between SPUF predictions using various mesh types and sizes as described in the footnote of Table 9.1and X-ray images for experiment ld750-12.

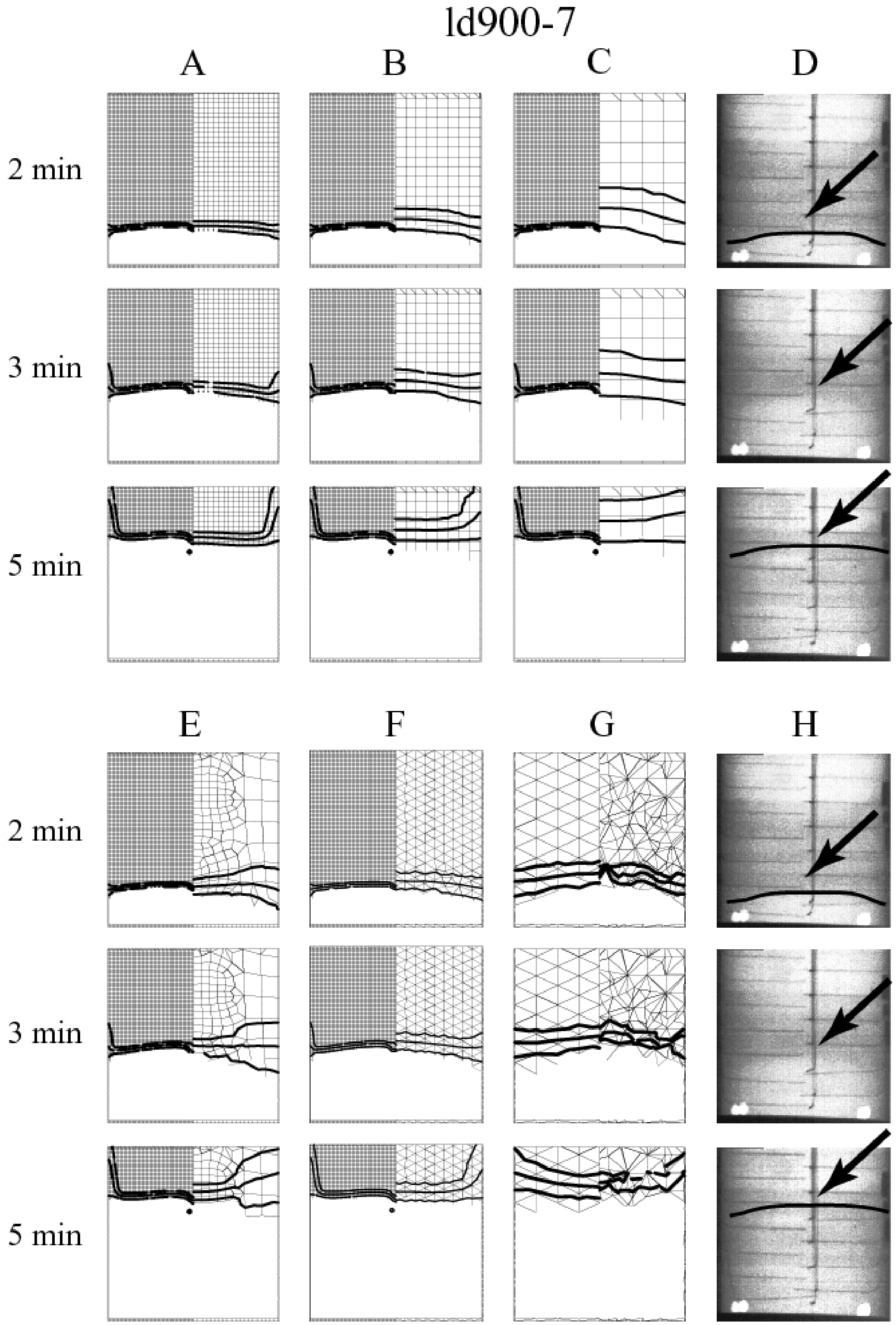

Fig. 9.7. Comparison between SPUF predictions using various mesh types and sizes as described in the footnote of Table 9.1and X-ray images for experiment ld900-7.

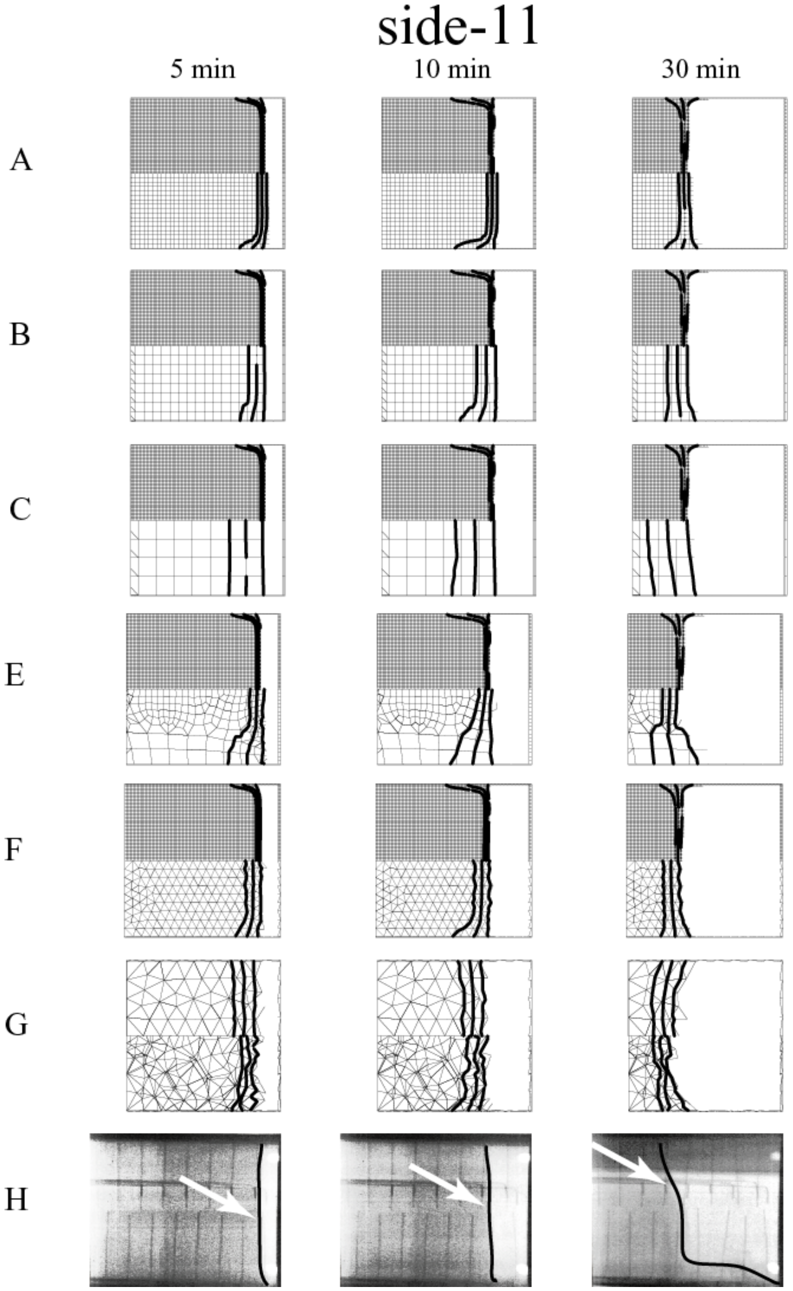

Fig. 9.8. Comparison between SPUF predictions using various mesh types and sizes as described in the footnote of Table 9.1and X-ray images for experiment side-11. Plot D is not shown for the side-heated experiments since plot D is a replica of plot H.

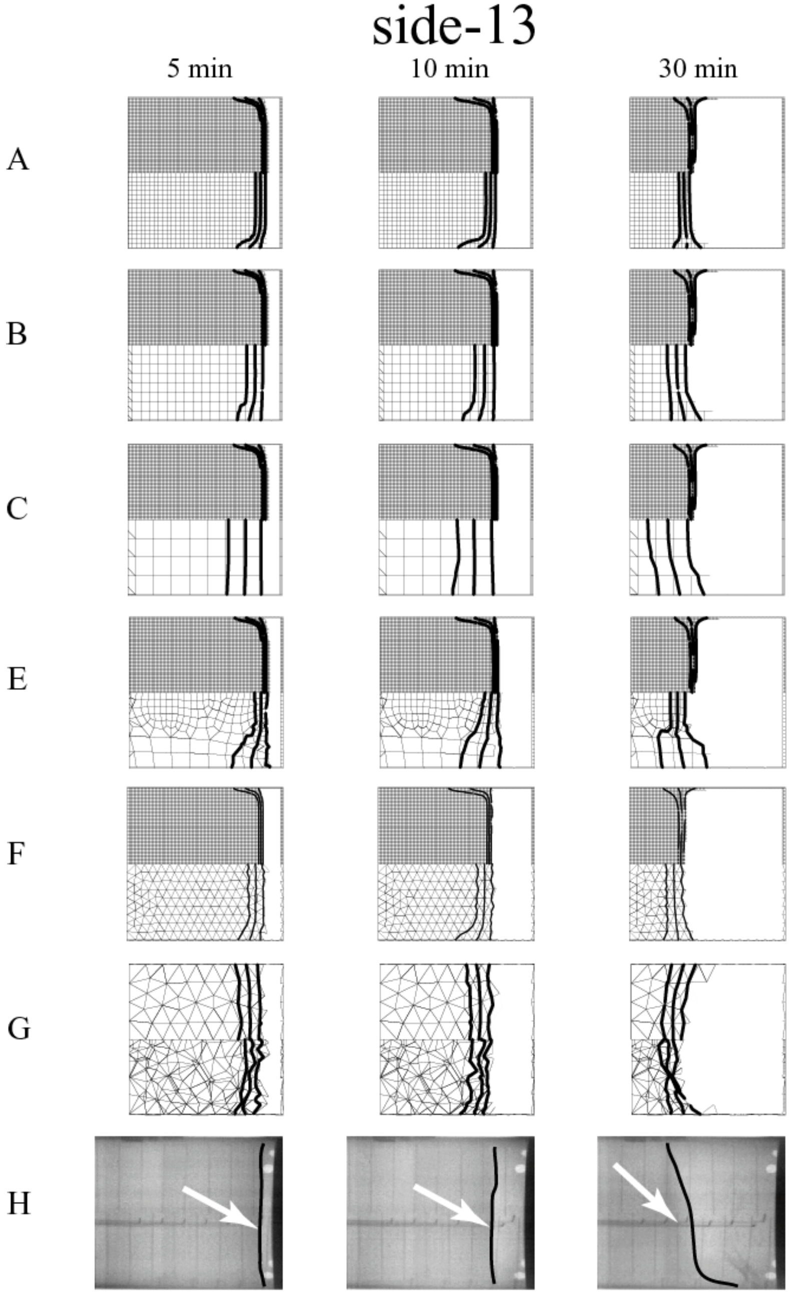

Fig. 9.9. Comparison between SPUF predictions using various mesh types and sizes as described in the footnote of Table 9.1and X-ray images for experiment side-13. Plot D is not shown for the side-heated experiments since plot D is a replica of plot H.

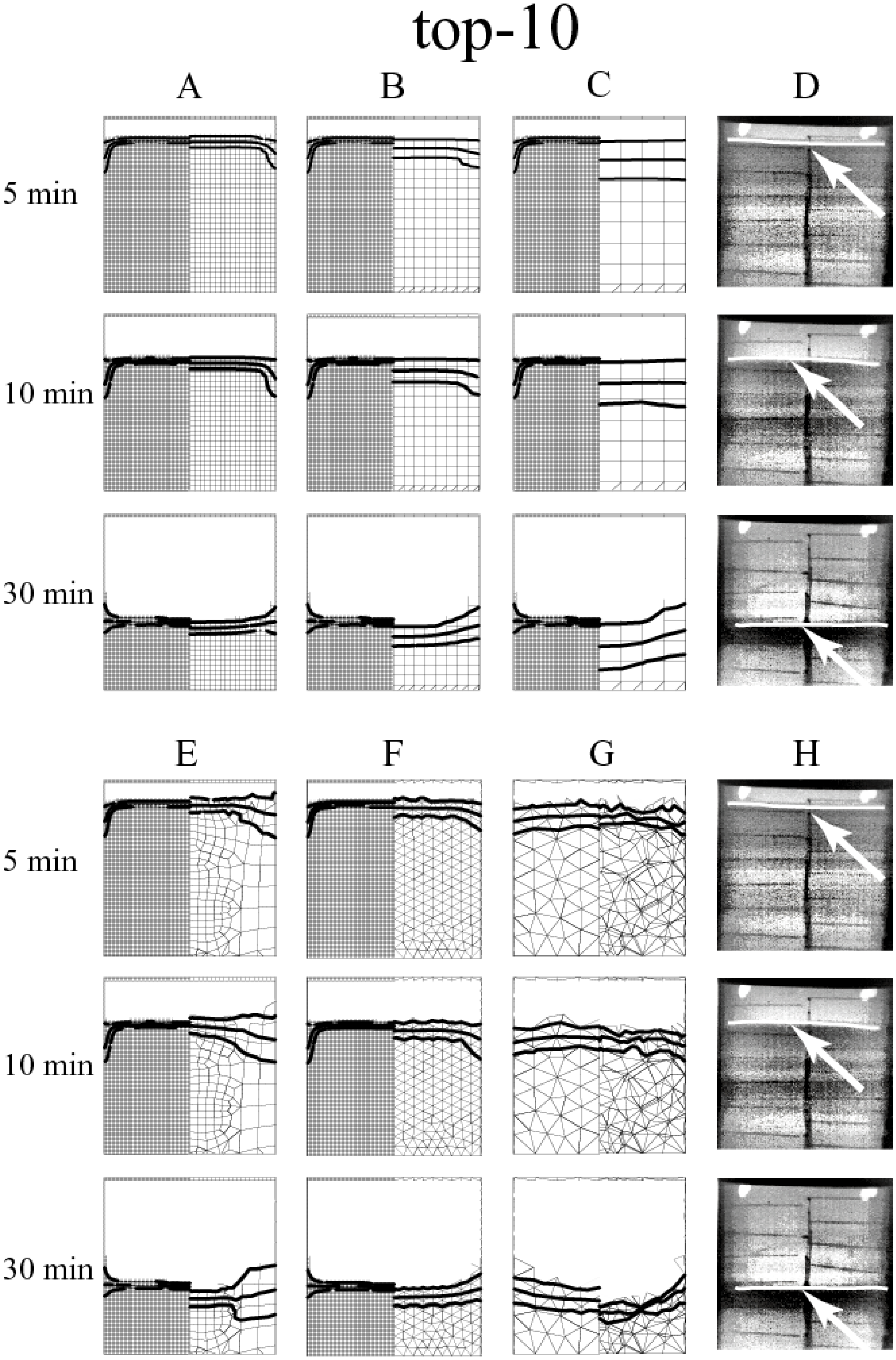

Fig. 9.10. Comparison between SPUF predictions using various mesh types and sizes as described in the footnote of Table 9.1and X-ray images for experiment top-10.

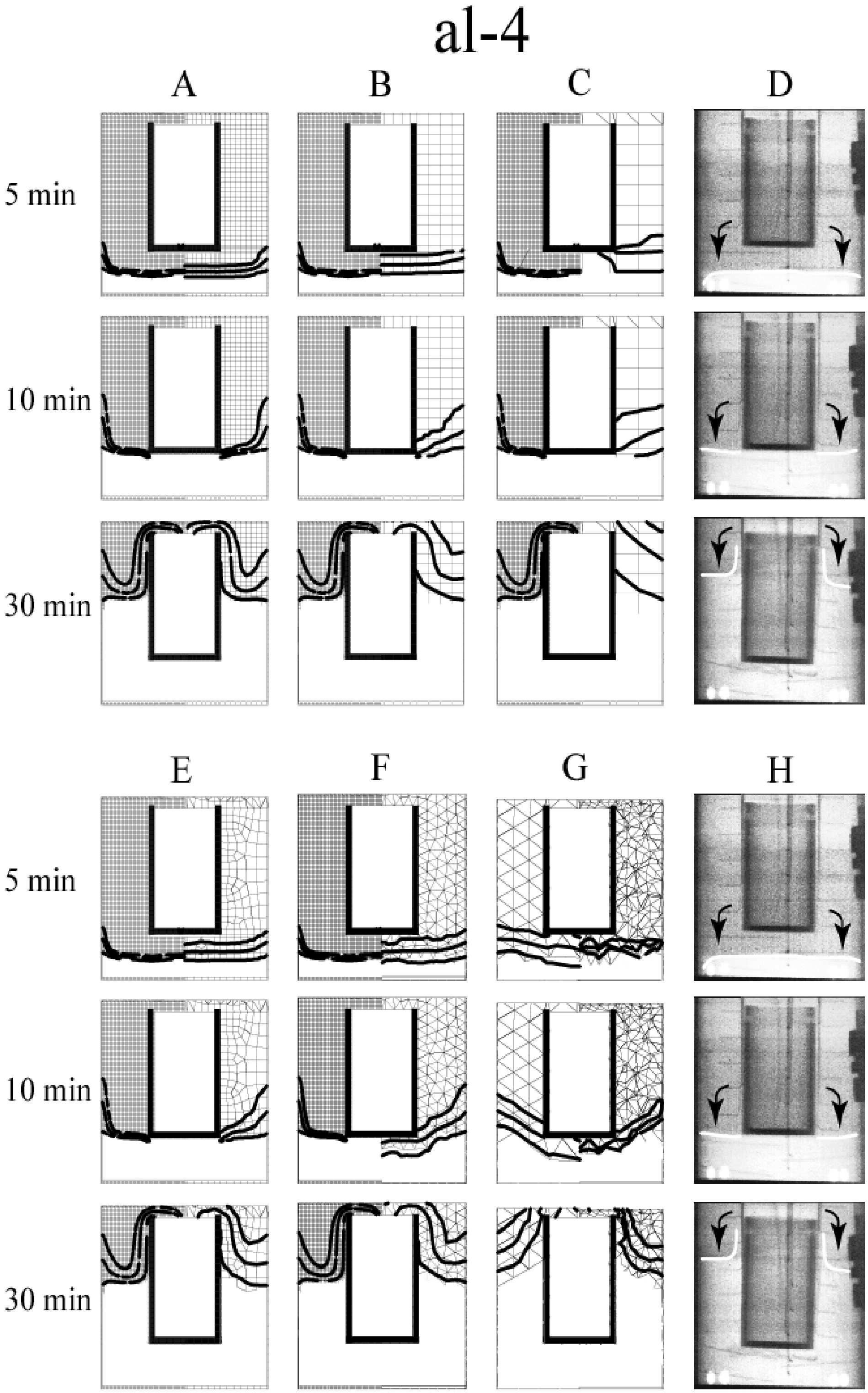

Fig. 9.11. Comparison between SPUF predictions using various mesh types and sizes as described in the footnote of Table 9.1and X-ray images for experiment al-4.

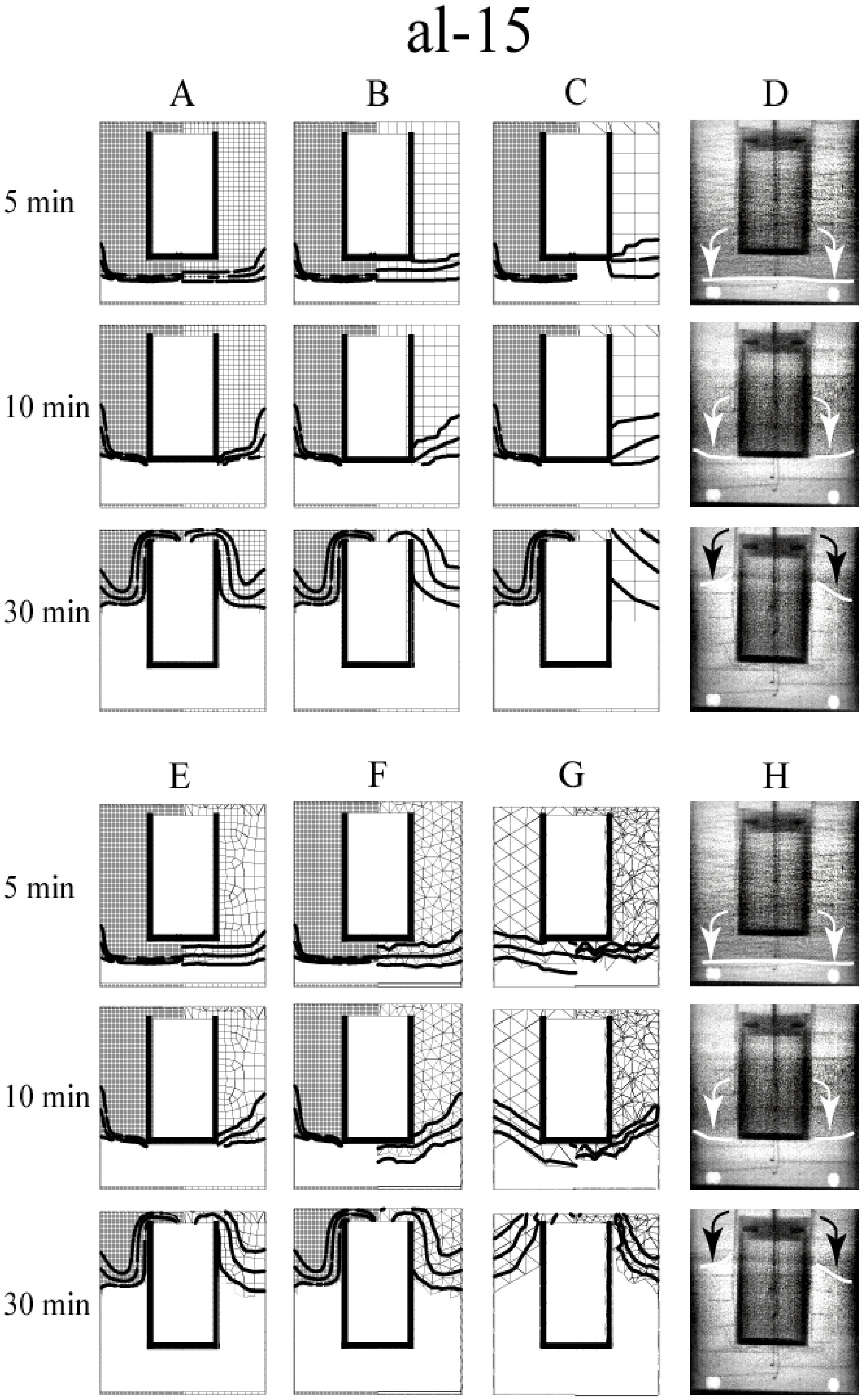

Fig. 9.12. Comparison between SPUF predictions using various mesh types and sizes as described in the footnote of Table 9.1and X-ray images for experiment al-15.

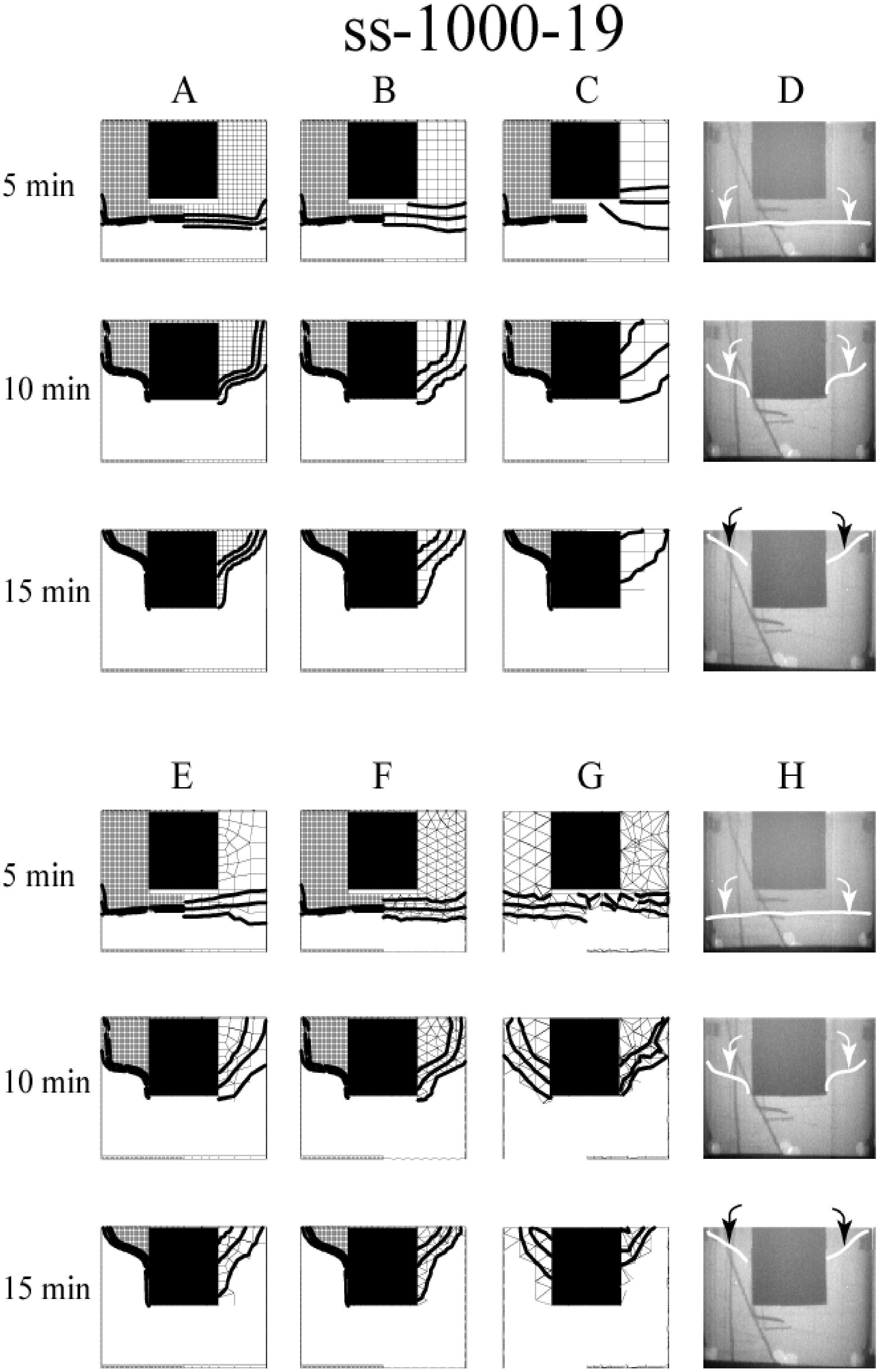

Fig. 9.13. Comparison between SPUF predictions using various mesh types and sizes as described in the footnote of Table 9.1and X-ray images for experiment ss-1000-19.

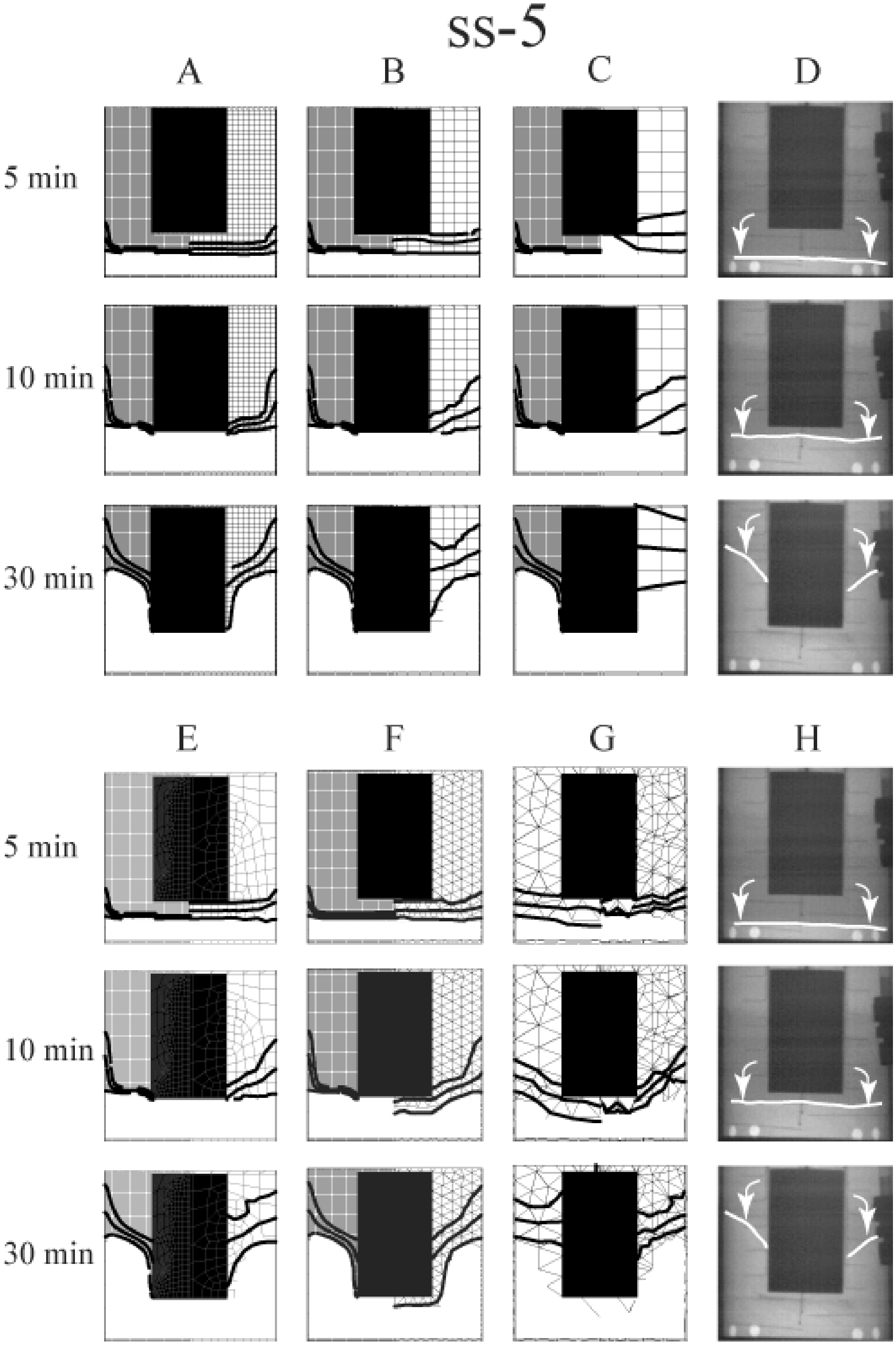

Fig. 9.14. Comparison between SPUF predictions using various mesh types and sizes as described in the footnote of Table 9.1and X-ray images for experiment ss-5.

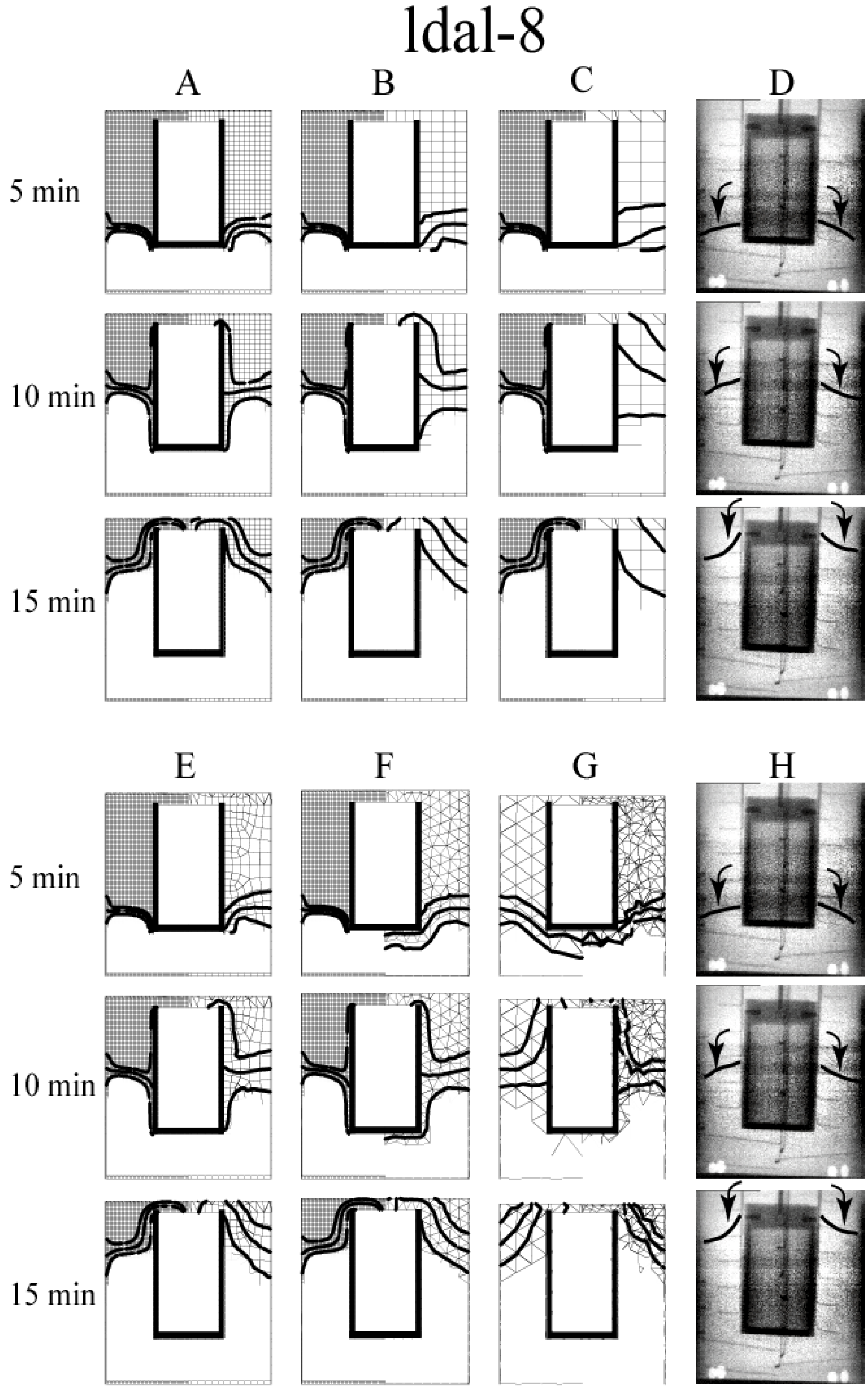

Fig. 9.15. Comparison between SPUF predictions using various mesh types and sizes as described in the footnote of Table 9.1and X-ray images for experiment Idal-8.

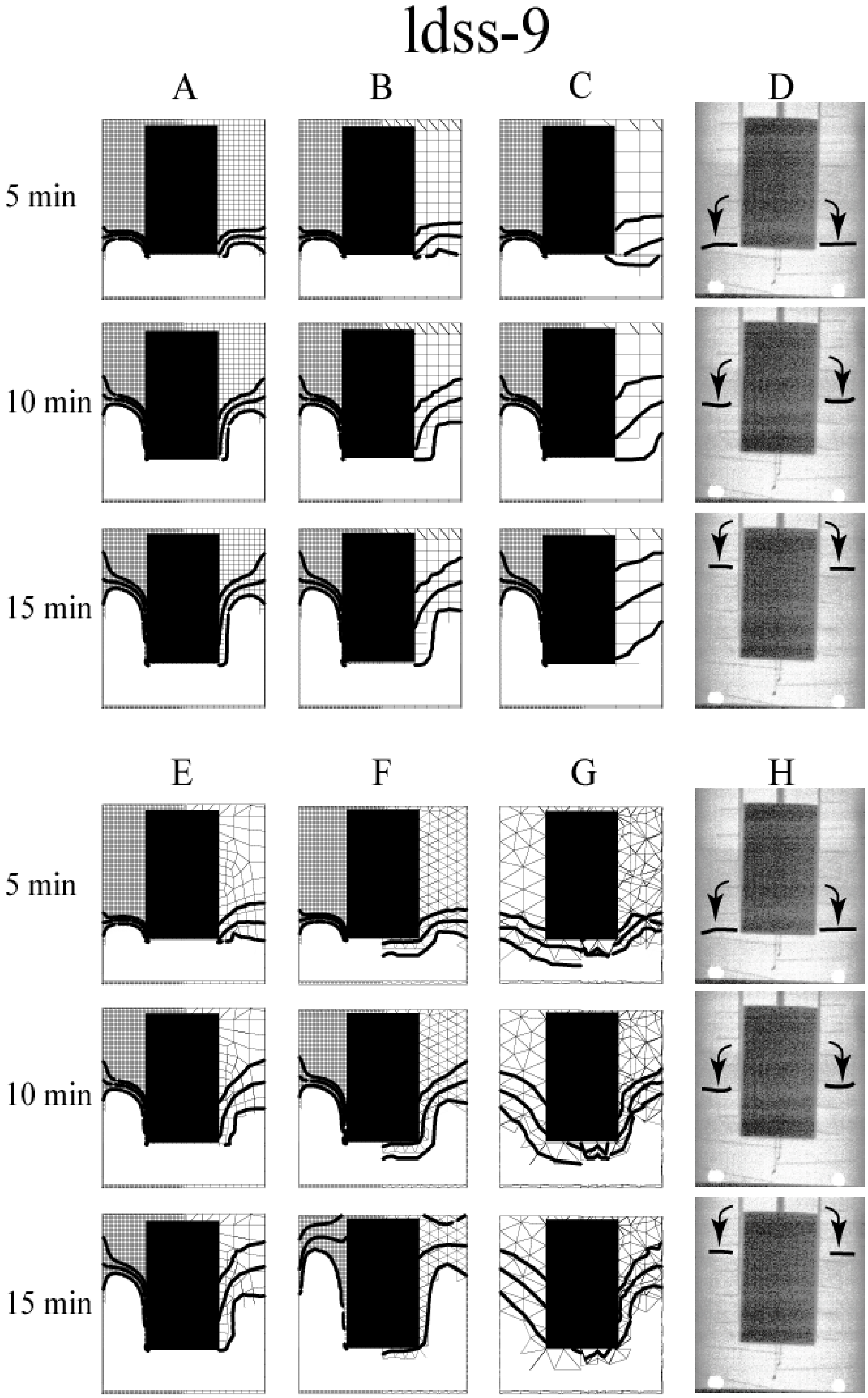

Fig. 9.16. Comparison between SPUF predictions using various mesh types and sizes as described in the footnote of Table 9.1and X-ray images for experiment ldss-9.

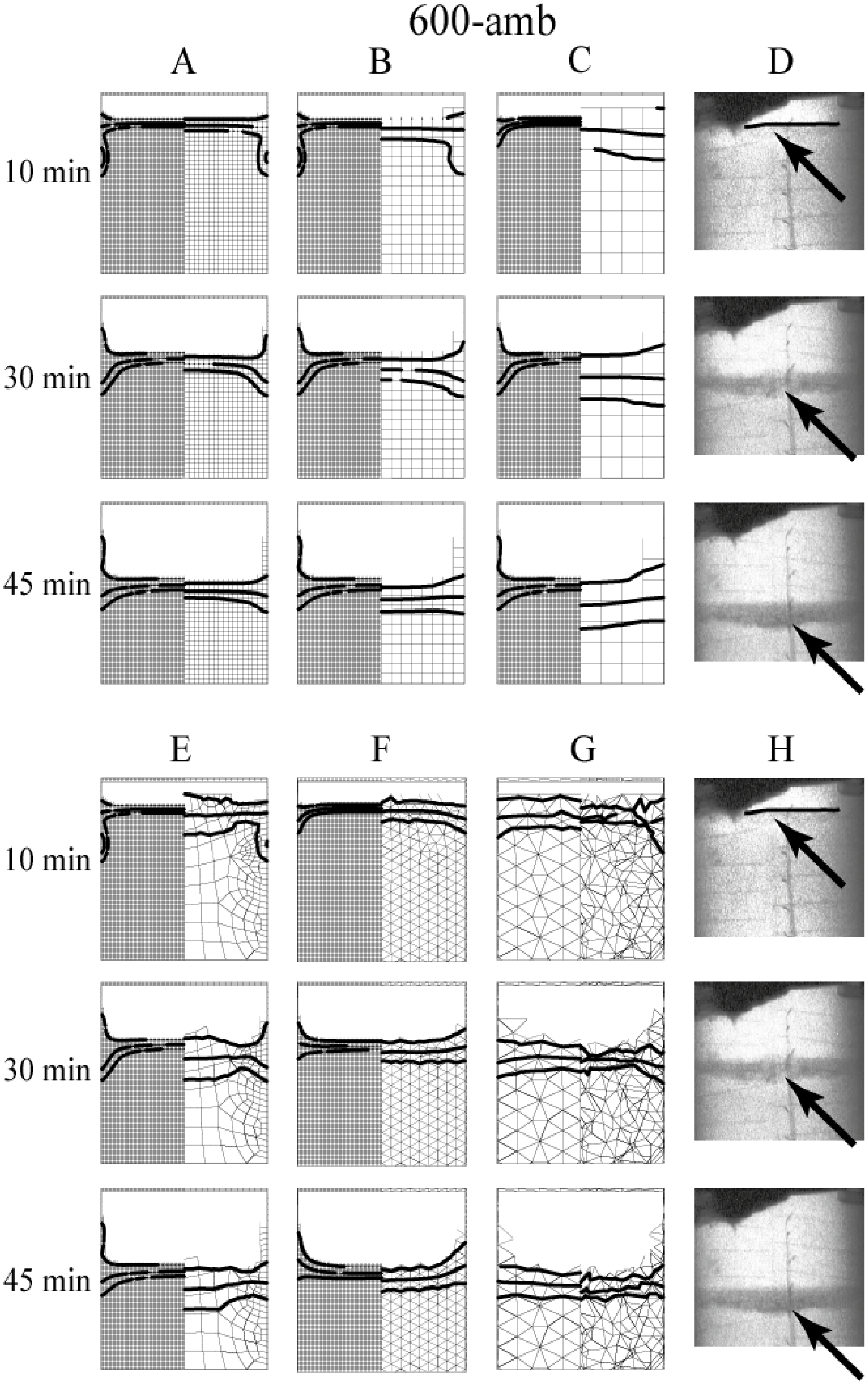

Fig. 9.17. Comparison between SPUF predictions using various mesh types and sizes as described in the footnote of Table 9.1and X-ray images for experiment 600-amb-p4.

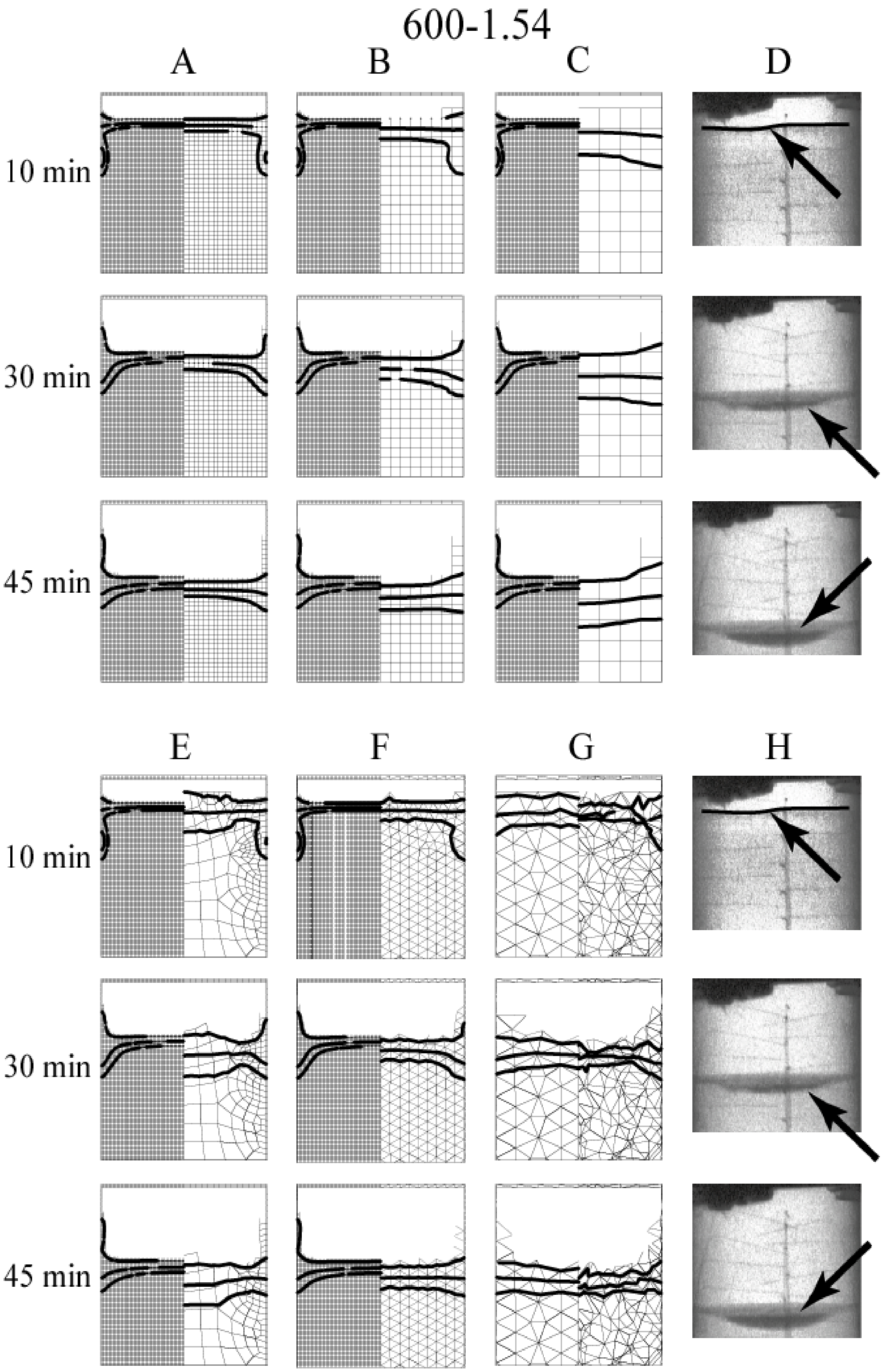

Fig. 9.18. Comparison between SPUF predictions using various mesh types and sizes as described in the footnote of Table 9.1and X-ray images for experiment 600-1.54-p2.

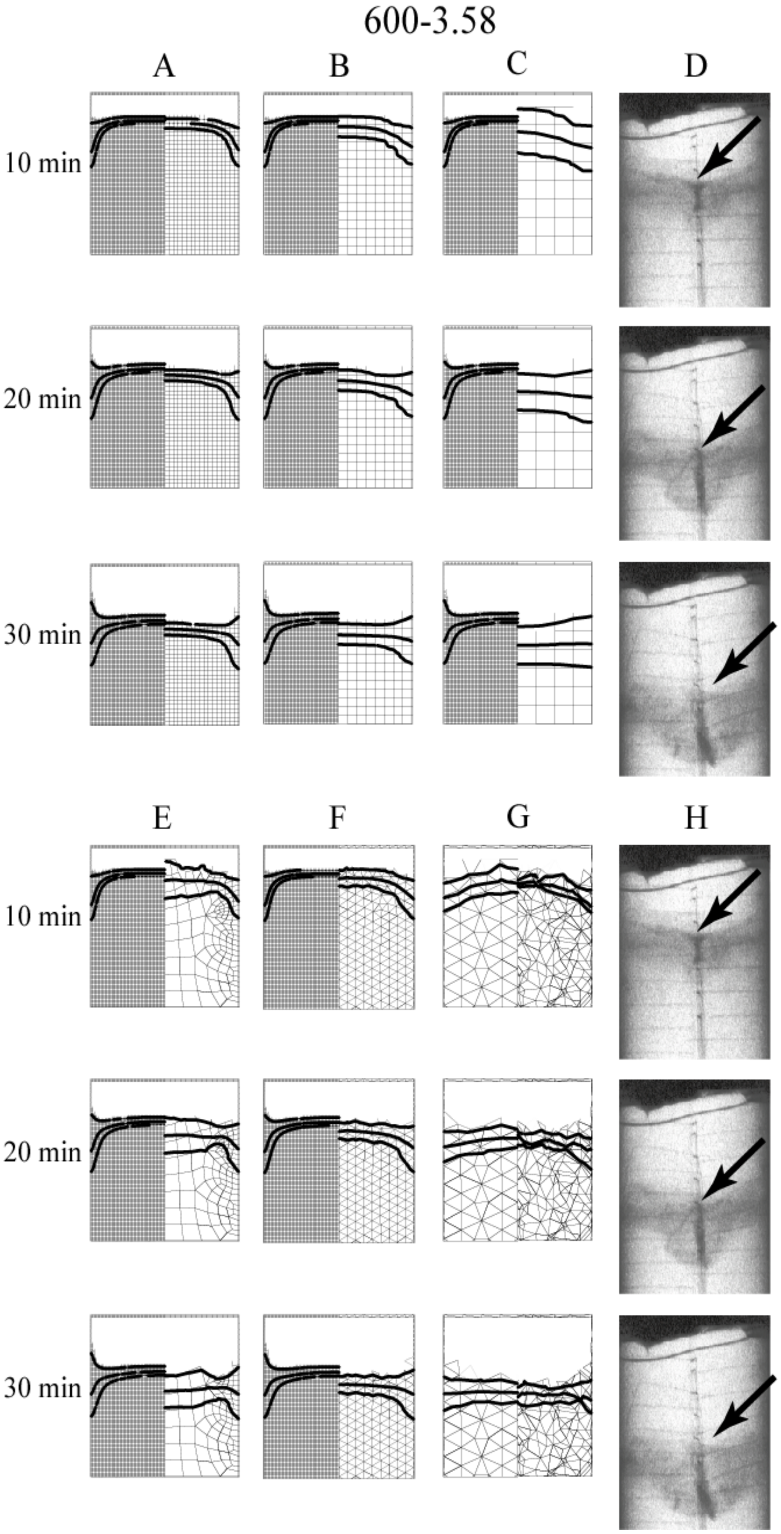

Fig. 9.19. Comparison between SPUF predictions using various mesh types and sizes as described in the footnote of Table 9.1and X-ray images for experiment 600-3.58-p3.

Table 9.2 gives the CPU times for all of the CPUF and SPUF simulations presented n Figures 9.1 through 9.19. The relative CPU time with respect to the 2D axisymmetric CPUF simulation run using 1-mm regular quadrilateral elements is also shown in Table 9.2. All of the 2D SPUF results (A through F) were run using COYOTE. The 3D SPUF results (G) were run with CALORE. The 2D SPUF run (C) using 1-cm regular quadrilateral elements (1-cm SPUF element size compared to 0.1-cm for the CPUF element size), resulted in a two orders of magnitude decrease in CPU time. Several other CPU studies were initiated to directly compare CPU requirements for COYOTE and CALORE. For identical 3D SPUF runs using identical HEX meshes, the overall CPU time for the CALORE simulation was about half of the CPUF time for an essentially identical simulation using COYOTE. The difference in CPU times was caused by differences in the radiation viewfactor calculations. The COYOTE simulation used an older version of the radiation viewfactor algorithm, which was slower than the newer radiation algorithm used by CALORE.

Table 9.2. CPU times for radiant heat simulations

	Plot	**A-G**	**A**	**B**	**C**	**D**	**E**	**F**	**G**
Figure	**Case**	**CPUF**	**SPUF.25**	**SPUF.5**	**SPUF1**	**SPUF-paved**	**SPUF-stri**	**SPUF-ltri**	**3D-CALORE**
10.1	**600-1**	14:22:00	2:40:00	0:23:03	0:04:16	1:05:00	1:23:00	0:10:49	42:19:18
10.2	**750-2**	7:59:00	3:43:00	0:32:10	0:10:37	1:22:00	2:09:00	0:18:12	34:47:02
10.3	**900-3**	10:30:50	5:34:26	0:51:47	0:09:01	1:28:25	2:56:17	0:23:28	25:15:41
10.4	**900-14**	14:08:00	5:28:00	0:54:30	0:08:40	1:29:00	2:17:00	0:20:05	22:42:22
10.5	**ld600-6**	5:44:22	0:56:54	0:18:38	0:03:28	0:35:38	0:33:40	0:07:23	19:30:33
10.6	**ld750-12**	9:08:00	2:03:00	0:39:32	0:07:28	0:51:17	1:04:00	0:14:34	16:57:50
10.7	**ld900-7**	1:18:27	1:58:36	0:28:35	0:06:23	0:53:34	1:05:59	0:13:30	9:02:24
10.8	**side-11**	6:20:45	1:02:14	0:16:56	0:05:44	0:42:33	0:44:55	0:12:11	36:51:34
10.9	**side-13**	8:29:00	3:52:00	0:40:22	0:06:56	1:23:00	1:58:00	0:15:40	40:02:11
10.10	**top-10**	9:16:00	1:23:00	0:07:18	0:05:55	0:10:48	0:51:54	0:04:10	52:02:12
10.11	**al-4**	21:59:56	2:50:18	0:33:05	0:10:49	1:03:54	1:24:24	0:19:11	134:45:42
10.12	**al-15**	16:02:00	2:50:00	0:31:30	0:09:39	0:59:13	1:28:00	0:23:02	124:25:58
10.13	**ss-1000-19**	13:26:00	2:42:00	0:28:36	0:03:23	0:24:01	1:01:00	0:16:48	29:47:08
10.14	**ss-5**	7:07:00	1:23:00	0:22:12	0:05:12	0:30:01	1:11:00	0:17:47	71:55:27
10.15	**ldss-9**	10:12:00	2:30:00	0:22:10	0:03:52	0:28:28	1:04:00	0:14:23	22:01:37
10.16	**ldal-8**	16:49:00	3:52:00	0:49:10	0:09:44	1:31:00	1:38:00	0:27:47	26:34:31
10.17	**600-AMB**	2:55:00	1:40:00	0:19:20	0:03:32	0:38:08	0:53:19	0:06:25	29:15:02
10.18	**600-1.54atm**	2:25:00	0:58:36	0:11:40	0:03:10	0:41:11	0:46:19	0:06:10	25:58:08
10.19	**600-3.58atm**	2:08:00	1:43:00	0:18:04	0:03:27	0:39:26	0:39:42	0:06:47	18:25:20
Ave. CPU (s)		34169	9316	1733	383	3210	4767	879	148295
Average (hh:mm:ss)		9:29:29	2:35:16	0:28:53	0:06:23	0:53:30	1:19:27	0:14:39	41:11:35
Relative CPU%		100	27.3	5.1	1.1	9.4	14.0	2.6	434.0

CPU savings can also be obtained by using “zombie elements” to improve computational performance. A “zombie element” is an element that should be removed from the computational domain since the “death criterion” has been satisfied, but is not removed until additional criteria, are met. The additional criteria are referred to as “zombie criteria”. In the current report, time step is used as the “zombie criteria” in addition to the solid fraction based “death criteria”. To use zombie elements, not only does the solid fraction death criteria need to be satisfied as discussed in Section 6, but “element death” is only allowed to occur at user specified increments of the time step.

Figure 9.20.A shows the effect of using the time-step “zombie criterion” for the 3D CALORE calculation for run TOP-10 shown previously in Fig. 9.19.G. The benefit of using a time-step “zombie criterion” is that the “zombie criterion” adapts with the auto-time-step feature in COYOTE and CALORE. The CPU-savings is significant as shown in Fig. 9.20.B. The saving is caused by not updating the viewfactors at every time step and allowing more elements to die between viewfactor calculations. Figure 9.20.C shows that the CPU cost of radiation drops and becomes comparable to the CPU cost of solving the chemistry equations. The required CPU drops dramatically as the “zombie criterion” is increased from a value of 10 to a value of 600, with little loss of accuracy as shown in Fig. 9.20.A. The uncertainty in the front location is on the order of 1-cm, which is the nominal size of the elements used in the 3D calculation.

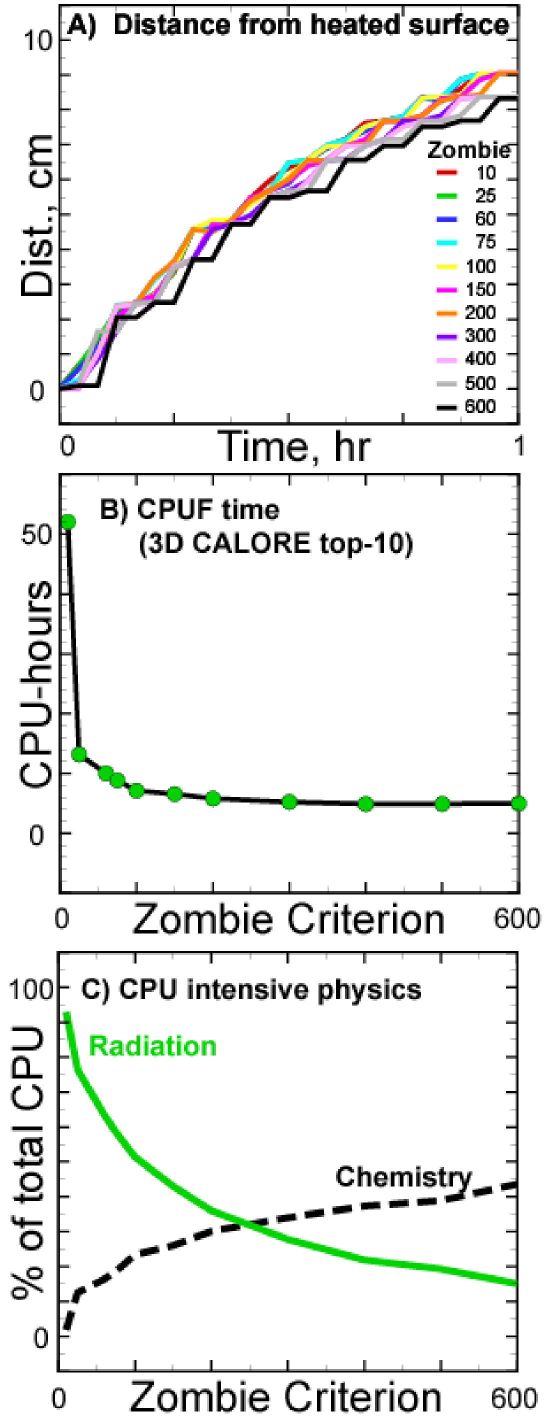

Fig 9.20. Front distance and CPU requirements for SPUF simulation calculated using 3D 1-cm^3 TET elements (see Fig. 9.10.G). A) Centerline distance from heated surface for various time-step “zombie criterion,” B) CPU-time as function of the zombie criterion, and C) percent of overall CPU attributed to radiation viewfactor calculations and chemistry calculations.

10 Summary and Conclusions

A simple mass loss model has been used with element death to simulate the response of unconfined, rigid, closed-cell, polyurethane foam. Elements are removed when the solid fraction within elements drop below a specified criterion. This criterion, known as the “death criterion”, was specified in the SPUF model based on experimental data. A second criterion, referred to as the “zombie criterion,” was used to obtain significant computational savings by limiting the update of the viewfactor calculation. Various one-dimensional simulations using element death were performed to determine the steady-state decomposition front velocity for a strand of foam insulated on three sides with one side exposed to a far-field radiation boundary condition. The steady-state front velocity was found to be highly dependent on the size of the element used in the simulations. By reducing the size of the element to 100-μm, a grid independent velocity was determined. Large-scale simulations are impractical using such small elements. A subgrid model for the SPUF foam response model was developed to correct the solution so that practical element sizes can be used for large-scale calculations to give the grid-independent solution. The methodology for bias correction was shown to be valid for a variety of element types such as 2D-QUAD elements, 2D-TRI elements, 3D-HEX elements and 3D-TRI elements.

The SPUF activation energies were assumed to be normally distributed and were obtained from various small-scale experiments. Thermophysical parameters for the SPUF model included density, temperature, thermal conductivity, specific heat, reaction enthalpy, and surface emissivity. The chemistry parameters included the two frequency factors commonly referred to as the pre-exponential factors, the two activation energies, and the two standard deviation of the activation energy used to distribute each of the reaction rates. The thermal conductivity and specific heat were linear functions of temperature between 23ºC and 250ºC. For temperatures greater than 250ºC, thermal conductivity and specific heat were linearly extrapolated. Thermal conductivity and specific heat were measured for three densities of foam – 0.078-g/cm^3, 0.15-g/cm^3, and 0.352-g/cm^3

Mass loss predictions were compared to mass loss measurements made in low pressure unconfined TGA experiments with the sample temperature ramped at 5ºC/m, 20ºC/m, and 50ºC/m. All of the ramped TGA mass loss data were within the 95% prediction limit of the SPUF model determined using mean value analysis. All of the chemistry parameters were shown to contribute to the uncertainty in the mass loss predictions with the initial reaction being more important at low temperatures and the final reaction being more important at higher temperatures. Similar comparisons were made with isothermal experiments where small samples were ramped from ambient temperatures to 250ºC, 270ºC, and 300ºC and held for 50 hours, 20 hours, and 20 hours, respectively. Reasonable solutions were obtained for all of the isothermal experiments.

As the final test of the SPUF response model, 19 radiant heat experiments were simulated. To test the discretization bias correction model using a variety of element types, each of the 19 radiant heat experiments were simulated using seven different meshes – 1) a 0.25 regular QUAD mesh, 2) a 0.5-cm regular QUAD mesh, 3) a 1.0-cm regular QUAD mesh, 4) a paved QUAD mesh, 5) a small tri-mesh, 6) a large tri-mesh, and 7) a 1.0-cm TET mesh. The first 6 mesh types were run assuming the geometry was 2D axisymetric. The last mesh type was run using a full 3D mesh. The radiant heat simulations were compared to CPUF predictions as well as to X-ray images of the experiment at selected time intervals.

The 19 radiant heat experiments included the effects of 1) the bottom plate temperature for high-density RPU foams, 2) the bottom plate temperature for low-density RPU foams, 3) the orientation of the heated plate in relationship to the gravity vector, 4) the influence of the embedded components in high-density foam, 5) the influence of the embedded components in low-density foam, 6) and the level of backpressure as well as the degree of confinement of the decomposition gases. The temperature boundary conditions for the heated plate and confinement walls were presented. The measured heat flux near the heated plate was also presented.

The radiant heat experiments were recorded using an X-ray camera with shots taken for most of the experiments every 30 seconds (for experiment ss-1000-19, the X-ray pictures were taken every 18 seconds). For the 19 radiant heat experiments, selected X-rays were compared to SPUF predictions. The X-ray images show density variations that correspond to the presence or absence of foam within the enclosure. In the X-ray images, the decomposition front appeared darker than the surrounding foam or enclosure. Calculated solid fraction contours were overlaid onto the predicted temperature plots and compared to the X-rays. Agreement between most of the SPUF predictions are within expected uncertainty due to model parameters and boundary conditions except for the semi-confined radiant heat experiments performed at elevated temperatures.

The front velocities for the partially confined radiant heat experiments at relatively low pressures, 600-amb-p4 and 600-1.54-p2, decreased slightly in comparison to the ambient pressure unconfined experiment 600-1. However, at 0.36-MPa backpressure, the decomposition front velocity for experiment 600-3.58-p3 was shown to increase, rather than decrease. The enhanced decomposition at 0.36-MPa may be due to liquefaction resulting in disappearance of the foam structure and increased heat transfer. Liquefaction of the RPU foam was also observed in the X-ray movies for all of the semi-confined decomposition experiments, even at low pressures.

Higher boundary temperatures (higher fluxes) resulted in faster decomposition fronts and narrow reaction zones for the unconfined radiant heat experiments. Orientation did not seem to have a large effect on the unconfined experiments. Flow effects were observed when the foam was partially confined. The high thermal capacitance components had little effect on the propagation of the decomposition fronts. However, the low thermal capacitance components caused the foam near the surface of the component to preheat significantly and caused the decomposition front to move rapidly around the component. Lower density foam resulted in faster decomposition front velocities due to less material available for decomposition.

In summary, various experiments were modeled using a simple foam decomposition mechanism to predict mass loss using two reaction steps. The dynamic radiation enclosure was simulated by removing elements from the computational domain after meeting an element death criterion based on the foam chemistry (calculated solid fraction within the finite elements). Uncertainty was propagated into some of the numerical simulation to show the relative importance of model parameters. Model results were compared to TGA weight-loss measurements and X-ray images of the various large-scale experiments. Although the shape of the front was difficult to determine near the wall in the X-rays and the location of the front was difficult to see in the low-density experiments, the calculated and measured locations of the decomposition fronts for the unconfined experiments were well within 1-cm of each other and in some cases the fronts coincided.

References

1. Gartling, D. K., Hogan, R. E., and Glass, M. W., “COYOTE – A Finite Element Computer Program for Nonlinear Heat Conduction Problems,” Sandia National Laboratories Report SAND94-1173 (theory) and SAND94-1179 (user’s manual), Albuquerque, NM (1998).

2. Bova, S.W., Glass, M.W., Dowding, K.J., Lober, R.R., Cochran, R.J., “Calore, A Computational Heat Transfer Program: Volume I Theory Manual,” Sandia National Laboratories Report SANDTBD (In Review).

3. Hobbs, M. L., Erickson, K. L., and Chu, T. Y., “Modeling Decomposition of Unconfined Rigid Polyurethane Foam,” Sandia National Laboratories report SAND99-2758, Albuquerque, NM (1999).

4. Hobbs, M. L., Erickson, K. L., and Chu, T. Y., “Modeling Decomposition of Unconfined Rigid Polyurethane Foam,” *Polymer Degradation and Stability*, **69**(1), 47 (2000).

5. Hobbs, M.L., Erickson, K.L., Chu, T.Y., Borek, T.T., Thompson, K.R., Dowding, K.J., Clayton, D., and Fletcher, T. H., “CPUF – A Chemical-Structure-Based Polyurethane Foam Decomposition and Foam Response Model,” Sandia National Laboratories Report SAND2003-2282 (2003).

6. Jackson, L.P., Erickson, K.L., Castaneda, J.N., Borek, T.T., “Thermal Decomposition of Aged Rigid Polyurethane (RPU) Foam from the MC3276,” Sandia National Laboratories Report SAND2002-1132 (2002).

7. Erickson, K.L., Castaneda, J.N., Ulibarri, T.A., Derzon, D.K., Renlund, A.M., “Thermal Decomposition Chemistry of Rigid Polyurethane (RPU) Foams,” Sandia National Laboratories Report, Albuquerque, NM (In Preparation).

8. Erickson, K. L., Borek, T. T., Renlund, A. M., Ulibarri, T. A., Clayton, D., and Fletcher, T. H., “Thermal Decomposition Chemistry of a Rigid Polyurethane Foam,” in Proc. of the 222nd National Meeting and Exposition of the American Chemical Society (2001).

9. Clayton, D., J. “Modeling Flow Effects During Polymer Decomposition using Percolation Lattice Statistics,” Dissertation, Brigham Young University, Provo, UT (2002).

10. Hobbs, M.L. and Romero, V. J., “Uncertainty analysis of decomposing polyurethane foam,” *Thermochimica Acta*, **384**, 393 (2002).

11. Robinson, D. G., “A Survey of Probabilistic Methods Used in Reliability, Risk and Uncertainty Analysis: Analytical Techniques,” Sandia National Laboratories Report SAND98-1189, Albuquerque, NM (1998).

12. Taylor, R. E., Groot, H., and Ferrier, J., “Thermophysical Properties of a Foam and Pyromark Paint,” Thermophysical Properties Research Laboratory Report TPRL 1833, Purdue University Research Park, West Lafayette, IN (1997).

13. Taylor, R. E., Groot, H., and Ferrier, J., “Thermophysical Properties of Two Foams A Report to Sandia national Laboratories,” Thermophysical Properties Research Laboratory Report TPRL 1964, Purdue University Research Park, West Lafayette, IN (1998).

14. Chu, T. Y., Hobbs, M. L., Erickson, K. L., Ulibarri, T. A., Renlund, A. M., Gill, W., Humphries, L. L., and Borek, T. T., “Fire-Induced Response in Foam Encapsulants,” in Proceedings SAMPE 1999-44th International SAMPE Symposium & Exhibition (1999).

15. Eldred, M. S., “Optimization Strategies for Complex Engineering Applications,” Sandia National Laboratories report SAND98-0340. Albuquerque, NM (1998).

Appendix

This appendix contains some of the FORTRAN code used to solve the ODE describing the SPUF model:

```
      program spuf
C23456789x123456789x123456789x123456789x123456789x123456789x123456789x12
C----------------------------------------------------------------------C
C  The is the Simple PolyUrethane Foam (SPUF) decomposition model
C  FOAM --> 0.7 G1 + 0.3 S1
C  S1   -->     G2
C----------------------------------------------------------------------C
C. . .VARIABLE DECLARATIONS. . . . . . . . . . . . . . . . . . . . . . .
      implicit none
      integer maxt, neq, lrw, liw, nmer, ntmax, iprint, ntim, ieee
      integer iii, idid, ipar, ieee_handler
      parameter (maxt=7000)
      parameter (neq = 4,lrw = 250+neq*(10+neq), liw = 56+neq)
      integer info(15), iwork(liw)
      double precision dt,dt0,dtmax,timax,zero,one,half,small,x,fx
      double precision y(neq), rwork(lrw), tim(maxt),tem(maxt), rpar(2)
      double precision atol,rtol,time,tout,tp,foam,g1,g2,s1,sf
      double precision tfun, jac
      logical louta,loutf,screen
      external func, sample_handler
C. . .COMMON BLOCK AREA. . . . . . . . . . . . . . . . . . . . . . . . .
      common /cdbl1/ dt,dt0,dtmax
      common /cint1/ iprint, ntmax, nmer
      common /clog1/ louta,loutf,screen
      common /ctime/ tim,tem,timax,ntim
C. . .DATA STATEMENTS. . . . . . . . . . . . . . . . . . . . . . . . . .
      data zero,one/0.D0,1.D0/
      data half,small/0.5D0,1.D-20/
C----------------------------------------------------------------------C
C Error trapping for SUN IV  . . . . . . . . . . . . . . . . . . . . .
C----------------------------------------------------------------------C
      ieee = ieee_handler('set','common',sample_handler)
      if (ieee.ne.0) print *, 'ieee_handler cannot set common '
C----------------------------------------------------------------------C
C Call init to initialize parameters and read input files
C Call echo to write parameters to output file
C----------------------------------------------------------------------C
      call init
      call echo
c   Initialize solver variables
      call sinit (info,atol,rtol)
C----------------------------------------------------------------------C
C Set initial    y(1)  = foam
C condition:     y(2)  = g1
C                y(3)  = g2
C                y(4)  = s1
C----------------------------------------------------------------------C
      y(1) = 1.0
      y(2) = 0.0
      y(3) = 0.0
      y(4) = 0.0
C----------------------------------------------------------------------C
```

```
C Begin solvers Do loop
C----------------------------------------------------------------------C
      time = zero
      do 100 iii=1,ntmax
C----------------------------------------------------------------------C
C CALL DEBDF     y(1)  = foam
C to calculate:  y(2)  = g1
C                y(3)  = g2
C                y(4)  = s1
C----------------------------------------------------------------------C
         tout = time+dt
         call ddebdf (func,neq,time,y,tout,info,rtol,atol,idid,
     &                rwork,lrw,iwork,liw,rpar,ipar,jac)
         tp = tfun(time,ntim,tim,tem)
         if (idid.lt.0) call error (idid,'cpuf.f',1,rwork,info)
C----------------------------------------------------------------------C
C Unravel solution vector
C----------------------------------------------------------------------C
      foam  = y(1)
      g1    = y(2)
      g2    = y(3)
      s1    = y(4)
C----------------------------------------------------------------------C
C Calculate solid fraction, sf
C----------------------------------------------------------------------C
cmlh      sf =  1.-g1-g2
          sf =  foam+s1
          fx = 1.-foam
          call inverf(fx,x)
          rpar(1) = x
c         fx = s1/0.3
          fx = 1.-sf
          call inverf(fx,x)
          rpar(2) = x
          if (mod(iii-1,iprint).eq.0) then
C----------------------------------------------------------------------C

             if (loutf) write(26,4000) time/60.,sf
             if (loutf) write(29,4001) tp-273.15,sf
c            if (screen)write(6,6000) time/60.,sf,idid,rwork(11)
             if (louta) write(21,1000) tp-273.15,foam, g1, g2, s1
          endif
100   continue
      stop
1000  format(' ',g10.4,15(1x,f7.5))
4000  format(' ',g10.4,2(1x,f8.5))
4001  format(' ',g10.4,2(1x,f8.5))
6000  format(' ',g10.4,1x,f8.5,1x,i2,1x,g10.4)
end
```

```
      subroutine func (time,y,ydot,rpar,ipar)
C-----------------------------------------------------------------------C
C This subroutine calculates time derivatives
C-----------------------------------------------------------------------C
c  ydot(i) = derivative of y(i) in time
C-----------------------------------------------------------------------C
C  y(1) = foam           foam ---> 0.7 G1 + 0.3 S1
C  y(2) = g1             S1   --->     G2
C  y(3) = g2
C  y(4) = s1
C-----------------------------------------------------------------------C
C. . .VARIABLE DECLARATIONS. . . . . . . . . . . . . . . . . . . . . . .
C     implicit double precision (a-h,o-z)
      implicit none
      integer ipar,neq, nrxn, maxt,ntim,i
      parameter (neq = 4, nrxn = 2, maxt = 7000)
      double precision k(nrxn),a(nrxn),e(nrxn),esig(nrxn)
      double precision time,tim(maxt),tem(maxt),timax
      double precision y(neq),ydot(neq),rpar(3),zero,rg,foam,g1,g2,s1
      double precision t, rt, tfun, r1, r2
C. . .COMMON BLOCK AREA. . . . . . . . . . . . . . . . . . . . . . . . .
      common /ctime/ tim,tem,timax,ntim
      common /cdbl4/ a,e,esig
C. . .DATA STATEMENTS. . . . . . . . . . . . . . . . . . . . . . . . . .
      data zero,rg/0.0D0,1.987D0/
      save
C Unravel variables used in rate expressions
      foam  = dmax1(y(1),zero)
      g1    = dmax1(y(2),zero)
      g2    = dmax1(y(3),zero)
      s1    = dmax1(y(4),zero)
C  calculate particle temperature
      t = tfun(time,ntim,tim,tem)
C  calculate rate constants
      rt = rg*t
      do 100 i = 1,nrxn
         k(i) = a(i)*dexp(-(e(i)+rpar(i)*esig(i))/rt)
100   continue
C-----------------------------------------------------------------------C
C  y(1) = foam ;  y(2) = g1 ;  y(3) = g2 ;  y(4) = s1 ;  y(5) = s2
C-----------------------------------------------------------------------C
C  set up rate equations
      r1 = k(1)*foam
      r2 = k(2)*s1
      ydot(1) = -r1
      ydot(2) = +0.7*r1
      ydot(3) = +r2
      ydot(4) = +0.3*r1-r2
      return
C***********************************************************************
C-----------------------------------------------------------------------
C- - - - - - - - - -  Variable Index (for func.f) - - - - - - - - - - -
C-----------------------------------------------------------------------
C. . . . . . . . . . . . . . . . . . . . . . . . . . . . . . . . . . . .
C Variables                      Description and Units
C ---------   ----------------------------------------------------------
C a           frequency factor, 1/s
```

```
C y           solution vector for init. value problem: y(1,2,3) = l,d,c
C ydot        time derivative y, dydt
C zero        double precision 0.0
      end
```

Distribution

Brigham Young University (1)
Department of Chemical Engineering
Attn: Dr. Thomas H. Fletcher
350 K Clyde Building
Provo, Utah 84602-4100

Easterling Statistical Consulting (1)
51 Avenida del Sol
Cedar Crest, NM 87008

Federal Aviation Administration (1)
Attn: Richard E. Lyon
Fire Safety Section, AAR-422
William J. Hughes Technical Center
Atlantic City International Airport, NJ 08405

Gordon H. Lemmon (1)
4234 Nonaville Rd.
Mt. Juliet, TN 37122

New Mexico State University (1)
Department of Mechanical Engineering
Attn: Richard G. Hills
Las Cruces, New Mexico 88003

Pratt & Whitney (1)
Attn: Dan Clayton
M/S 163-03
400 Main Street
East Hartford, CT 06108

Shawna Liff (1)
2010 Clark Rd.
East Montpelier, VT 05651

United States Department of Commerce (1)
Attn: Kathryn M. Butler
Building and Fire Research Laboratory
National Institute of Standards and Technology
Gaithersburg, MD 20899

University of California, Berkeley (1)
Attn: Carlos Fernandez-Pello
Mechanical Engineering Department
6105a Etcheverry Hall
University of California
Berkeley, CA 94720

University of Utah (1)
Attn: Ronald Pugmire
Associate Vice President for Research
Professor of Chemical & Fuels Engineering
210 Park Building
Salt Lake City, UT 84112

University of Utah (1)
Attn: David M. Grant
Distinguished Professor of Chemistry
Henry Eyring Bldg
315 S 1400 East Rm 2020
Salt Lake City, UT 84112

University of Washington (1)
Dept of Mechanical Engineering
Attn: Ashley Emery
Box 352600
Seattle, WA 98195-2600

Sandia

1	MS0888	1811	R. L. Clough
1	MS0888	1811	E. M. Russick
1	MS0886	1822	R. P. Goehner
1	MS0886	1822	T. T. Borek
1	MS0481	2132	R. J. Harrison
1	MS0481	2132	D. R. Helmich
1	MS0481	2132	T. F. Hendrickson
1	MS0427	2134	R. A. Paulsen, Jr.
1	MS1452	2552	L. G. Minier
1	MS1454	2554	A. M. Renlund
1	MS0311	2616	M. J. Craig
1	MS1202	5932	T. A. Ulibarri
1	MS0748	6413	D. G. Robinson
1	MS9051	8351	A. R. Kerstein
1	MS9052	8361	R. Behrens, Jr.
1	MS9052	8361	S. B. Margolis
1	MS0841	9100	T. C. Bickel
1	MS0836	9100	M. R. Baer
1	MS1393	9100	T. Y. Chu (in Washington DC, Forrestal Building)
1	MS0826	9100	D. K. Gartling
1	MS0834	9112	M. R. Prairie
1	MS0834	9112	K. L. Erickson
1	MS0834	9112	S. M. Trujillo
1	MS0826	9113	S. N. Kempka
1	MS0834	9114	J. E. Johannes
1	MS0834	9114	T. A. Baer
1	MS0834	9114	P. L. Hopkins
1	MS0834	9114	A. M. Kraynik
1	MS0834	9114	P. R. Schunk
1	MS0834	9114	A. C. Sun
1	MS0836	9116	E. S. Hertel
1	MS0836	9116	B. L. Bainbridge
1	MS0836	9116	B. D. Boughton
1	MS0836	9116	J. F. Dempsey

1	MS0836	9116	D. D. Dobranich
1	MS0836	9116	R. C. Dykhuizen
1	MS0836	9116	N. D. Francis, Jr.
10	MS0836	9116	M. L. Hobbs
1	MS0836	9116	R. E. Hogan
1	MS0836	9116	C. Romero
1	MS0836	9116	R. G. Schmidt
1	MS0836	9117	R. O. Griffith
1	MS0836	9117	M. E. Larsen
1	MS0555	9122	M. S. Garrett
1	MS0555	9122	K. R. Thompson
1	MS0893	9123	M. K. Neilsen
1	MS0824	9130	J. L. Moya
1	MS0821	9132	L. A. Gritzo
1	MS0836	9132	W. Gill
1	MS1135	9132	J. T. Nakos
1	MS1135	9132	V. F. Nicolette
1	MS1135	9132	S. R. Tieszen
1	MS0828	9133	M. Pilch
1	MS0828	9133	B. F. Blackwell
1	MS0828	9133	K. J. Dowding
1	MS0828	9133	V. J. Romero
1	MS0828	9133	W.L. Oberkampf
1	MS0835	9140	J. M. McGlaun
1	MS0835	9141	E. A. Boucheron
1	MS0835	9141	S. W. Bova
1	MS0835	9141	M. W. Glass
1	MS0835	9141	R. R. Lober
1	MS0847	9211	M. S. Eldred
1	MS0819	9211	R. G. Trucano
1	MS0847	9226	T. D. Blacker
1	MS0847	9226	R. A. Kerr
1	MS0423	9732	J. A. Fernandez
1	MS0151	9750	A. C. Ratzel
1	MS0421	9800	W. Hermina
1	MS0139	9900	M. O. Vahle
1	MS0139	9905	S. E. Lott
1	MS0829	12323	B. M. Rutherford
1	MS0405	12333	T. R. Jones
1	MS0405	12333	L. A. Schoof
1	MS0405	12333	S. E. Camp
1	MS9018	8945-1	Central Technical Files
2	MS0899	9619	Technical Library